

Spring 2007

Fabrication and Compressive Behavior of Corrugated Aramid-Epoxy Cellular Solids

Jeffrey Arthur Schneider
Embry-Riddle Aeronautical University - Daytona Beach

Follow this and additional works at: <https://commons.erau.edu/db-theses>



Part of the [Aerospace Engineering Commons](#)

Scholarly Commons Citation

Schneider, Jeffrey Arthur, "Fabrication and Compressive Behavior of Corrugated Aramid-Epoxy Cellular Solids" (2007). *Theses - Daytona Beach*. 228.
<https://commons.erau.edu/db-theses/228>

This thesis is brought to you for free and open access by Embry-Riddle Aeronautical University – Daytona Beach at ERAU Scholarly Commons. It has been accepted for inclusion in the Theses - Daytona Beach collection by an authorized administrator of ERAU Scholarly Commons. For more information, please contact commons@erau.edu.

FABRICATION AND COMPRESSIVE BEHAVIOR
OF CORRUGATED ARAMID-EPOXY CELLULAR SOLIDS

by

Jeffrey Arthur Schneider

A Thesis Submitted to the
Graduate Studies Office
in Partial Fulfillment of the Requirements for the Degree of
Master of Science in Aerospace Engineering

Embry-Riddle Aeronautical University
Daytona Beach, Florida
Spring 2007

UMI Number: EP32007

INFORMATION TO USERS

The quality of this reproduction is dependent upon the quality of the copy submitted. Broken or indistinct print, colored or poor quality illustrations and photographs, print bleed-through, substandard margins, and improper alignment can adversely affect reproduction.

In the unlikely event that the author did not send a complete manuscript and there are missing pages, these will be noted. Also, if unauthorized copyright material had to be removed, a note will indicate the deletion.

UMI[®]

UMI Microform EP32007
Copyright 2011 by ProQuest LLC
All rights reserved. This microform edition is protected against
unauthorized copying under Title 17, United States Code.

ProQuest LLC
789 East Eisenhower Parkway
P.O. Box 1346
Ann Arbor, MI 48106-1346

FABRICATION AND COMPRESSIVE BEHAVIOR
OF CORRUGATED ARAMID-EPOXY CELLULAR SOLIDS

by

Jeffrey Arthur Schneider

This thesis was prepared under the direction of the candidate's thesis committee chairman, Dr. David J. Sypeck, Department of Aerospace Engineering, and has been approved by the members of his thesis committee. It was submitted to the Office of Graduate Programs and was accepted in partial fulfillment of the requirements for the degree of Master of Science in Aerospace Engineering.

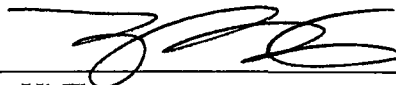
THESIS COMMITTEE:



Dr. David J. Sypeck,
Chairman



Dr. Frank Radosta
Member



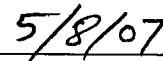
Dr. Yi Zhao
Member



MSAE Graduate Program Coordinator



Department Chairman, Aerospace Engineering



Date

ACKNOWLEDGEMENTS

I would like to extend my gratitude to the Thesis Chairman, Dr. Sypeck. His optimism, patience, encouragement, helpful suggestions, and most importantly, patience, were crucial in the research and writing in support of this thesis. Without his help, this work would have never been completed. Appreciation is also in order for Drs. Radosta and Zhao for their support, both as committee members and as professors.

Thanks is also due for the entire Eagle Works department, including Professor Pierpont, Dr. Steve Roth, and Dr. Tim Wilson for their unequivocal willingness to share knowledge, offer encouragement, and provide suggestions in the development of this work.

ABSTRACT

Author: Jeffrey Arthur Schneider
Title: Fabrication and Compressive Behavior of Corrugated
Aramid-Epoxy Cellular Solids
Institution: Embry-Riddle Aeronautical University
Degree: Master of Science in Aerospace Engineering
Year: 2007

Cellular solids are materials whose base material does not always occupy the entire solid fraction available. A number of cellular solids can provide blast protection and absorb impact energy, but few perform well resisting blunt object (ballistic) penetration. In this thesis, a method is proposed for fabricating cellular solids from aramid-epoxy composites that can absorb impact energy and resist blunt object penetration. The aramid-epoxy samples were fabricated using wet-layup techniques, with two different styles of Kevlar 49 woven fabric in a variety of orientations. Test sample density ranged from 0.08 – 0.23 g/cm³. Different lamination orientations, assembly techniques, and bonding adhesives were investigated and assessed for their effect on quasi-static and dynamic crushing. A maximum plateau stress of 1.5 MPa was recorded with corresponding energy absorption of 4.2 J/g; values comparable to commercially produced metal foams. Methods for prediction of mechanical properties are presented/assessed along with suggestions for further improvements.

TABLE OF CONTENTS

ACKNOWLEDGEMENTS.....	iii
ABSTRACT.....	iv
LIST OF TABLES.....	vii
LIST OF FIGURES.....	viii
1. INTRODUCTION.....	1
1.1. Cellular Materials.....	2
1.1.1. Natural Cellular Materials.....	5
1.1.2. Synthetic Cellular Materials.....	9
1.1.3. Performance of Cellular Materials.....	17
1.2. Fibrous Composites and Applications.....	19
1.3. Fibers.....	20
1.3.1. Glass Fibers.....	21
1.3.2. Carbon Fibers.....	22
1.3.3. Aramid Fibers.....	25
1.3.4. Fiber Comparison.....	29
1.4. Matrices.....	31
1.4.1. Polyester Resin Matrix.....	31
1.4.2. Epoxy Resin Matrix.....	33
1.4.3. Vinyl Ester Resin Matrix.....	34
1.4.4. Matrix Comparison.....	34
1.5. Fibrous Composites and Theory.....	35
1.6. Energy Absorption.....	39
1.7. Penetration and Ballistic Impact Tolerance.....	45
2. CORRUGATED KEVLAR STRUCTURE.....	47
3. MECHANICAL BEHAVIOR PREDICTION.....	49
3.1. Composites.....	49
3.1.1. Laminated Plate Theory.....	49
3.1.2. Woven Fiber Theory.....	56
3.2. Plate Loading.....	60
3.3. Plate Geometry.....	62
3.4. Plate Instability.....	63
3.5. Triangular Corrugation.....	65
3.5.1. Geometry.....	65

3.5.2.	Properties	66
4.	SAMPLE DESIGN AND FABRICATION.....	70
4.1.	Sample Construction.....	70
4.1.1.	Mold Fabrication.....	71
4.1.2.	Ply Lay-Up.....	73
4.1.3.	Layer Assembly	77
5.	SAMPLE DETAILS AND TEST RESULTS.....	79
5.1.	Sample Overview.....	79
5.2.	Testing Setup	81
5.2.1.	Quasi-static Testing Apparatus.....	81
5.2.2.	Dynamic Testing Apparatus	82
5.3.	Experimental Results	84
5.4.	Sample 1.....	85
5.5.	Sample 2.....	87
5.6.	Sample 3.....	89
5.7.	Sample 4.....	91
5.8.	Sample 5.....	94
5.9.	Sample 6.....	97
5.10.	Sample 7.....	100
5.11.	Sample 8.....	102
5.12.	Sample 9.....	104
5.13.	Comparison of Results.....	105
6.	RESULTS AND ANALYSIS.....	107
6.1.	Validation of Predicted Results	107
6.2.	Comparison to Other Materials.....	110
6.3.	Further Research	118
6.4.	Conclusions.....	119
7.	REFERENCES	120
8.	Appendix A – Material Details	125
9.	Appendix B – Plate Stiffness Calculator	127

LIST OF TABLES

Table 1.1. Fiber properties.	29
Table 1.2. Specific fiber strength and modulus.	30
Table 1.3. Mechanical properties of some thermoset matrices [37, 46].	35
Table 1.4. Fiber and matrix property definitions.	37
Table 1.5. Elastic constants of unidirectional composites	38
Table 1.6. Maximum allowable deceleration examples [1].	42
Table 3.1. Unidirectional cross-ply and woven fabric comparison.	59
Table 4.1. Woven Kevlar fabric comparison [44].	75
Table 5.1. Sample overview.....	79
Table 5.2. Comparison of sample measurements.	80
Table 5.3. Comparison of mechanical properties from quasi-static testing.....	106
Table 6.1. Comparison of relative density.....	108
Table 6.2. Plate stiffness and predicted maximum stress.	110
Table A.1. West System epoxy properties.....	125
Table A.2. System Three MetlWeld adhesive properties.	126
Table B.1. Values used for calculations of plate stiffness.	127

LIST OF FIGURES

Figure 1.1. Drawing of cork by Robert Hooke, 1664.	3
Figure 1.2. Open-cell polymer foam.	4
Figure 1.3. Example of a closed-cell polymer foam.	4
Figure 1.4. Relative density comparison: a) low density cellular solid, b) solid with isolated pores.	5
Figure 1.5. Wasp's nest, a natural closed cell material.	6
Figure 1.6. Natural sponge, a natural open cell material.	6
Figure 1.7. a) Human skull section, b) section through bird wing [1].	7
Figure 1.8. View of cellular structure of a bovine femur.	8
Figure 1.9. Open-cell aluminum alloy foam with dense facesheets (ERG Aerospace, Oakland, CA).	10
Figure 1.10. Closed-cell aluminum foam (Shinko Wire Co., Japan).	10
Figure 1.11. Cardboard, and example of sinusoidal corrugation.	11
Figure 1.12. Examples of a) regular, b) half, and c) square honeycombs.	12
Figure 1.13. Typical out-of-plane crushing behavior of honeycomb.	13
Figure 1.14. Type 304 stainless steel micro-truss core material [22].	14
Figure 1.15. Corrugated stainless steel fabric cellular solid [6].	15
Figure 1.16. Young's modulus comparison for selected classes of materials.	18
Figure 1.17. Yield strength comparison for selected classes of materials.	18
Figure 1.18. Typical fiber reinforced composite.	19
Figure 1.19. Schematic of glass fiber production [32].	22
Figure 1.20. PAN based carbon fiber production [32].	24
Figure 1.21. Molecular structure of structure of aramid [32].	26
Figure 1.22. Monomer synthesis to produce aramid [44].	27

Figure 1.23. Schematic of Kevlar fiber spinning.....	28
Figure 1.24. Direction definitions for a unidirectional composite.....	38
Figure 1.25. Stress-strain curve for an ideal energy absorber.....	40
Figure 1.26. Example ammunition: a) armor piercing and b) handgun [51]......	46
Figure 2.1. Proposed corrugated Kevlar structure.....	47
Figure 3.1. Axis system for laminated plates.....	50
Figure 3.2. Example of laminate coordinate systems.....	51
Figure 3.3. Stresses on unit of laminae.....	52
Figure 3.4. Example laminate with ten layers (N=10).....	54
Figure 3.5. Example of a symmetrical laminate.....	56
Figure 3.6. Examples of fabric weaves: (a) plain ($n_g=2$); (b) twill weave ($n_g=3$); (c) 4-harness satin ($n_g=4$); and (d) 8-harness satin ($n_g=8$).....	57
Figure 3.7. Fill and warp yarns in a plain-weave element.....	58
Figure 3.8. Section of woven fiber element.....	59
Figure 3.9. Definition of loads and resulting deflection for a rectangular plate.....	60
Figure 3.10. Ideal loading of a wide plate in uniform axial compression.....	62
Figure 3.11. Triangular geometry.....	65
Figure 3.12. Unit of triangular corrugation under compression.....	68
Figure 3.13. Free body diagram of loaded element.....	68
Figure 4.1. Assembly of the proposed sample.....	71
Figure 4.2. Engineering drawing of one half of mold.....	72
Figure 4.3. One half of the finished mold used for layup.....	73
Figure 4.4. Plain weave Kevlar fabric comparison; a) style 120, b) style 281.....	74
Figure 4.5. Removing excess material from layer.....	76
Figure 4.6. Completed single layer of aramid-epoxy.....	77
Figure 4.7. Comparison of different orientations.....	78

1.2 A few steps of history

This chapter does not have the purpose of offering an exhaustive history of helicopter but offers a glimpse at important steps. Leonardo Da Vinci is very often credited for being the conceptual inventor of helicopter. Although his design never took life and apparently could not work, he surely had sensed what the future would offer to mankind. An opportunity to make a human dream come true, a chance to fly in the skies, hover and go rearward.

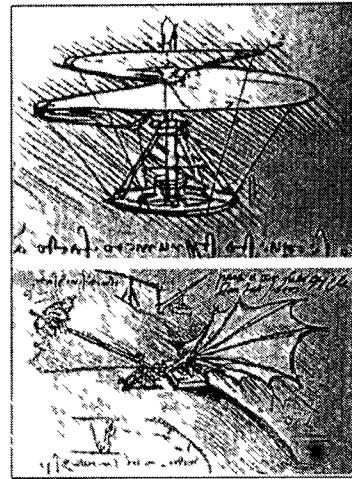


Figure 1: Da Vinci rotor design

In his book “The God Machine”, James R. Chiles [1] describes early inventors’ work and intellectuals’ contribution. The word 'helicopter' is adapted from the French *hélicoptère*, coined by Gustave de Ponton d’Amecourt in 1861. It is linked to the Greek words *helix/helik-* (ἑλίκας) = "spiral" or "turning" and *pteron* (πτερόν) = "wing". D’Amecourt’s efforts were backed up by the famous Jules Verne through, for example, “Robur the conqueror” in which the main character, captain of the Albatross, states: “With her, I am master of the seventh part of the world”.

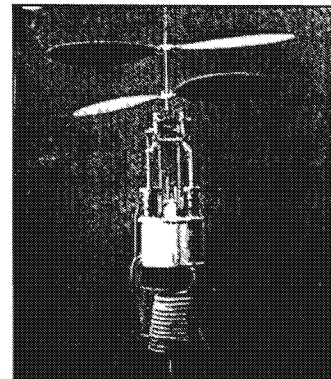
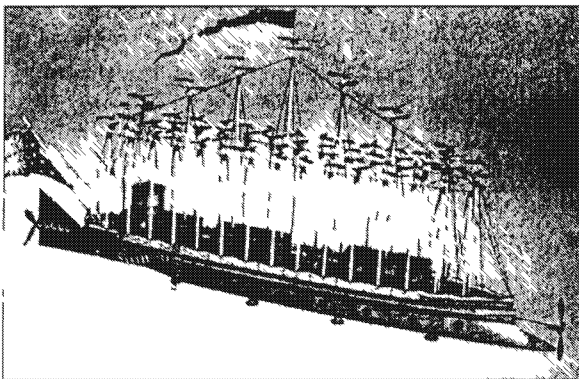


Figure 2: J. Verne’s Albatross & first aluminum counter-rotating coaxial rotor (d’Amecourt)

Figure 5.25. Stress-displacement of sample 8.	103
Figure 5.26. View of sample 8 after penetration test.	103
Figure 5.27. Finished sample 9.	104
Figure 5.28. Stress-displacement behavior of sample 9.	105
Figure 6.1. Predicted densification strain.	109
Figure 6.2. Alporas aluminum foam sample (Shinko Wire Co., Japan).	111
Figure 6.3. Results for quasi-static testing of Alporas.	112
Figure 6.4. Honeycomb used for compression testing (Hexcel Composites, Dublin, CA).	113
Figure 6.5. Results for quasi-static testing of honeycomb.	114
Figure 6.6. Comparison of compressive plateau stress.	115
Figure 6.7. Comparison of energy absorbed per unit volume.	115
Figure 6.8. Hexweb honeycomb with attached aramid facesheet.	116
Figure 6.9. Stress-displacement for honeycomb samples.	117

1. INTRODUCTION

Materials that absorb mechanical energy in a predictable and consistent fashion have been beneficial to designers and engineers for many years. Modern packaging for aerospace, automotive and rail industries are just a few examples where advancements in the realm of energy-absorbent materials have proven beneficial. Furthermore, most consumer items are packaged in some form of protective packaging; and when people board an airliner or drive a car, they are also carefully packaged [1].

The underlying concept for an energy absorbing material is its ability to convert kinetic or explosive energy into some other form of energy, usually heat, while keeping the forces (and therefore deceleration) imparted to the object below some damage threshold. Since almost all packaged objects are transported at some time or another, keeping the amount and weight of packaging to a minimum is important. Through careful design and manufacturing techniques, packaging materials of a desired strength can be made less dense. This leads to lighter packaging materials and better utilization of resources [2].

Puncture and impact resistance are also desirable and beneficial traits for packaging materials. The benefits of puncture resistance were employed by the earliest of hunters and armies to increase their survivability during an attack. With similar goals, modern day armor is known for its ability to resist puncture (knife) and ballistic (bullet) threats. Aramid fibers (manufactured and sold by E. I. du Pont de Nemours under the trademark Kevlar®) were first released during the 1970s. These low density, high strength

materials have made great advances in the field of wearable lightweight personal body armor, among many other applications [3].

If stiff, lightweight, energy absorbing materials which also resist ballistic threats were readily available, such materials would be beneficial to designers and the users of the products they design as structural armor. In this thesis, a method to construct energy absorbent, ballistic resistant materials from woven aramid fiber composites is presented. The compression behavior of the resulting structures is compared to commercially available materials of similar density and character, along with model predictions. Recommendations to improve the performance of the structure are made.

1.1. Cellular Materials

As the word cellular would imply, cellular materials are those which are made of cells [1]. There is generally a repetition in their geometry, although not necessarily ordered or predictable. Cells began to be widely studied in the seventeenth century, when Robert Hooke first examined cork under his microscope, Figure 1.1. It was during these microscopic examinations of plants and other biological structures when the “phenomena of cork” was attributed to its cellular structure in his book *Micrographia* [4].

One feature of cellular materials is that their solid fraction does not always occupy the entire available volume, making them porous and resulting in an overall density reduction. A number of different methods have been developed to employ the benefits of these materials, most commonly as energy absorbing materials, but also as thermal insulators, structural members, buoyant bodies, and others [5]. Polymer foams are excellent examples of cellular materials that possess many of these qualities [1].

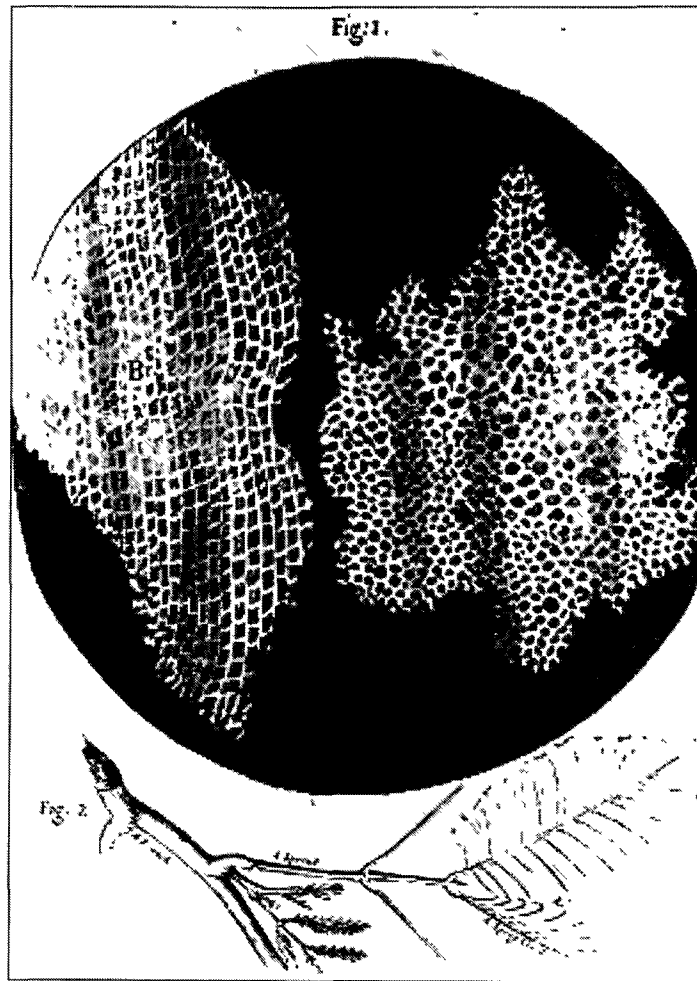


Figure 1.1. Drawing of cork by Robert Hooke, 1664.

Cellular materials are generally classified into two broad categories; open-cell and closed-cell. In an open-cell structure, Figure 1.2, the adjacent cells are freely interconnected. This trait can be useful for flowing fluid through the cells. A closed-cell structure, Figure 1.3, on the other hand, physically isolates adjacent cells from one another. In this type of geometry, each cell is completely enclosed by walls of the base material [6]. Some materials may even possess a combination of open and closed cells. This is called mixed porosity. There are many other geometries and characterizations, as the possibilities are infinite.

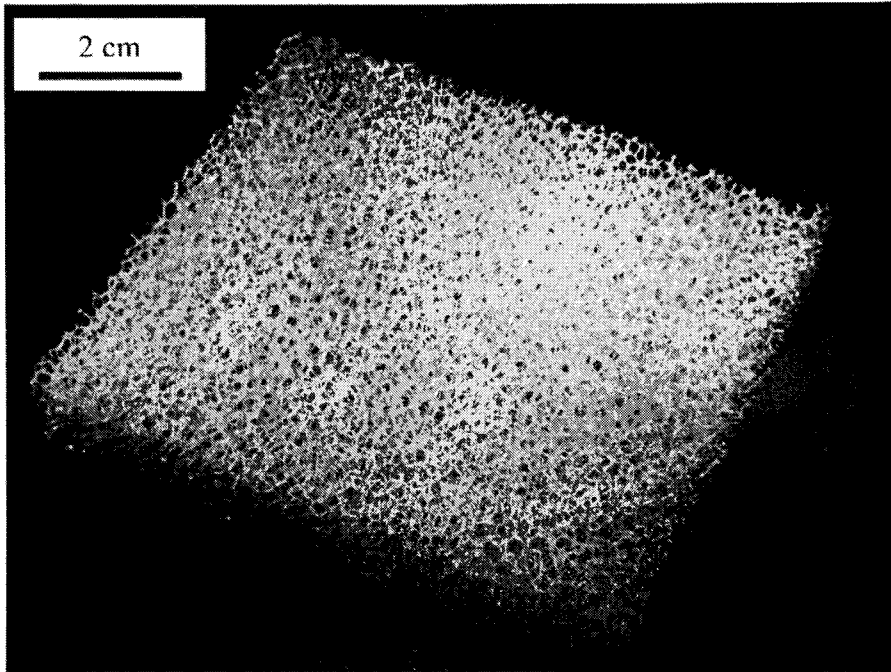


Figure 1.2. Open-cell polymer foam.

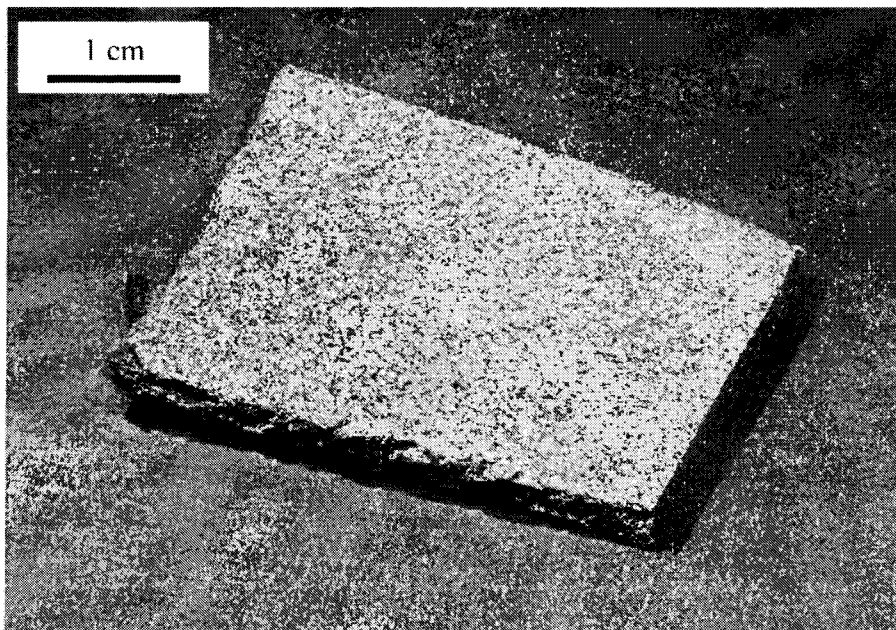


Figure 1.3. Example of a closed-cell polymer foam.

One of the most important features of any cellular solid, regardless of the type, geometry, or base material, is the relative density ρ/ρ_s . Here, ρ is the overall density of the cellular material and ρ_s is the density of its base material. Some ultra-low-density foams have

relative densities as low as 0.001, while common foams for insulation and packaging have relative densities that range from 0.05 to 0.2. Above a relative density of about 0.3, the material is better thought of as a solid with isolated pores, Figure 1.4, as opposed to a true cellular solid [1].

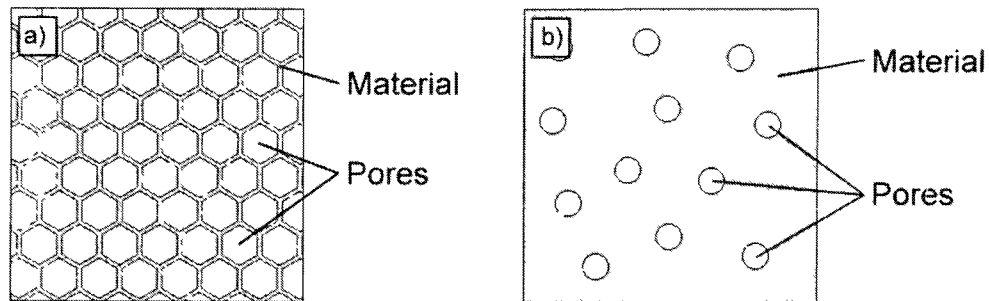


Figure 1.4. Relative density comparison: a) low density cellular solid, b) solid with isolated pores.

1.1.1. Natural Cellular Materials

The most familiar of all cellular materials are those produced by nature; bone, sponge, and wood for example. There are numerous different types ranging from ordered and structured like the honeycomb of a wasp's nest, Figure 1.5, or random, like the open celled structure of natural sponge, Figure 1.6. Wasps and bees use their closed cell honeycomb nests to provide separate chambers for rearing their brood. Bees also use them for storing honey [7]. Marine sponges utilize the open cell layout to encourage feeding by filtration of seawater which flows freely through the cells [8].

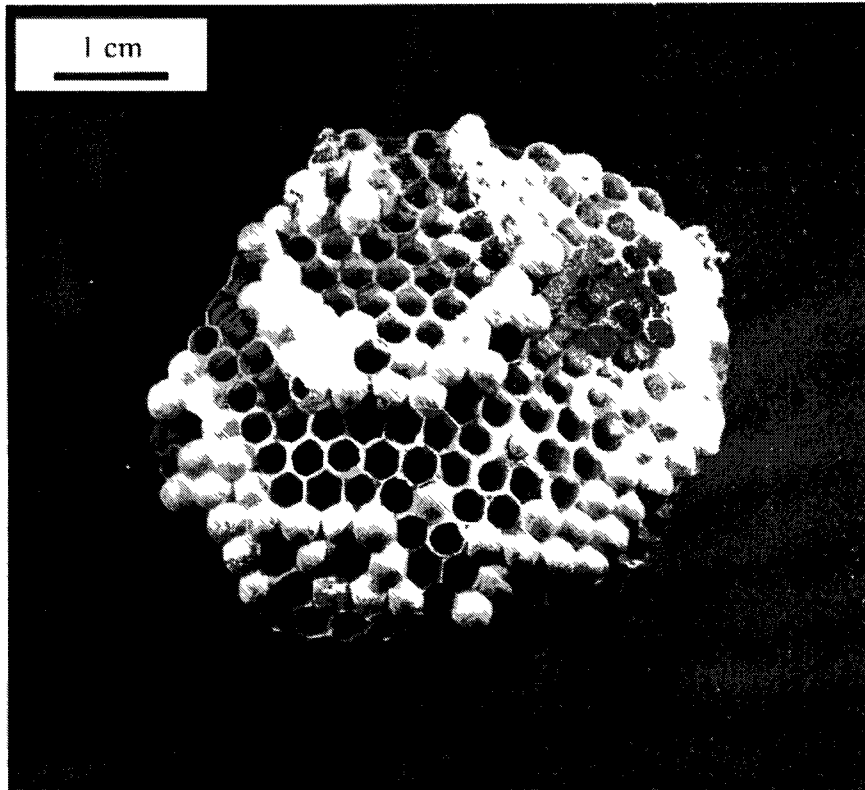


Figure 1.5. Wasp's nest, a natural closed cell material.

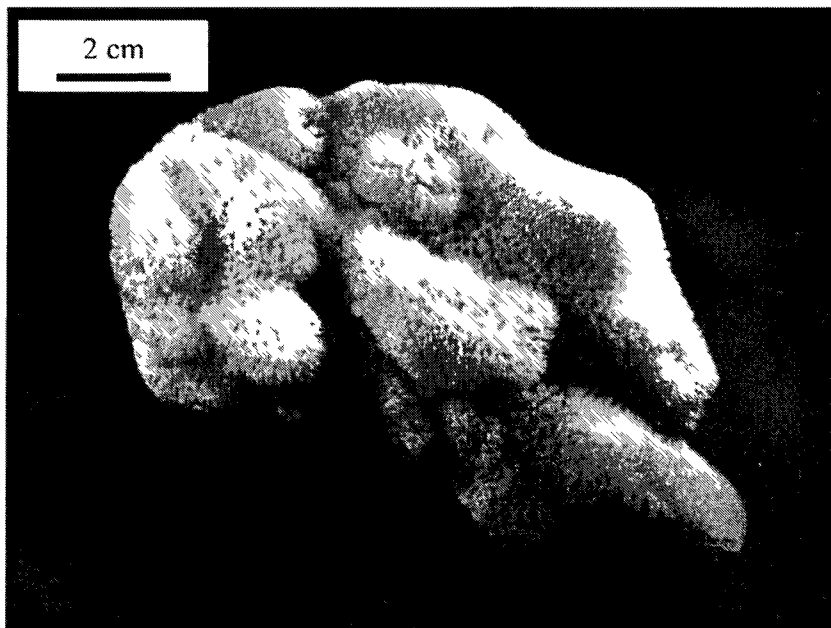


Figure 1.6. Natural sponge, a natural open cell material.

The skull of many animals is cellular with energy absorbing characteristics, partially owing to two layers of dense, compact bone separated by spongy, open-cell cancellous bone [9]. Bones of birds are known to be lightweight and strong, owing partially to a low density core, Figure 1.7. In addition to the energy absorbing characteristics of cancellous bone, the open cells allow for blood production (bone marrow is found there), Figure 1.8.

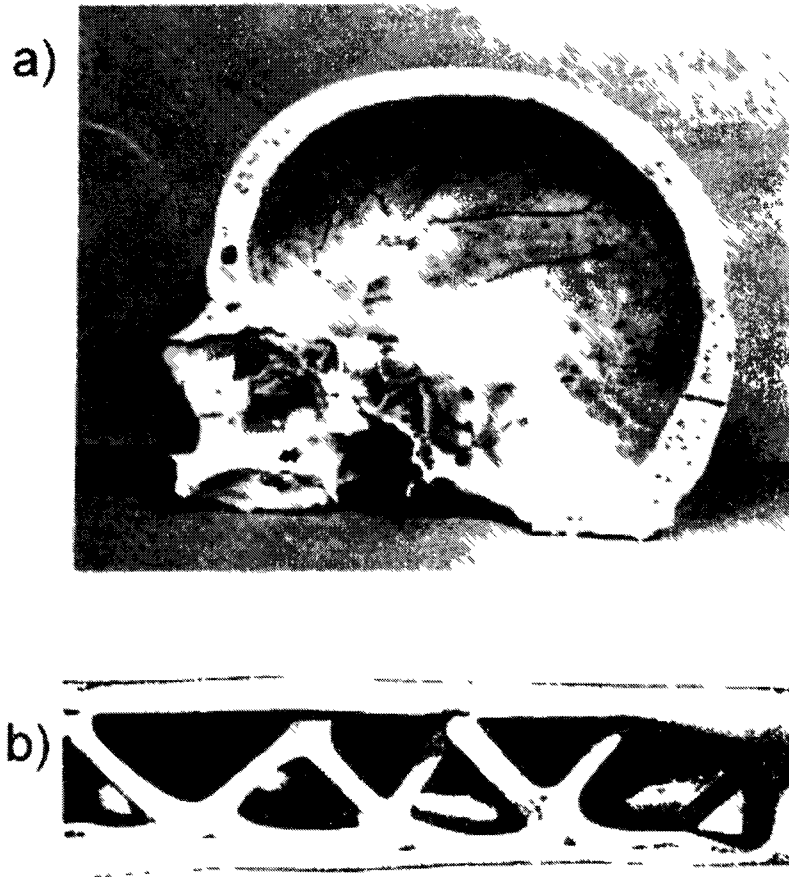


Figure 1.7. a) Human skull section, b) section through bird wing [1].

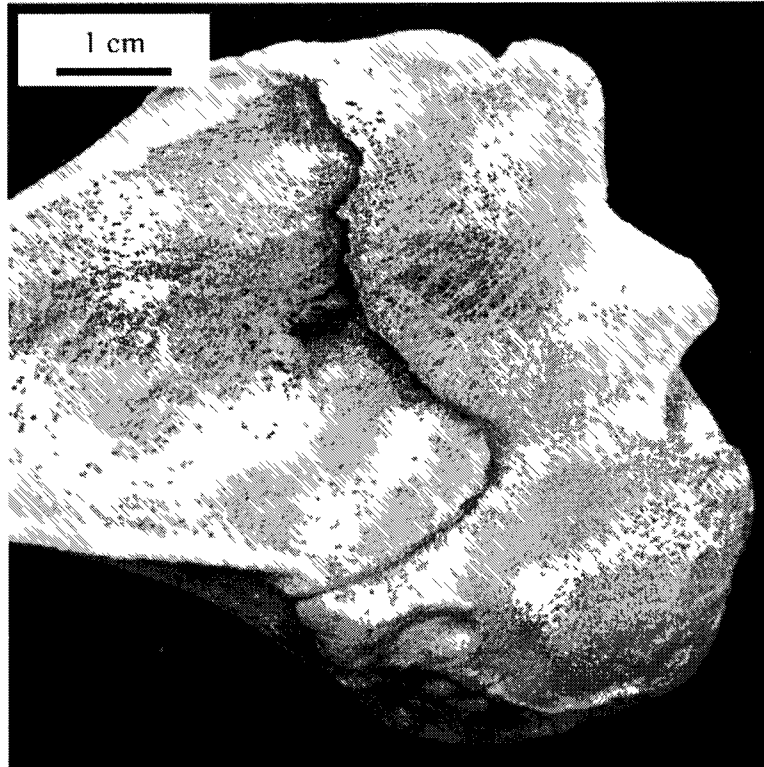


Figure 1.8. View of cellular structure of a bovine femur.

Perhaps the most widely used natural cellular material is wood. This is one of man's most utilized engineering materials. Simple structures, shelters, weapons, parts of modern aircraft and even spacecraft all include parts made from wood [10]. It has been studied extensively owing to a large variety of trees producing a variety of woods having a broad range of structure, density, strength, and cost. The anisotropic behavior of wood fibers has long been known and exploited. Improvements to raw wood have been made by using various treatments, including tar and pitch (used for many centuries in shipbuilding) along with advanced polymers that improve strength, heat resistance, or toughness [11].

In addition to a wealth of data on static stiffness and strength, wood has also been tested under a variety of dynamic conditions [12]. Properties are highly anisotropic and depend

on fiber orientation. To create more uniform properties in a plate-like form, plywood was created. Plywood was also one of the first materials to be treated as a laminated anisotropic plate, the basis for a large group of composite materials [13]. Common disadvantages of wood as compared to other material choices include inconsistency between individual samples, intolerance to moisture, no natural flame resistance, rot, termites, etc. However, wood is usually inexpensive, abundant and renewable, and easy to fabricate into useful articles.

1.1.2. Synthetic Cellular Materials

Synthetic man-made cellular materials include foams (generally stochastic, or random in nature), and geometric or constructed materials such as honeycomb. These cellular materials have seen increasing usage for a number of tasks due to innovations in base material properties, cell geometry, fabrication methods, and reduced cost.

Man-made open and closed cell foams can be further categorized depending on base material type; polymer, glass, ceramic, composite, or metallic. Polymer foams are commonly made of polyurethane or polystyrene. American businesses sold nearly \$16.8 billion of polymer based foam products in 2005 [14]. The use of metal foams is growing as price decreases and quality improves. These can be made from alloys of aluminum, steel, nickel, titanium, and others [15]. An example of an open cell aluminum foam (ERG Aerospace, Oakland, CA) with dense facesheets metallurgically adhered is seen below, Figure 1.9. Also pictured is an example of a closed cell aluminum foam (Shinko Wire Company, Japan), Figure 1.10.

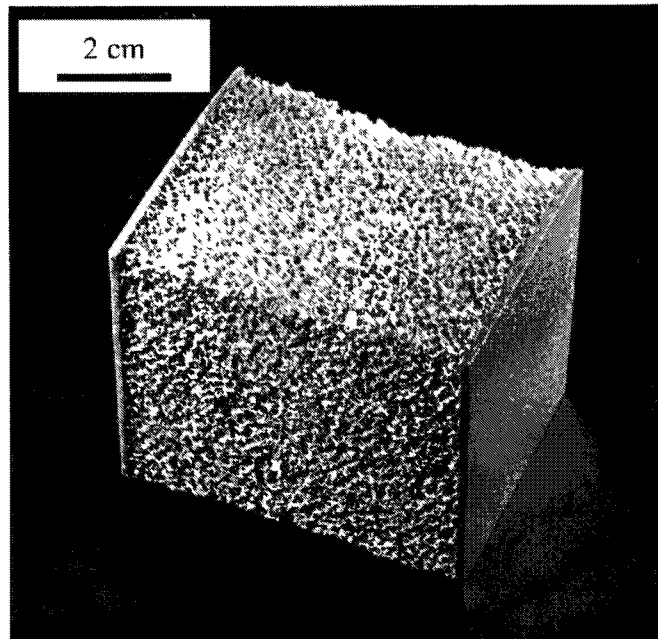


Figure 1.9. Open-cell aluminum alloy foam with dense facesheets (ERG Aerospace, Oakland, CA).

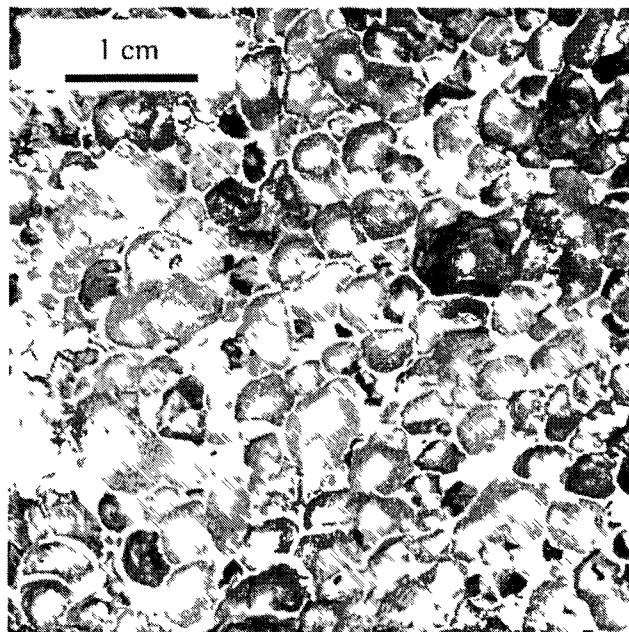


Figure 1.10. Closed-cell aluminum foam (Shinko Wire Co., Japan).

Prismatic forms of cellular solids can be made by stacking corrugated sheets. A type of prismatic corrugation which has been widely used in industry is the sinusoidal corrugation, commonly used in paperboard packaging (cardboard), Figure 1.11.

Sinusoidal layers are simple to construct from a variety of base materials (e.g., metal, paper, and composite) as well as easy to assemble into multi layer products with thickness to suit the intended use.

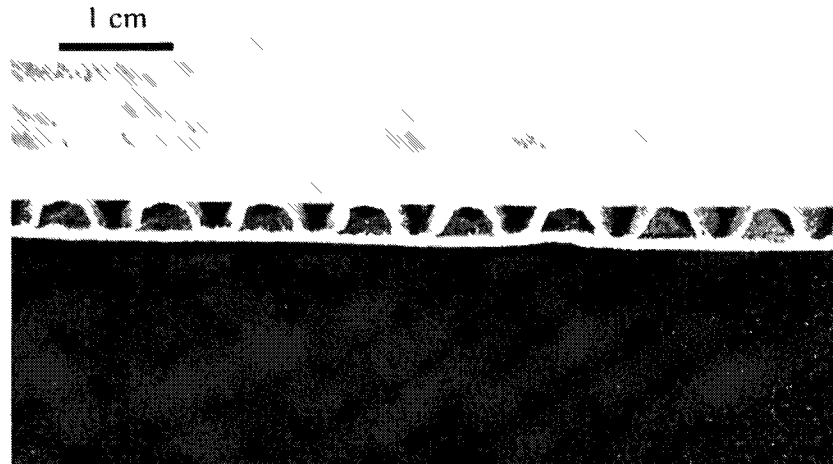


Figure 1.11. Cardboard, and example of sinusoidal corrugation.

If properly utilized, the concept of a corrugated core can provide weight and space savings, fire resistance, noise control, and improved thermal (heating and cooling) behavior [16]. However, corrugated core sandwich panels have not been the subject of a great deal of scholarly research. In one article dating back over 40 years, this material was suggested as a bulkhead material for naval ships, but welding and manufacturing difficulties slowed its adoption. Trapezoidal core sandwich panels have been the subject of blast protection research in recent years, also with naval applications in mind [17, 18].

When the fluting of a material is oriented to produce cells with six-sided walls that resemble beehives, the resulting structure is generally known as regular honeycomb. Figure 1.12. This structure can be made from a number of base materials including metals, composites (e.g., Nomex), paperboard, and more. The cells can also take on

square, triangular, and other shapes. A look into the history of these materials documents their use as structural materials in a number of industries. Particularly, as the cores of stiff, lightweight sandwich structures. Honeycombs are also well known for their excellent energy absorbing characteristics.

While the hexagonal shape is by far the most widely used honeycomb architecture, there are variations. For example, half-honeycomb is similar to the full honeycomb (already discussed), with an additional rib in one out-of-plane direction. Square honeycomb, with two sets of parallel ribs oriented at 90-degrees, is another variation shown in Figure.1.12.

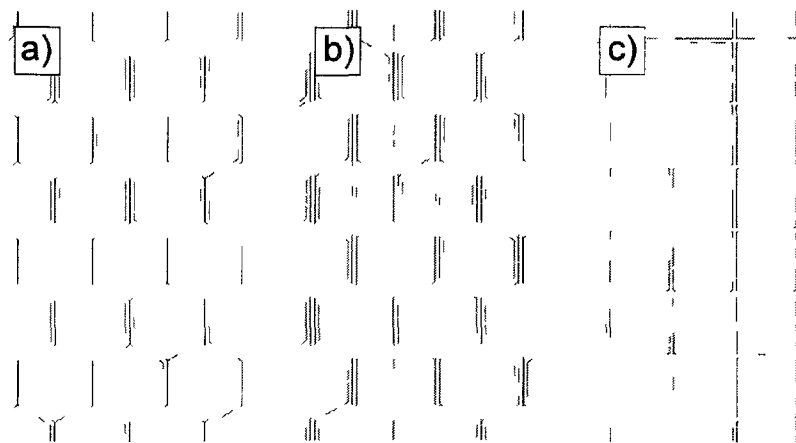


Figure 1.12. Examples of a) regular, b) half, and c) square honeycombs.

Honeycombs have been widely utilized in the aerospace industry. For example, the B-70 has an airframe that is over 70% stainless steel honeycomb [10]. Another use of honeycomb in aerospace is as an energy absorbing core. The de Havilland “Dash 8” DHC-8 meets Federal Aviation Administration (FAA) bird strike requirements by using aramid-based honeycomb core in wing leading edges. In this application, the honeycomb core sandwich panels can be readily formed to the required shape of the airfoil [19].

While honeycombs are excellent energy absorbers, there are issues when compressing them because of a high initial peak stress. The energy absorbing cell walls that yield/buckle under compressive loading must first instigate this behavior with a high peak stress, followed by crushing at a lower plateau stress as crushing proceeds, Figure 1.13. The danger with a high peak stress involves the high peak forces, and therefore a high initial deceleration, which can damage the object the honeycomb is designed to protect.

Such findings have been observed for a number of honeycombs in both quasi-static and dynamic loading conditions [20, 21]. While impressive as energy absorbers, honeycombs offer little penetration resistance, and adjacent cells are not available to communicate with each other, as it is a closed-cell material.

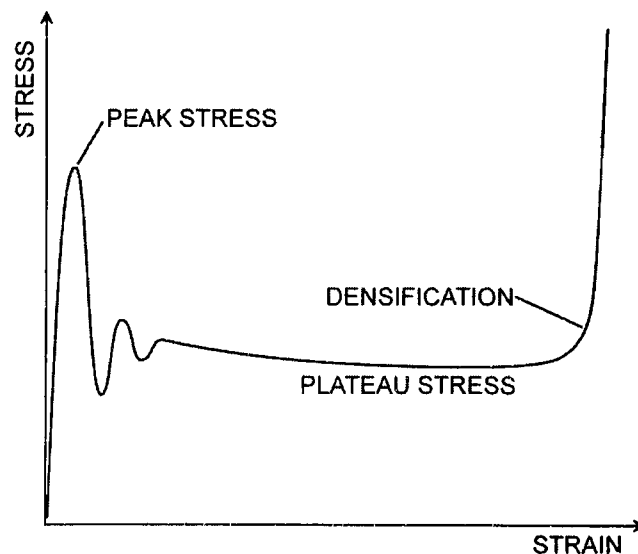


Figure 1.13. Typical out-of-plane crushing behavior of honeycomb.

While manufacturing techniques and performance of honeycombs continue to improve, other competing materials have been developed. A recent advance in cellular materials is in the form of micro-truss structures [22]. Miniature truss structures of this type have

been constructed using a number of techniques, including rapid prototyping, injection molding, investment casting, and sheet perforation/bending/bonding approaches. Their design and appearance resembles truss structures used in skyscrapers, bridges, and the like that have been studied and utilized for many years [5]. Starting with a relatively simple shape or base material (such as sheet metal or woven wire) one can create a truss-like sandwich structure core, such as that in Figure 1.14.

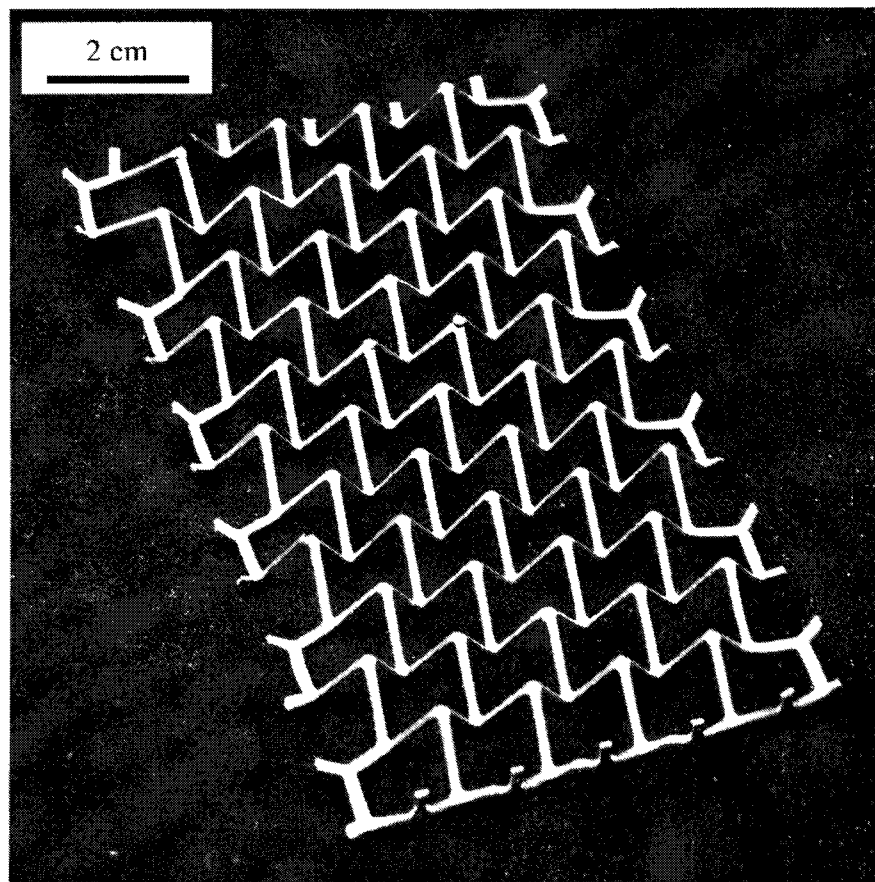


Figure 1.14. Type 304 stainless steel micro-truss core material [22].

Within the past few years, a method to create cellular materials made from woven metallic textiles has also been reported [2]. Testing of these materials shows them to be viable energy absorbers. Research by Choi [6] involved corrugating woven stainless

steel fabric, laminating and then bonding to create low-density cellular solids, Figure 1.15. A number of fabric densities were examined. Following compression testing, open-cell stochastic foam models were shown to reasonably predict the crushing strength of these open cell corrugated cellular solids.

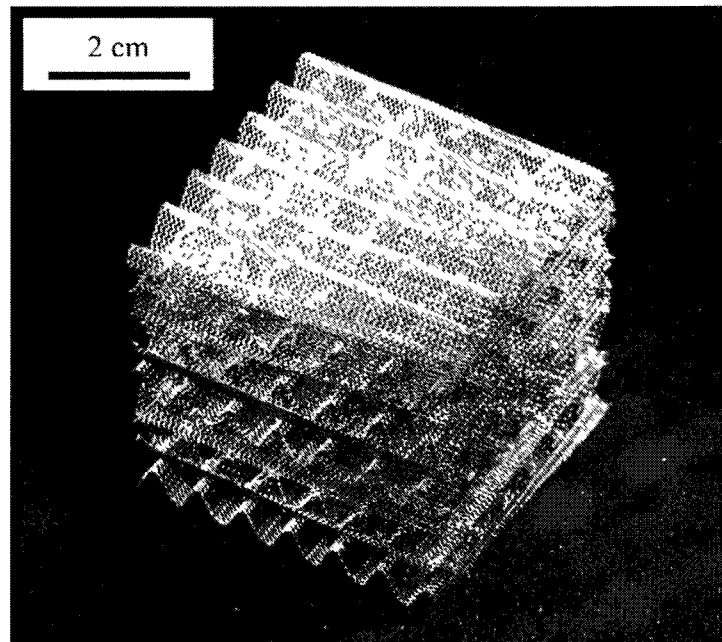


Figure 1.15. Corrugated stainless steel fabric cellular solid [6].

A search of the literature reveals another design for energy absorbing materials involving egg crate materials. These materials have been shown to outperform other foams, with characteristics similar to honeycombs [23]. Yet another design involves folding flat sheets into three dimensional “chevron patterns,” then laminating to make a low density cellular solid [24]. An advantage of the folding techniques is that a number of common materials, such as paperboard, metals, composites and plastics can be adapted, keeping the cost of the cellular material down. Recent research involving these types of materials illustrates their potential application as an energy absorber similar to honeycomb [24].

Uses for the cellular materials continue to grow, and energy absorption has been an important application and topic of research. Since most energy absorbing applications involve high rate loading, investigation into strain rate effects on compression behavior for a number of foams and honeycombs has been conducted. The complex behavior of certain cellular materials, particularly foams, must be observed through testing. Some reports show no strain rate dependence for open cell, aluminum alloy foams [25]. Other reports, for aluminum syntactic foams, show an increase in peak stress of 10-30% under dynamic conditions [26].

A number of product applications are finding that performance can be improved through the use of cellular materials discussed above. One such use is as a lightweight core, where stainless steel foams have been shown to help reduce the weight of turbine fan blades, while simultaneously improving the vibration characteristics [27]. This improvement provides the benefit of removing the vibration damping snubbers which are located mid-span on the blade. Employing these design concepts reduces weight and the number of blades while increasing aerodynamic efficiency [27].

In addition to their use as energy absorbers and cores in sandwich structures, cellular materials have found other interesting applications. The open cell nature of certain cellular materials can be utilized for the storage of gases and liquids (fuel, water, etc.) with little loss in useable space [5]. Furthermore, these types of cellular materials can also be used as heat exchangers. Current research seeks to characterize the performance of these devices, and it has been found that they are viable heat exchangers [28, 29].

1.1.3. Performance of Cellular Materials

As a general rule, all of the cellular materials (both natural and manmade) discussed in the previous section have a density less than that of nonporous metals, ceramics, or other engineering materials. Properties other than density (e.g., mechanical and electrical) are important for comparison as well. An effective way to see trends of certain classes of materials is using the Cambridge Engineering Selector [30] software package (by Granta Design Ltd). This program compiles a large database of material properties and allows graphing and quick comparisons.

The power of this tool lies in a user's ability to select certain materials for comparison, or to view all materials within a selected range for a given property. Material properties within the database include mechanical properties, electrical properties, environmental, cost, and more. Hyperlinks to sources for the materials are also provided within the program. Compared to handbooks and manual searching for material properties, the CES software package is a powerful time saver.

For comparative purposes, Young's Modulus, E , was plotted as a function of density, Figure 1.16. The general trend shows that denser materials have higher stiffness. The distinction of different classes of materials is also important; synthetic polymer foams are light and compliant, while ceramics are heavy and stiff. In the plot, the large groupings of materials represent different classes of materials (e.g., polymers, glasses, metals, etc.). The smaller areas (darker in color) are more specific materials, whose labels were omitted for clarity.

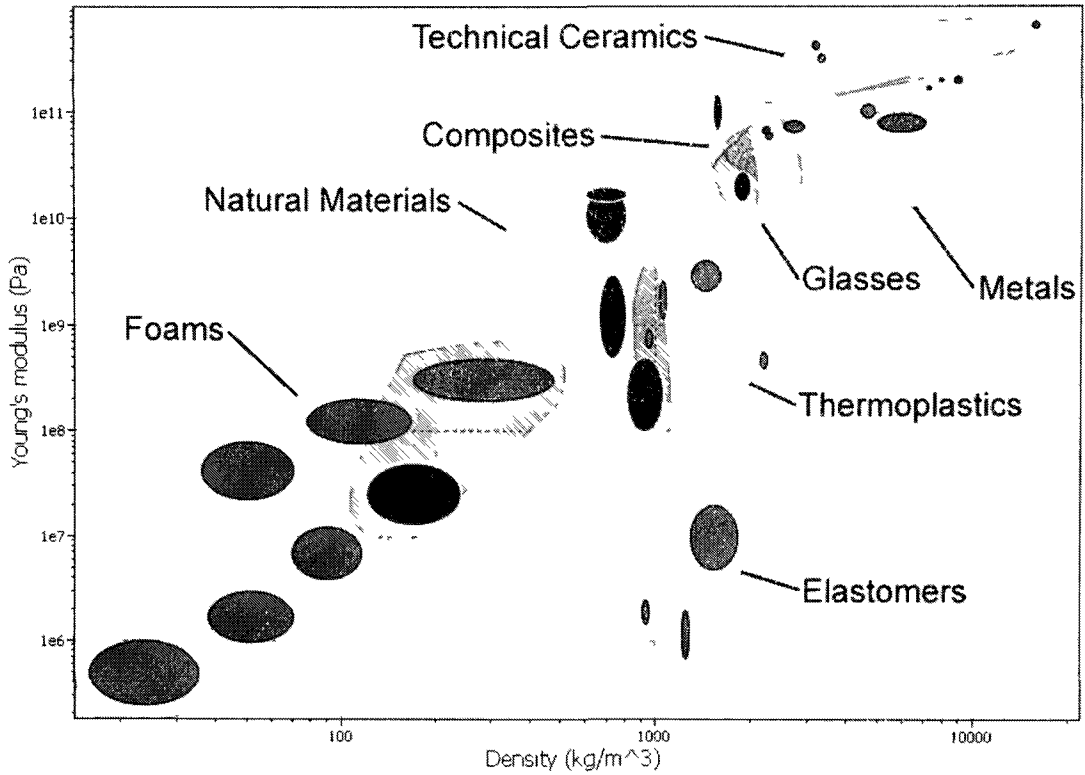


Figure 1.16. Young's modulus comparison for selected classes of materials.

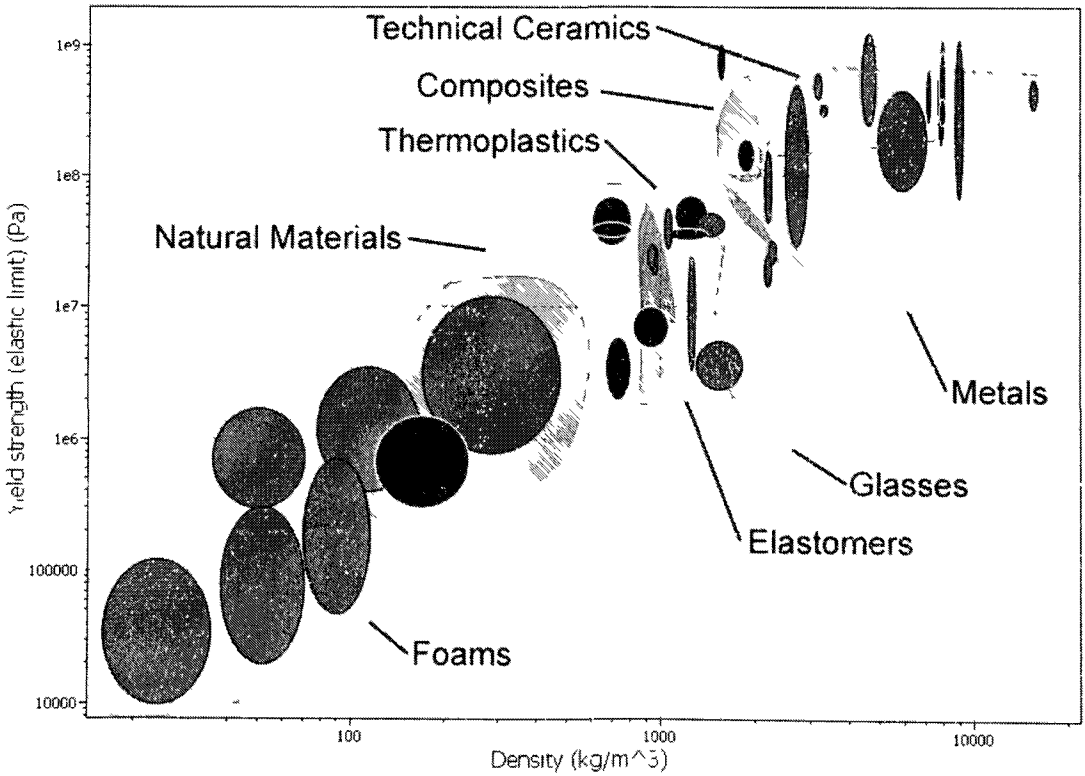


Figure 1.17. Yield strength comparison for selected classes of materials.

Yield strength follows a similar trend, where strength increases with increasing density, Figure 1.17. Woods (natural materials) and dense foams occupy the intermediate range of the data. The materials included in this comparison are the same as those seen in the stiffness comparison.

1.2. *Fibrous Composites and Applications*

Composite materials are engineered materials made of two or more constituent materials (called the reinforcement and matrix) with significantly different properties [31]. A common composite material is reinforced concrete used to pave roadways and bridges. This is made of steel reinforcing bars set within a hardened concrete (Portland cement, gravel, sand, and water) matrix. Fibrous composites, on the other hand, are commonly made of polymer, ceramic, glass, or metallic reinforcing fibers set within a polymer, metal, or ceramic matrix, Figure 1.18.

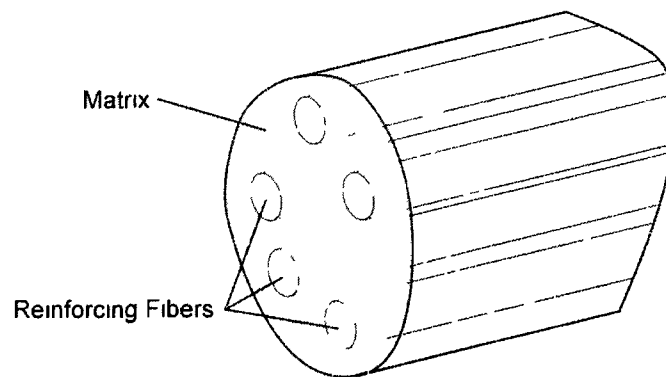


Figure 1.18. Typical fiber reinforced composite.

The fibers in a composite material normally carry a majority of the load while the matrix holds the shape of the composite, transfers load between fibers, and protects the fibers from the environment (e.g., abrasion, chemicals) [32].

Among today's fibrous composite materials, glass fiber reinforced composites are the most widely used. When glass fibers are used with an epoxy matrix, boat hulls, surfboards, and homebuilt aircraft are some of the applications. The resulting composite is usually referred to as "fiberglass." When used with less expensive matrices (which are generally lower strength), these glass fiber composites are usually used in non-structural application such as body panels or aerodynamic fairings for cars and motorcycles [33].

1.3. *Fibers*

Fibers have been used by humans for many thousands of years; the natural fibers of the jute plant, flax (linseed), and hemp have been used for rope, cordage, nets, and clothing. Synthetic fibers; those not from natural sources (plant, animal, or mineral) have gained popularity compared to their natural counterparts, due to their excellent performance and higher degree of uniformity [34]. Nylon, rayon, and spandex are all examples of synthetic fibers invented during the twentieth century.

While the term "fiber" generally refers to a single continuous fiber, very commonly they are grouped together. When they are combined into a group at a basic level, the result is referred to as a strand. A yarn is an assemblage of these strands, and usually refers to those with fewer than about 10^4 fibers. When greater than 10^4 fibers are present, the result can be referred to as a tow [35]. If a yarn (or tow) is used in a woven fabric, the yarn can be called an end, and are specified based on their direction as fill ends (running perpendicular to the fabric) or warp ends (running lengthwise with the fabric).

1.3.1. Glass Fibers

Glass has been widely used as a structural material over the last century or so (as load bearing panes in buildings), and as a composite reinforcing material for perhaps fifty years. Glass fibers usually contain large percentages of silicon dioxide (SiO_2), and depending on the type, may contain traces of aluminum oxide (Al_2O_3), magnesium oxide (MgO), and more [36]. Since glass is made mostly from noncrystalline amorphous silicates (some of the most abundant resources on Earth), glass has the benefit of not being petroleum dependant. Two of the most common types of glass fibers are the “E-glass” and “S-glass”; these have slightly different compositions and properties. While E-glass was originally intended for electrical applications, S-glass was developed as a high strength fiber, but it costs more [35].

Production of glass fibers begins with melting of glass marbles or batch in a furnace heated to around 1400 °C [32]. The glass batch in the furnace has the desired composition, and must be mixed thoroughly to ensure consistency in the final product. From the furnace, the liquid glass is cooled to 1250 °C and flows into a bushing (or spinet) that has a large number of holes (between several hundred and several thousand) with diameters that can range from less than one mm to several millimeters. The emerging glass is drawn into fibers at very high speed; up to 54 m/s [35]. They are rapidly cooled by a fine water spray, coated with a sizing agent (for environmental protection, abrasion resistance, and an increase in bond strength with the matrix), and combined into a strand (or tow) in an assembler, then wound onto a spool. This process is shown schematically below, Figure 1.19.

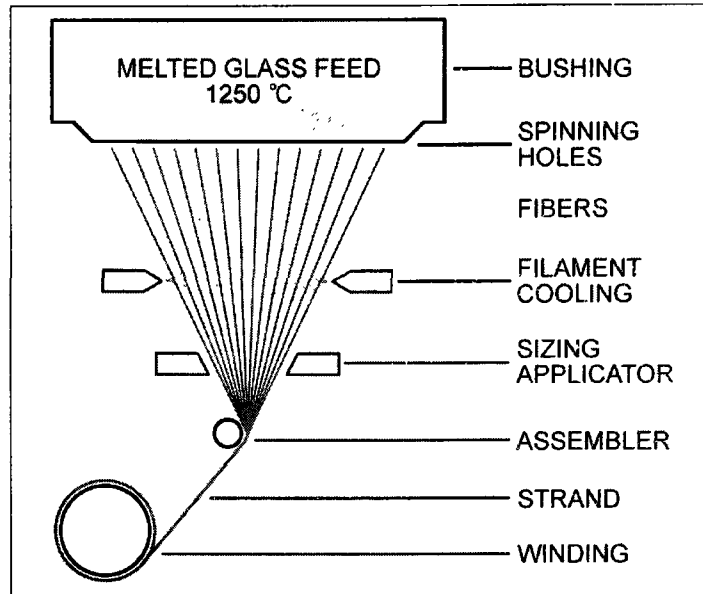


Figure 1.19. Schematic of glass fiber production [32].

The fiber diameter can be controlled by adjusting the viscosity of the melt, size of holes in the bushing, and the rate of winding. A typical strand of glass fiber has 52, 102, or 204 fibers within it, depending on the exact manufacture process [32]. The strands can be further processed, depending on the desired final product. Glass fibers are widely available as continuous filaments, cut or chopped strands, and yarns, which are arranged in the form of cloths, mats, or tapes. The wide variety of choices makes them attractive for a variety of applications and wide ranging fabrication processes [35]. Advantages of glass fibers, compared to others, include their low cost per unit weight (or volume), chemical/galvanic corrosion resistance, and inertness (not chemically reactive) [37].

1.3.2. Carbon Fibers

Carbon fibers are a category of stiff, strong fibers which have become synonymous with high tech sports equipment (e.g., bicycles, racquets, fishing poles, etc.), and aerospace vehicles [38]. They are commonly referred to as “graphite”, although there is a

difference between these two products, as carbon fibers do not contain graphite structures of carbon [35, 37, 39]. Although expensive compared to many other materials, the performance of these synthetic, inorganic fibers is so good that they are becoming the state of the art choice for many applications. Carbon and graphite manufacturing sales exceeded two billion dollars in 2005 in the United States [14].

The properties of carbon fibers can vary widely, depending on the raw material (or precursor) and process used. The vast majority of today's carbon fibers are made from three different precursor materials; rayon, polyacrylonitrile (PAN), and pitch. First generation, more expensive carbon fibers were based on a precursor material of rayon, but were gradually phased out in favor of the second generation fibers based on PAN [35]. The third generation of fibers, which further reduced costs and increased performance, are based on pitch, a residue from the pyrolysis of organic materials, containing complex mixtures of aromatic hydrocarbons [39]. Today, both PAN and pitch types are popular and can be selected to fit the intended application by tradeoff of cost, strength, stiffness, and thermal behavior. Carbon fibers can be purchased as woven fabric or unidirectional cloths and tapes, and it can be blended with aramid fibers to create hybrid fabrics that share the benefits of the two fiber types [32].

Depending on the precursor material, there are slightly different methods for making carbon fibers. The PAN based carbon fibers start with a tow or yarn of PAN fibers, which usually contains about 10^4 fibers (although much larger and smaller tows can be produced). First, the PAN fibers are placed in an air oven at around 250 °C, to stabilize the polymer. The next step is carbonization, where fibers are passed through an inert atmosphere of nitrogen between 1200 °C and 1600 °C. It is during this heat treatment

process that the aromatic network transforms to mainly carbon atoms and becomes more dense [32]. One important distinction of the PAN fiber process is that the fibers must remain in tension as they are heated. Schematically, this process is shown in Figure 1.20.

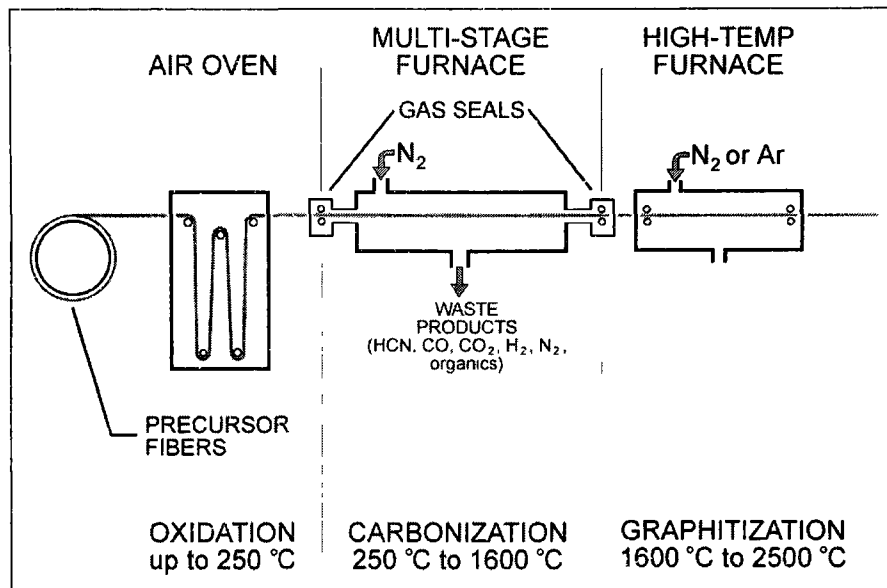


Figure 1.20. PAN based carbon fiber production [32].

For even higher modulus fibers, a final stage of heat treatment can be performed. Such treatments are completed at temperatures up to 2500 °C in a clean and highly inert atmosphere, such as argon. This final stage, called graphitization, results in a change to the three dimensional crystalline structure [39]. The performance of the end product is not only affected by the specific process and heating, but the nature and content of weakening voids (determined largely by the quality of the PAN precursor). Starting with higher quality PAN fibers usually leads to increased strength and stiffness, but also results in a higher cost for the final product [32].

Pitch based carbon fibers are made using a similar method. First, the organic compounds of the pitch precursor (solid at room temperature) are heated into a liquid

crystal phase at 400-500 °C and the fibers are then spun. They are then heated in an atmosphere containing oxygen at 300 °C to cross link the fibers before pre-carbonizing at 1000 °C. Lastly, carbonization and graphitization processes are completed at higher temperatures (1200 to 3000 °C). The main advantage of pitch processing is that no tension is required to maintain or develop the molecular orientation required for high strength and stiffness. This is due to the anisotropic liquid crystal nature of the pitch, as proper molecular orientation is achieved during spinning [32].

Carbon fiber based composites have been used in a number of aerospace vehicles, including advanced fighter aircraft (such as the F/A-18E/F) [32]. Disadvantages of carbon include its potential for a galvanic reaction with metals such as aluminum, lower strain to failure than other fibers and high cost. The high cost can often be justified through weight savings and higher stiffness, such as that needed in aerospace and sporting goods products.

1.3.3. Aramid Fibers

Aramid fibers, produced by DuPont under the trademark Kevlar®, were created during the mid 1960s from polymers [3]. These fibers are also produced by Teijin and Akzo Nobel under the names Technora® and Twaron®, respectively. Aramid is an *aromatic polyamide*, meaning that it is a structure of aromatic carbon rings produced from two monomers that are joined to form peptide bonds, Figure 1.21 [40]. The result is a fiber with high strength to weight ratio and applications in a number of industries. It is inherently flame resistant, has good thermal stability, and resists acids, alkalies and hydrocarbons [3].

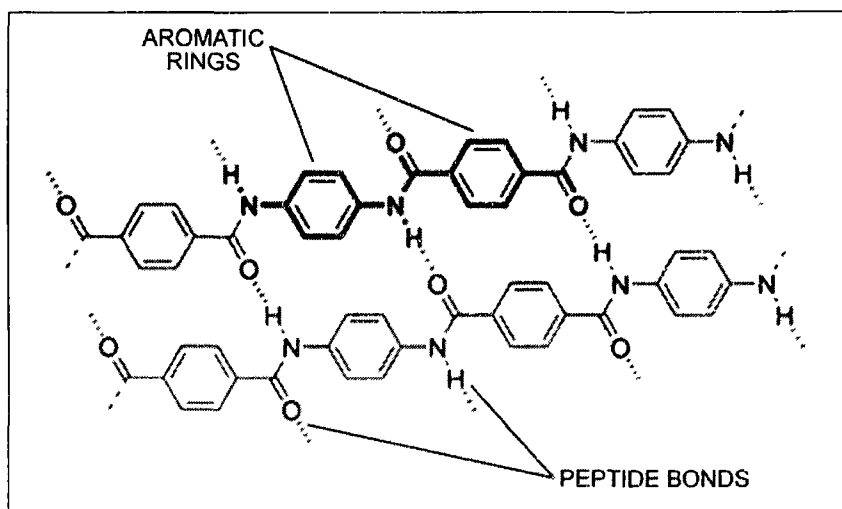


Figure 1.21. Molecular structure of structure of aramid [32].

Initial trials as a reinforcement with epoxy resins produced a high strength material that quickly led to use in aircraft (e.g., Lockheed L-1011, Boeing 767, Airbus A310), rockets (e.g., Trident I, Pershing II, MX, and NASA Space Shuttle), as well as high-performance boats including the CG-67 missile cruiser and USCG cutters [41, 42]. Additionally, it was widely accepted as a belting material in tires, often replacing steel since it made a lighter product with lower rolling resistance [3].

Perhaps its most famous application is in the ballistics arena, where “Kevlar 29” is used to create soft bulletproof vests (beginning in the mid-1970s). This is partly due to the toughness of the aramid fiber (energy absorbed before failure), which on a per weight basis is higher than nearly all glass and carbon fibers. Most of the increased energy absorption is due to its higher strain at failure [43, 35]. For personnel protection, this beneficial characteristic is utilized in the form of gloves, chaps, sleeves, coats and hoods that protect from abrasion, cuts, and also heat.

Producing aramid involves two monomers; the first is terephthaloyl chloride (an acid chloride), and the second is para-phenylenediamine (an aromatic amine). Combining these produces the aramid polymer chain along with hydrochloric acid as a byproduct, Figure 1.22.

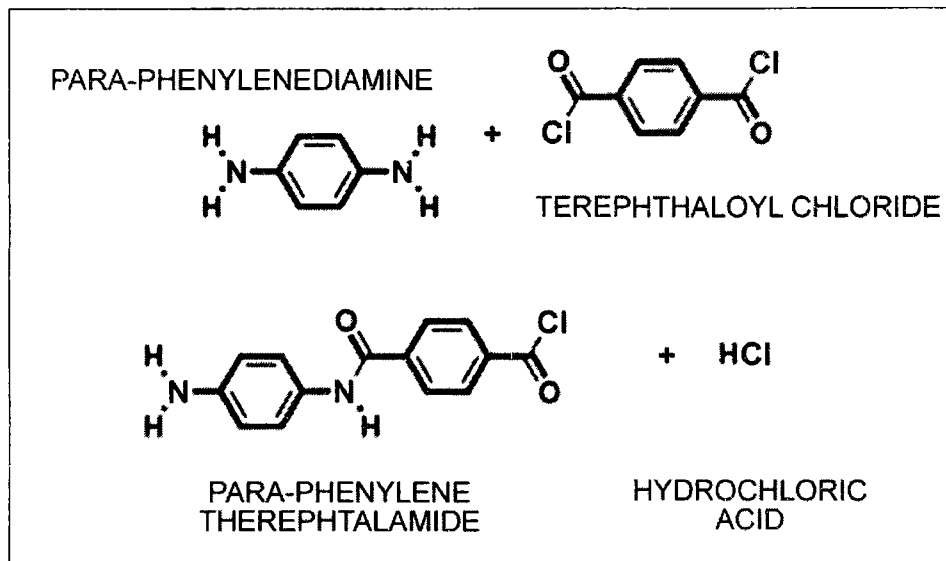


Figure 1.22. Monomer synthesis to produce aramid [44].

Spinning of aramid into fibers begins by mixing the aramid polymers as a solution with a pure sulfuric acid (no water) at around 100 °C. The solution is then extruded through a spinneret, where it passes through a short air gap before entering a water bath to rinse off the acid, Figure 1.23. The resulting fiber structure is highly crystalline, with aligned chains of the aramid polymer.

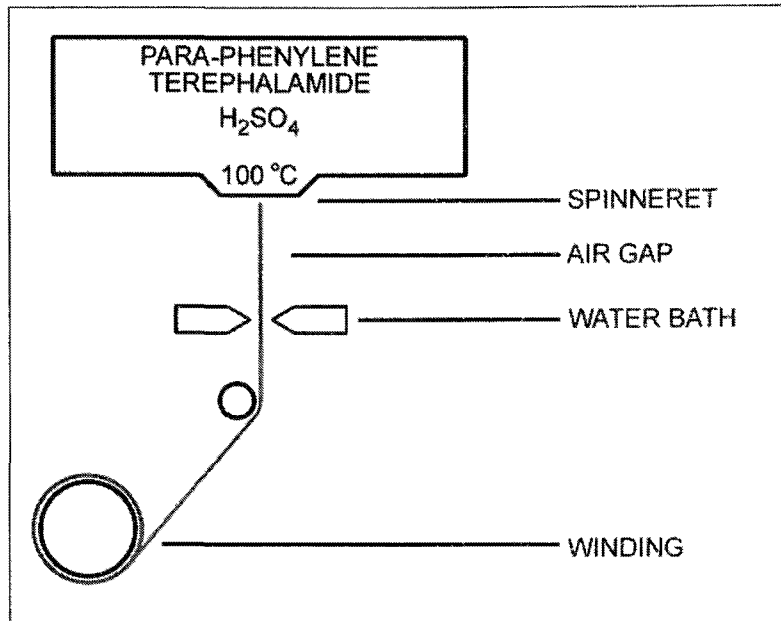


Figure 1.23. Schematic of Kevlar fiber spinning.

While Kevlar consists of woven aramid fibers spun from aramid, another form known as Nomex® can also be made. Here, the final product involves unaligned fibers (paper-like) in the form of a sheet. It is commonly used as a honeycomb core in sandwich structures. Nomex® is manufactured in a different manner than continuous strands of aramid fiber (such as those in woven fabric), but it offers many of the same benefits of traditional aramid. It is tough yet flexible, flame resistant, and won't fracture under compression. Like Kevlar®, Nomex® is also used for making flameproof, protective clothing (e.g., flight suits, gloves, etc.) [45].

When compared to other fibers, major drawbacks for aramid fibers include lower stiffness and tensile strength, sensitivity to UV light, and lower compressive strength than other materials [35]. Cutting, drilling, and machining aramid composites can be problematic due to the toughness of the fibers, and may require special carbide-tipped

tools. Water jets (high velocity water containing abrasives and lubricants) can be an excellent method for cutting aramid composites [32].

1.3.4. Fiber Comparison

Some important physical properties of common synthetic fibers are shown below, Table 1.1. These are general properties for the type listed; other types are commercially available with differing properties. The sources report different values; a range is given to represent differences seen in the literature.

Table 1.1. Fiber properties.

Fiber	Tensile Strength (GPa)	Modulus (GPa)	Failure Strain (%)	Fiber Diameter (μm)
Glass Fibers				
E-Glass	3.4-3.5 ^{[35],[42]}	72-73 ^{[32],[42]}	3.5-4.4 ^{[32],[37]}	4-13 ^[42]
S-Glass	4.5-4.6 ^{[35],[42]}	86-87 ^{[32],[42]}	4.5-5.3 ^{[32],[37]}	8-14 ^[32]
Carbon Fibers				
PAN Carbon, HS (i.e., T300)	3.5-3.53 ^{[32],[37]}	230 ^{[32],[37]}	1.5 ^{[32],[37]}	4-8 ^{[32],[42]}
PAN Carbon, HM (i.e., M50)	2.45-2.5 ^{[32],[37]}	490 ^{[32],[37]}	0.5 ^{[32],[37]}	4-8 ^{[32],[42]}
Pitch Carbon, HM (i.e., P100)	2.2-2.41 ^{[32],[37]}	725-758 ^{[32],[37]}	0.3-0.32 ^{[32],[37]}	8-11 ^{[32],[42]}
Aramid Fibers				
Kevlar 29	3.6-3.8 ^{[37],[42]}	80-83 ^{[32],[42]}	3.6-4.0 ^{[32],[44]}	12 ^{[32],[44]}
Kevlar 49	3.6-4.1 ^{[37],[42]}	124-131 ^{[37],[42]}	2.8 ^{[32],[44]}	12 ^{[32],[44]}
Kevlar 149	3.4-3.6 ^{[37],[42]}	173-179 ^{[37],[42]}	1.5-2.0 ^{[32],[44]}	12 ^{[32],[44]}

Observe that carbon can be made to be the strongest of the three fiber types discussed here. However, Kevlar is the least dense, giving it a higher specific strength (strength divided by specific gravity) and specific stiffness (stiffness divided by specific gravity) than fiberglass and some carbons,

Table 1.2. Carbon is also expensive, known to exhibit a brittle failure, and has little to no post-failure load bearing capacity [43].

Table 1.2. Specific fiber strength and modulus.

Fiber	Specific Gravity	Specific Strength (GPa)	Specific Modulus (GPa)	Max Operating Temperature (°C)	Approx Cost (\$/kg)
Glass Fibers					
E-Glass	2.5-2.6 ^{[35],[42]}	1.31-1.40	27.7-29.2	350-550 ^{[32],[37]}	1.7-3 ^[35]
S-Glass	2.5 ^{[35],[42]}	1.80-1.84	34.4-34.8	650 ^[37]	22-30 ^[35]
Carbon Fibers					
PAN Carbon, HS (i.e., T300)	1.75-1.76 ^{[32],[37]}	1.99-2.00	130.7-131.4	>2000 ^[32]	50 ^[35]
PAN Carbon, HM (i.e., M50)	1.90-1.91 ^{[32],[37]}	1.28-1.31	256.5-257.9		44-220 ^[42]
Pitch Carbon, HM (i.e., P100)	2.15-2.16 ^{[32],[37]}	1.02-1.12	335.6-352.6	>2000 ^[32]	88-440 ^[42]
Aramid Fibers					
Kevlar 29	1.43-1.44 ^{[32],[37]}	2.50-2.65	55.6-58.0	250 ^[32]	
Kevlar 49	1.45 ^{[32],[37]}	2.48-2.83	85.5-90.3	250 ^[32]	50 ^[42]
Kevlar 149	1.47 ^{[32],[37]}	2.31-2.45	117.7-121.8	250 ^[32]	

1.4. *Matrices*

Common matrix materials used with reinforced fibrous composites are normally based upon polymers, polymer mixtures, or mixtures of chemically reactive components [42]. Metal and ceramic matrices are also used for certain fibers, particularly where high temperatures are expected [32].

One type of matrix called a thermoset matrix involves a two part system that is mixed to “harden” is popular due to low cost and ease of processing. These type of matrices are formed by irreversible chemical reactions between a “resin” and “hardener” that produce amorphous cross-linked polymers. The low viscosity of the resin system (as it is commonly called before mixing) aids with fiber impregnation for good bonding at high processing speeds [37].

Whichever matrix type is used, it directly affects the design, production, cost, strength, and nearly every other aspect of the finished composite. A variety of resins are commonly used for glass, carbon, and aramid fibers in aerospace, automotive, marine, and other industries. Each has its advantages and disadvantages, and a brief description of the three most widely utilized follows.

1.4.1. Polyester Resin Matrix

Polyester resin, which has been in use for over 50 years, is a low cost, quick-setting thermoset matrix used most often with glass fibers. It has relatively poor adhesion and

poor compatibility with most other fibers. However, low cost makes it an economical choice for many applications. This type of polyester is very different than the polyester used in paints or thermoplastics, but does share some of the same functional groups (specific groups of molecules), mostly ester [32].

Curing of this resin begins with a free radical that initiates chain growth of double bond monomers, which means very small amounts of the active initiator are required. The speed of cure can be adjusted by the amount of initiator or by the use of accelerators. However, the cure stage is highly exothermic, and there is potential for thermal damage, especially in thick sections [32]. Oxygen impurities can kill the free radicals used to cure polyester resins, and incomplete cure is a potential at free surfaces, unless precautions are taken.

Care should be exercised when curing polyester resins since the free radical initiators are almost always hazardous chemicals. Methyl ethyl ketone peroxide (MEKP) is a common initiator for room temperature cures. MEKP can cause permanent skin and eye damage and can be explosive if used incorrectly. Metal salts can also be used as accelerators, but can spontaneously explode if not mixed properly into the resin.

Some polyester resins can withstand outdoor exposure with just slight discoloration and strength loss for up to 30 years, due to good UV resistance. The upper range of service temperature for polyester resins is for the chlorendic resin type, where applications up to 176 °C are acceptable [35]. Flame and chemical resistant forms of polyester are also available [37]. A general disadvantage of this low cost matrix material is moderate

shrinkage during cure which can reduce the adhesion to fibers. As a low cost matrix material, however, the disadvantages are usually acceptable.

1.4.2. Epoxy Resin Matrix

Epoxy resins are known for their high strength, modulus, toughness, and chemical resistance. This thermoset matrix is generally easy to process, has excellent adhesion, low shrinkage, and is compatible with a number of fibers [37]. Epoxies are curable by reaction with a number of amines, acids, and alcohols, and are available in a wide range of viscosities, from liquid to nearly solid.

Several different compounds of epoxy are available, but the class of compounds known as epoxy resins contain two or more epoxide groups per molecule. An epoxide is a three atom ring containing two carbons and one oxygen. The bonds are highly stressed due to the unfavorable bond angle, which encourages reaction with a variety of curing agents (often called hardeners) [32].

An epoxy resin cure is a series of individual chemical reactions that occur at different rates. The stoichiometry, or ratio, of resin to hardener is important for these reactions to follow the correct sequence, form the proper molecular architecture, and hence correct chemical and mechanical properties. Another important feature is that epoxy passes through a number of physical states as it cures [32]. The viscosity reaches a minimum (which is helpful for processing and impregnating fibers) then rapidly increases (at a point called gelation) as molecular chains begin to cross-link. The amount of time epoxy will spend in these states can be altered by the type of hardener used in the system (another useful feature depending on the desired use).

Depending on composition, epoxy has an upper service temperature limit of approximately 175 °C. The toughened versions are capable of slightly lower service temperatures of 125 °C, as there is a tradeoff between service temperature and toughness [35]. Issues with epoxy include higher cost, brittleness, and degradation of properties in the presence of moisture [42].

1.4.3. Vinyl Ester Resin Matrix

Vinyl ester resins are thermosets that fill a gap between cost and performance tradeoffs seen with polyester and epoxy resins. There are a great variety of vinyl ester resins, and they are generally resistant to acids, solvents, peroxides, and more [37]. Vinyl esters also have service temperature capacity up to 121 °C, better performance than the majority of low-cost polyester matrices, but not quite as good as that of epoxy resins [37].

The vinyl-ester resins usually have ingredients that are similar to the epoxies. They tend to form linear, saturated polymer chains with less cross-linking than the epoxy resins. The saturation of the cured resin contributes to the chemical resistance characteristics of vinyl-ester. The curing process is similar to the polyester resins, involving a low-cost free radical initiator [32].

1.4.4. Matrix Comparison

Examples of the three most common polymer based matrices are outlined below, Table 1.3. The values given are general guidelines, and include multiple types of polyester resins and epoxy resins to illustrate the range in values for these classes of thermoset matrices.

Table 1.3. Mechanical properties of some thermoset matrices [37, 46].

Thermoset	Tensile Strength, (MPa)	Tensile Modulus, (GPa)	Compressive Strength, (MPa)	Tensile Failure Strain, (%)	Specific Gravity
Polyester					
Orthophthalic	55.2	3.4		2.1	
Isophthalic	75.9	3.4	117.2	3.3	
Vinyl Ester					
Derakane 411-45	82.7	3.4	117.1	5-6	
Epoxy					
9310/9360	75.8	3.12		4	1.2
West System 105/205	54.1	2.8	78.6	3.4	1.18

1.5. Fibrous Composites and Theory

An important feature of fibrous composites stems from the fact that a given material is only as strong as its weakest defect. Fibrous composites work by physically separating fibers into a large number of members such that failure of a “weak” fiber cannot cause failure of the “strong” fibers that surround it. Rope and steel cable are good examples of this, where overall strength is enhanced due to the decreased sensitivity to a single defect as compared to a single piece of material of the same shape. This has been shown mathematically by many [32, 47]. As the total number of fibers increases, the ratio of unbroken to broken fibers increases, and strength becomes more reproducible towards a consistent value [32].

In a non-woven unidirectional composite, fibers cannot effectively transfer load to one another without some means of doing so. This is generally done with the matrix; a material which protects the surface of the fibers from damage, holds them in a desired shape or configuration, and transfers load to them. The matrix can also allow broken fibers to carry load along nearly their entire length, by transmission of load through shear stress at the fiber-matrix interface [47].

Two points of view are commonly used to study fibrous composites, micromechanical and macromechanical. The former analysis is aimed at providing an understanding of composites in terms of the fiber and matrix properties, their interaction, and geometry. The latter approach predicts average strength, stiffness, and other properties based on the average properties measured during a test of a unidirectional composite material [32].

A difficult aspect of composite modeling is the fiber-matrix interface, known as the interphase. The interphase can have a large effect on composite strength and toughness. Coatings or materials that remain adhered after manufacturing can also change the behavior of the bond at the interphase. Glass fibers, for example, can be coated with a sizing agent to help improve the bond strength, improve durability, and reduce handling damage [32].

Since a composite is made of two distinct materials, fiber and matrix, properties are influenced by the relative amounts of each. These volume fractions (or volume ratios), defined as V_f and V_m , represent the fiber volume fraction and the matrix volume fraction. They are defined as:

$$V_f = \frac{\text{volume of fiber}}{\text{volume of composite}} \quad 1.1$$

$$V_m = \frac{\text{volume of matrix}}{\text{volume of composite}} \quad 1.2$$

The total volume adds to unity [37]:

$$V_f + V_m = 1 \quad 1.3$$

A unidirectional fibrous composite (with all fibers running in one direction) is expected to be anisotropic, with properties that vary based on constituent volume fraction, properties, geometry and the interphase. Some fiber and matrix properties of interest are defined in Table 1.4.

Table 1.4. Fiber and matrix property definitions.

E_f	Young's modulus for fibers
ν_f	Poisson's ratio for fibers
G_f	Shear modulus for fibers
ρ_f	Density of fibers
E_m	Young's modulus for matrix
ν_m	Poisson's ratio for matrix
G_m	Shear modulus for matrix
ρ_m	Density of matrix

The unidirectional composite, an orthotropic material, has two directions which are most important, Figure 1.24. A material that is orthotropic has three planes of symmetry, one is parallel to the fibers, and two others that can have any orientation perpendicular to the fibers. It can be shown (see [32]) using the above fiber and matrix properties, that four

elastic constants define the in plane elastic behavior of a unidirectional composite. They are defined in Table 1.5.

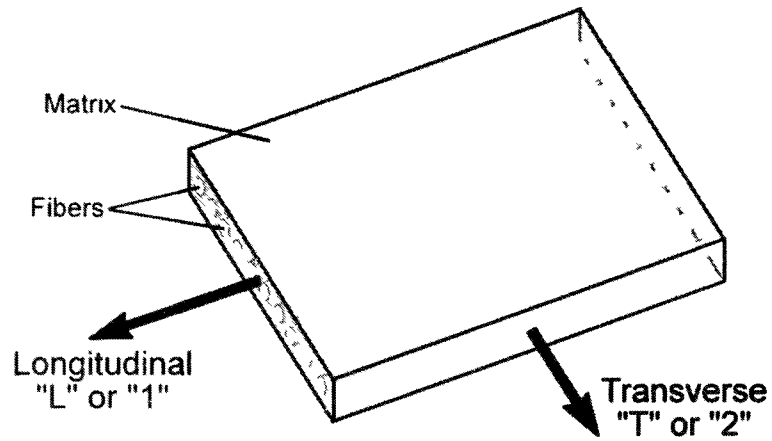


Figure 1.24. Direction definitions for a unidirectional composite.

Table 1.5. Elastic constants of unidirectional composites

$E_1 = E_L$	Longitudinal Stiffness
$E_2 = E_T$	Transverse Stiffness
$\nu_{12} = \nu_{LT}$	major Poisson's ratio
$G_{12} = G_{LT}$	in-plane shear modulus

Simple rule of mixture type of expressions arrive at the following [32]:

$$E_L = E_f \cdot V_f + E_m \cdot V_m \quad 1.4$$

$$E_T = \frac{1}{V_f/E_f + V_m/E_m} \quad 1.5$$

$$v_{LT} = v_f V_f + v_m V_m \quad 1.6$$

$$G_{LT} = \frac{1}{V_f/G_f + V_m/G_m} \quad 1.7$$

$$\rho = V_f \cdot \rho_f + V_m \cdot \rho_m \quad 1.8$$

Depending on properties of the fibers, matrix, and expected loading conditions, a fiber volume fraction can be found which often yields a good balance of mechanical properties. In practice, this fraction is between 40% and 60% depending on the type of fibers and matrix [37].

1.6. Energy Absorption

One type of mechanical energy absorption involves deceleration of a moving object through the use of a force applied through a distance (work). This often involves the compression of a porous structure or material. Car bumpers, helmets, and consumer packaging are all examples of mechanical energy absorbers. Common energy absorbing materials include closed-cell polystyrene and metallic foams, and the importance of these

materials to the packaging industry is well known. An ideal energy absorber should have a constant “plateau” stress when compressed, which translates into a constant force impacting the object, Figure 1.25. When the material cannot be compressed any further, there is a sharp rise in stress. This portion of the stress-strain curve is referred to as the densification region.

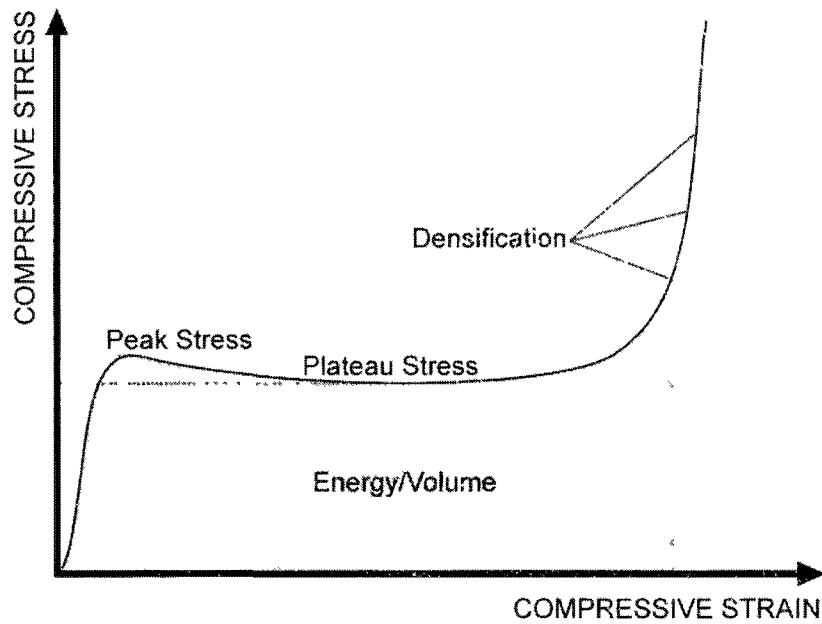


Figure 1.25. Stress-strain curve for an ideal energy absorber.

The amount of absorbed mechanical energy is a function of the work done on the absorber by external stimuli. As a moving object with some kinetic energy comes into contact with an energy absorbing material, the compressive stress of the material increases to some plateau stress. This compressive stress, σ , translates to a force F , depending on the contact area A . It follows the relation $F = \sigma \cdot A$. It is important that the object has stopped (all of its kinetic energy absorbed) before the densification strain is reached, or the stress (and therefore the deceleration force) will increase greatly, possibly

damaging the object. Good energy absorbers dissipate all of the energy at levels below the damage threshold, and they must be thick enough to do so.

By definition, mechanical work W is equal to the product of a force F and the parallel component of the distance D . This is the well-known relation $W = \vec{F} \cdot \vec{D} = F \cdot d \cdot \cos(\theta)$ [48]. Applying this to an energy absorber, the work W is equal to the product of the force F and the distance crushed D (less energy loss or dissipation). Force F is nearly equal to the product of the plateau stress σ_{pl} and the contact area A . The distance d is found from the strain ε and initial absorber height h_0 .

$$W = F \cdot d \cos 90^\circ \text{ where } F = \sigma_{pl} \cdot A \text{ and } d = \varepsilon \cdot h_0$$

Combining these relations, work is:

$$W = \sigma_{pl} \cdot A \cdot \varepsilon \cdot h_0 = \sigma_{pl} \cdot \varepsilon \cdot (A \cdot h_0) \quad 1.9$$

In crushing materials, where the concepts of stress and strain are commonly used, work per unit volume (W/V) and work per unit mass (W/m) are useful notations [15]. Volume is simply $V = A \cdot h_0$, and the work per unit volume is found:

$$\frac{W}{V} = \sigma_{pl} \cdot \varepsilon \quad 1.10$$

Lastly, dividing the work per unit volume by density ρ , where $\rho = m/V$, work per unit mass m is found to be:

$$\frac{W}{m} = \frac{(\sigma_{pl} \cdot \epsilon)}{\rho} \quad 1.11$$

When a material is loaded and deforms, the work per unit volume is the area under the stress-strain curve. This is found by integration of $\sigma \cdot d\epsilon$, or more commonly, by directly measuring the area under the curve. This measurement can be used for comparison and selection of different materials, depending on use.

An important aspect of energy absorption is the peak stress that a protected object can withstand. In Table 1.6, maximum decelerations, in g's, that several objects can withstand without damage are listed. Based on the mass of the object, an appropriate maximum force can be calculated. In many scenarios, the total mass and initial kinetic energy of both colliding objects must be taken into consideration, along with dissipation and other factors.

Table 1.6. Maximum allowable deceleration examples [1].

Object	Maximum Deceleration (g)
Human body, sustained	5-8
Delicate instrument, gyroscopes	15-25
Optical and X-ray equipment	25-40
Computer displays, hard disks	40-60
Human head, 36 ms contact time	55-60
Stereos, TV receivers	60-85
Household appliances, furniture	85-115
Machine tools, engines	115-150

To safely stop a moving object listed in the table above without damage, the deceleration must remain below the values listed. For example, consider a falling computer hard drive, with mass $m = 3.7$ kg. In order to prevent damage, the deceleration a must be less than 60 g's, or $a \leq 60 \cdot 9.8 \text{ m/s}^2 = 588 \text{ m/s}^2$. From Newton's Second Law, the maximum force F_m is related to the object mass m and the acceleration (or deceleration), a , such that $F_m = m \cdot a = 3.7 \text{ kg} \cdot 588 \text{ m/s}^2$, or $F_m \leq 2175 \text{ N}$.

Using an energy absorbing material with an estimated contact area between the object and the energy absorber of 0.01 m^2 , a maximum stress can be found for this example, $\sigma_m = F_m / A = (2175 \text{ N}) / 0.01 \text{ m}^2 = 0.217 \text{ MPa}$. This maximum stress, σ_m , is useful for selecting an energy absorber which will not damage the object. This value should be greater than the plateau stress, σ_{pl} , of the material chosen, as well as the peak stress, σ_p , to minimize the likelihood of damage.

Additionally, it is important to know the amount of initial energy, E_0 , (kinetic energy in a crash, or potential energy for a fall), the object is expected to dissipate. With initial energy estimations, the geometry (thickness) of the energy absorber can be found. In this case, the total thickness of the energy absorber is h_0 , contact area is A , and the densification strain of the selected material is ε_D , such that the displacement before densification is $d = h_0 \cdot \varepsilon_D$. The thickness is then found to be:

$$W = F \cdot d \text{ or } E_0 = (\sigma_m \cdot A) \cdot (\varepsilon_D \cdot h_0) \quad 1.12$$

$$h_0 = \frac{E_0}{\sigma_m \cdot A \cdot \varepsilon_D} \quad 1.13$$

In some instances, the geometry (thickness) of the energy absorber may be a limiting factor. If this is the case, one can find the maximum initial energy (i.e., kinetic energy and impact velocity or potential energy and drop height) which the energy absorber can dissipate before the object will be damaged. The maximum energy which can be usefully absorbed, W_{max} , is equal to the product of the plateau stress of the material σ_{pl} , the contact area A , and the displacement before densification, $d = h_0 \cdot \varepsilon_D$.

$$W_{max} = \sigma_{pl} \cdot A \cdot h_0 \cdot \varepsilon_D \quad 1.14$$

The relationship for kinetic energy is $E = (1/2) \cdot m \cdot v_0^2$, where v_0 is the initial velocity.

When this kinetic energy is equal to the maximum energy which can be absorbed,

$$\frac{1}{2} m \cdot v_0^2 = \sigma_{pl} \cdot A \cdot h_0 \cdot \varepsilon_D \quad 1.15$$

Maximum impact velocity can then be solved:

$$v_0 = \sqrt{\frac{2 \cdot \sigma_{pl} \cdot A \cdot h_0 \cdot \varepsilon_D}{m}} \quad 1.16$$

For potential energy, $E = m \cdot g \cdot H$, where g is gravitational acceleration and H is the initial drop height. When potential energy equals energy absorbed,

$$m \cdot g \cdot H = \sigma_{pl} \cdot A \cdot h_0 \cdot \varepsilon_D \quad 1.17$$

From this, maximum drop height without exceeding limit deceleration can be found:

$$H = \frac{\sigma_{pl} \cdot A \cdot h_0 \cdot \varepsilon_D}{m \cdot g} \quad 1.18$$

In real life design scenarios, availability of commercially produced foams or other energy absorbers (and their cost) will play a role in the choice of material. Additionally, more detailed methods using higher order approximations or iterative processes can be used to reach a final design for the energy absorber. These methods have been studied in detail by others to account for the efficiencies of energy absorbers, strain-rate dependencies, and more [1, 49].

1.7. Penetration and Ballistic Impact Tolerance

A wide variety of materials have been used for these types of applications, ranging from leather or metal to advanced composites. Creating armor to protect against potential threats is a challenge for designers, but well performing materials certainly help. Impact is a complex problem, and generally any one single property of a material is not a good predictor; it is often some other combination of properties such as tensile modulus, elongation, tenacity, energy absorption, and speed of sound in the material that are important [50]. Aramid fibers, with high specific strength to weight ratio, good elongation to failure, and high toughness, were first used as wearable armor during the early 1970s. These materials have saved hundreds, if not thousands, of lives (both civil and governmental personnel).

Modern ballistic protection generally takes one of two forms; the first is called soft armor, with multiple layers of woven fabric and no matrix material. The second is a composite laminate made with some amount of resin matrix (typically 20-25% for non-structural armor applications) [50]. Soft armors perform well at stopping soft lead projectiles common to handguns (Figure 1.26), which “mushroom” upon impact.

Laminates, on the other hand, perform well when stopping hard, blunt fragments (e.g., those projected from an exploding warhead). Woven fabrics are preferred, since the bidirectional reinforcement in each single layer enhances the impact resistance [52].

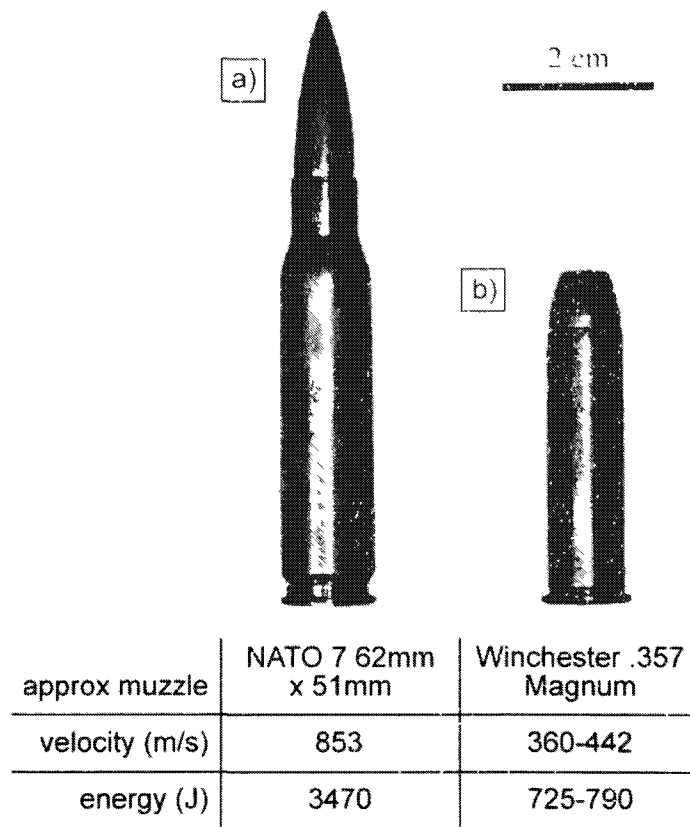


Figure 1.26. Example ammunition: a) armor piercing and b) handgun [51].

Neither construction has proven effective at stopping armor piercing bullets fired from a rifle. These generally have higher energy and velocity than handgun bullets, and a sharp point which easily spreads the energy absorbing fibers apart [50]. The danger that sharp armor piercing rounds pose to wearers of fibrous composite armor is also present with penetrating objects such as knives/ice picks and teeth. Inventors have been able to increase the performance of ballistic armor in this regard by using tightly woven metal

wires or ceramic inserts, which can help stop sharp object attacks in addition to providing knife and ballistic protection [53].

2. CORRUGATED KEVLAR STRUCTURE

A number of energy absorbing materials are available that can be used as multipurpose materials for numerous applications. Most energy absorbers discussed in the previous chapter do not provide good penetration resistance in addition to good mechanical energy absorption. In this work, a combination of these traits is sought by using a multi-layer, corrugated aramid-epoxy design, Figure 2.1.

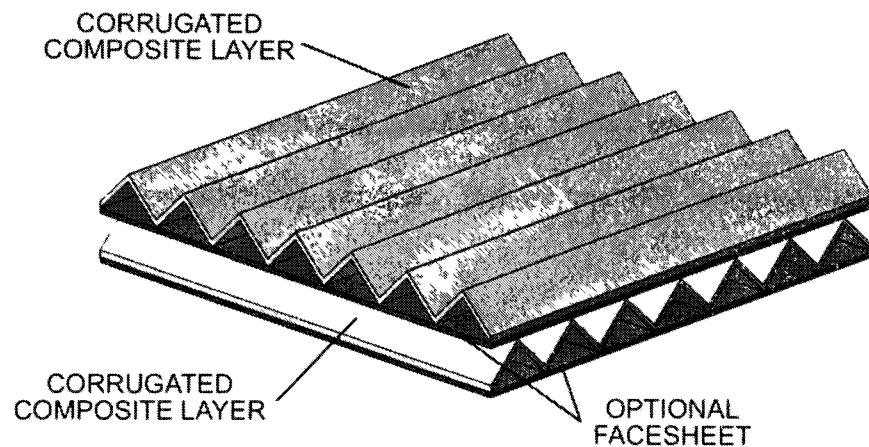


Figure 2.1. Proposed corrugated Kevlar structure.

Corrugated materials (e.g., cardboard) discussed in Chapter 1 have been widely used for decades as energy absorbers in the packaging industry, and were also proposed as blast protection materials in naval applications [16, 18]. However, a literature review found that little work has been done on this type of structure with composites, especially as a penetration resistant energy absorber.

With this structure, benefits of woven aramid-epoxy as a penetration resistant material can still be employed, since a penetrating object must pass through a number of layers. Unlike honeycombs, the open spaces are not oriented parallel to the direction of potential impact. This not only reduces the risk of a ballistic object passing between or through a cell, but maintains interconnected areas between cells for gas and fluid storage.

When impacted, triangular corrugation produces a number of wide plates in compression (another area where a unique feature of aramid fibers can be exploited). Unlike other composites (e.g., carbon, boron, and fiberglass), aramid fibers retain some strength through compressive failure in a similar fashion to ductile metals [41, 43, 54, 55].

As a cellular material, properties such as relative density, densification strain, and plateau stress are all important. Developing predictions of the proposed structure requires examination of the base materials, geometry, and the expected loading (plates loaded in compression).

3. MECHANICAL BEHAVIOR PREDICTION

The focus of this work lies in the development of an efficient cellular material (competitive with foams and prismatic materials) that absorbs energy and resists blunt object penetration. Corrugated materials like those under investigation for this study can be represented as thin plate members. This has been done by others studying the buckling of corrugated webs [56]. Enhancing the performance of these materials may benefit through an understanding of classical plate theory and the behavior of laminated composites. Buckling (or elastic instability) of the composite aramid-epoxy plates is anticipated to be the main failure mode and receives careful consideration.

3.1. *Composites*

Polymer matrix composites (PMC) have been studied for strength and stiffness by a number of sources [32, 35, 37, 57]. However, it is important to bear in mind that while stiffness estimates are generally accurate, strength predictions are not, making experimental data very valuable [37]. Concepts for predicting the stiffness of laminated, anisotropic plates are presented below.

3.1.1. Laminated Plate Theory

A plate or shell with multiple composite layers can have a large number of possible configurations due to many possible fabric orientations. Since the stiffness of fibrous materials depends on the direction of the fibers (the material is not isotropic), laminated

plate theory can be used to estimate overall stiffness properties. A few important assumptions in classical laminate theory are [32]:

- For 2-D plane stress analysis, strain is constant through the thickness
- For bending, strain varies linearly through thickness
- The laminate is thin compared to in-plane dimensions
- Each layer is quasi-homogeneous and orthotropic
- Displacements are small compared to thickness
- Behavior remains linear

Coordinate systems play an important role in laminated plate theory, as fibers in a layer have their own three-axis system (denoted by axes 1, 2, and 3). In this system, the fibers run in the direction of the 1-axis, while the 2-axis is perpendicular to it and on the surface of the composite. The 3-axis is perpendicular to these in-plane axes, Figure 3.1 [37].

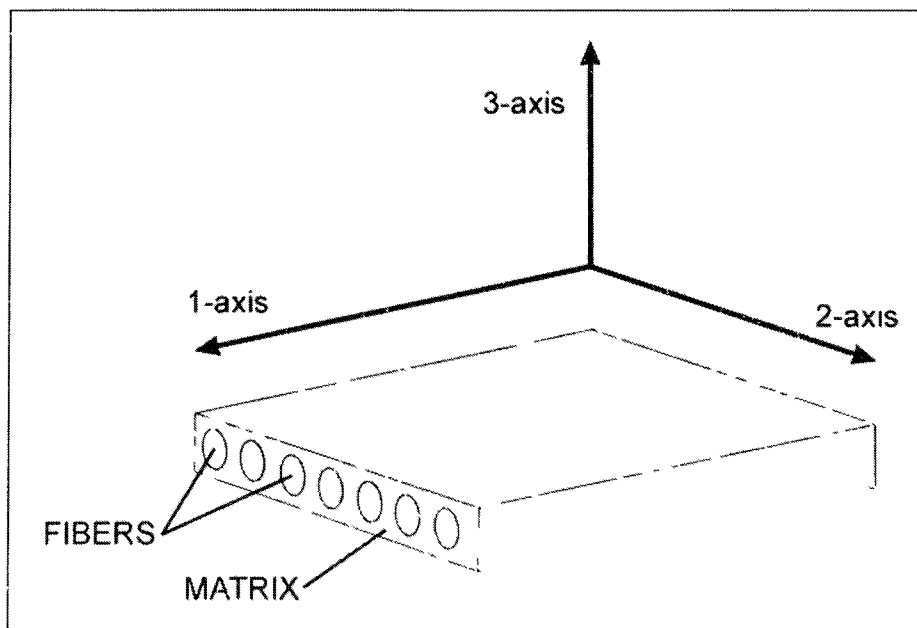


Figure 3.1. Axis system for laminated plates.

Common to all layers is the global coordinate system, with axes denoted by x , y , and z (also called the laminate axis system). The orientation of this system is chosen arbitrarily by the designer, so it may be aligned with the part being designed, the major loads applied, etc [37]. Each layer in a composite is rotated some angle θ , from the global system, measured about the z -axis of a layer (where θ is measured from the global x -axis to the layer 1-axis), Figure 3.2.

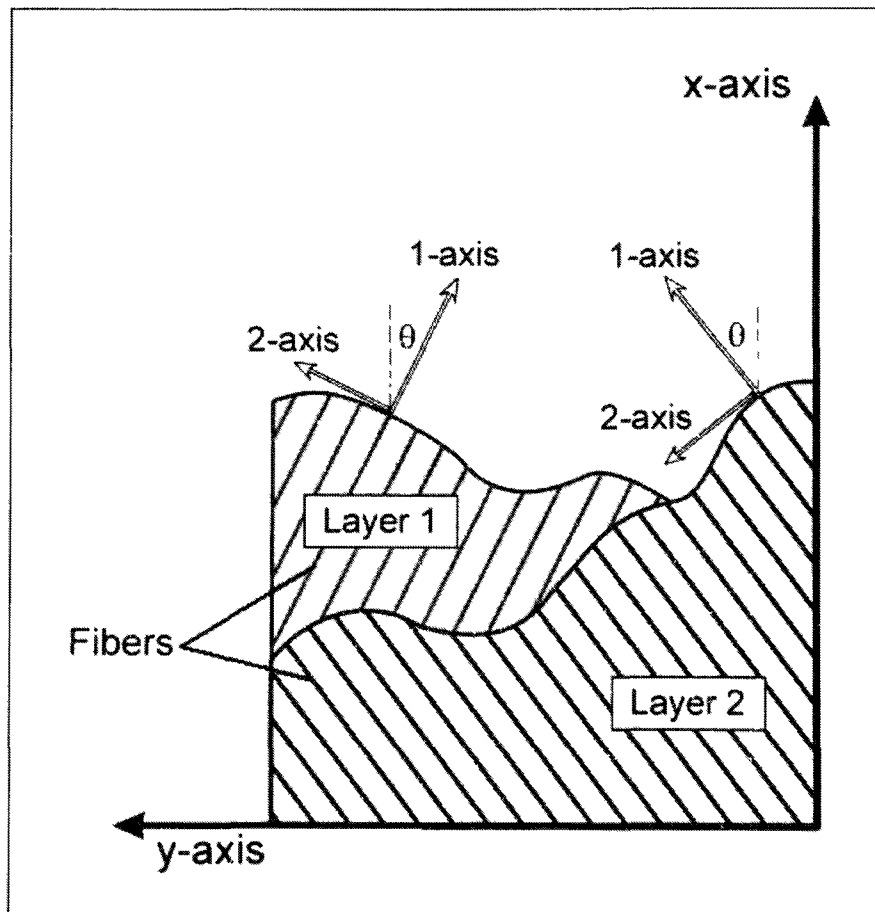


Figure 3.2. Example of laminate coordinate systems.

In a single layer of thin composite plate (which is assumed orthotropic), we normally consider only in-plane stresses. Therefore, only three stresses and three relating strains are of interest. These stresses, σ_1 , σ_2 , and τ_{12} , are the longitudinal, traverse, and shear

stress, respectively, Figure 3.3. Three corresponding strains, ϵ_1 , ϵ_2 and γ_{12} , relate to the longitudinal strain, traverse strain, and shear strain respectively. Other stresses which are assumed to be negligible are the out-of-plane stress σ_3 , and the interlaminar shear τ_{13} and τ_{23} .

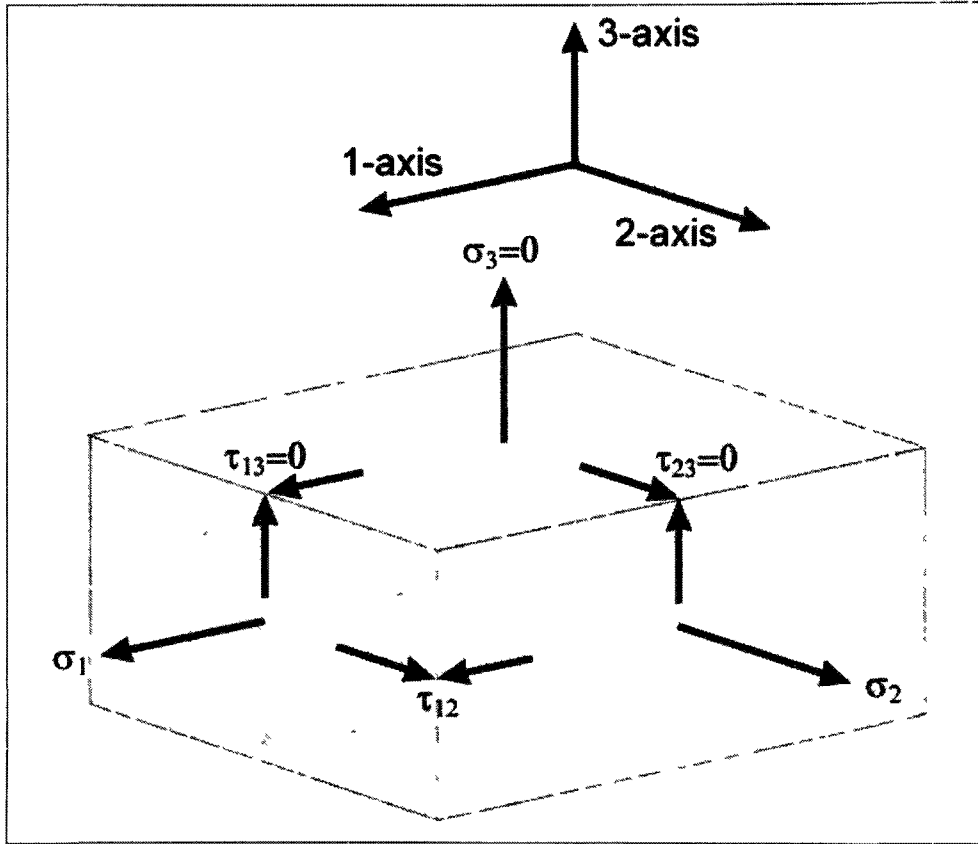


Figure 3.3. Stresses on unit of laminae

For the nonzero stresses as defined above, the stress strain relationship for the thin plate can be seen below with the reduced stiffness coefficient Q_{ij} [32].

$$\begin{bmatrix} \sigma_1 \\ \sigma_2 \\ \tau_{12} \end{bmatrix} = \begin{bmatrix} Q_{11} & Q_{12} & 0 \\ Q_{21} & Q_{22} & 0 \\ 0 & 0 & Q_{66} \end{bmatrix} \begin{bmatrix} \epsilon_1 \\ \epsilon_2 \\ \gamma_{12} \end{bmatrix} \quad 3.1$$

Values of the reduced stiffness matrix come from the material properties for a unidirectional composite. These values (defined in section 1.5) are the longitudinal stiffness E_L , transverse stiffness E_T , major Poisson's ratio ν_{LT} , and in-plane shear modulus G_{LT} . The resulting reduced stiffness coefficients are given by the four equations below. Different authors [32, 37, 58] have slightly different methods and notation for this step, although the result is the same.

$$Q_{11} = \frac{E_L}{1 - \nu_{LT}^2 (E_T/E_L)} \quad 3.2$$

$$Q_{22} = \frac{E_T}{1 - \nu_{LT}^2 (E_T/E_L)} \quad 3.3$$

$$Q_{12} = Q_{21} = \frac{\nu_{LT} E_L}{1 - \nu_{LT}^2 (E_T/E_L)} \quad 3.4$$

$$Q_{66} = G_{LT} \quad 3.5$$

As noted previously, unidirectional fibers are rotated some angle θ . The constitutive relation seen above, Equation 3.1, can be transformed to the laminate axes system with the transformed reduced stiffness matrix Q' :

$$\begin{bmatrix} \sigma_x \\ \sigma_y \\ \tau_{xy} \end{bmatrix} = \begin{bmatrix} Q'_{xx} & Q'_{xy} & Q'_{xs} \\ Q'_{xy} & Q'_{yy} & Q'_{ys} \\ Q'_{xs} & Q'_{ys} & Q'_{ss} \end{bmatrix} \begin{bmatrix} \epsilon_x \\ \epsilon_y \\ \gamma_{xy} \end{bmatrix} \quad 3.6$$

The transformed reduced stiffness matrix Q' is found, with $c = \cos \theta$ and $s = \sin \theta$ for a given angle [32]:

$$\begin{bmatrix} Q'_{xx} \\ Q'_{xy} \\ Q'_{yy} \\ Q'_{xs} \\ Q'_{ys} \\ Q'_{ss} \end{bmatrix} = \begin{bmatrix} c^4 & 2c^2s^2 & s^4 & 4c^2s^2 \\ c^2s^2 & c^4 + s^4 & c^2s^2 & -4c^2s^2 \\ s^4 & 2c^2s^2 & c^4 & 4c^2s^2 \\ c^3s & -cs(c^2 - s^2) & -cs^3 & -2cs(c^2 - s^2) \\ cs^3 & cs(c^2 - s^2) & -c^3s & 2cs(c^2 - s^2) \\ c^2s^2 & -2c^2s^2 & c^2s^2 & (c^2 - s^2)^2 \end{bmatrix} \begin{bmatrix} Q_{11} \\ Q_{12} \\ Q_{22} \\ Q_{66} \end{bmatrix} \quad 3.7$$

For a general ply, as shown schematically in Figure 3.4 below, a different transformed reduced stiffness matrix must be calculated for each layer with a different orientation or base material. If a laminate has a large number of plies, this can quickly become a task best suited for a computer program, as can be seen with the MATLAB script shown in Appendix B.

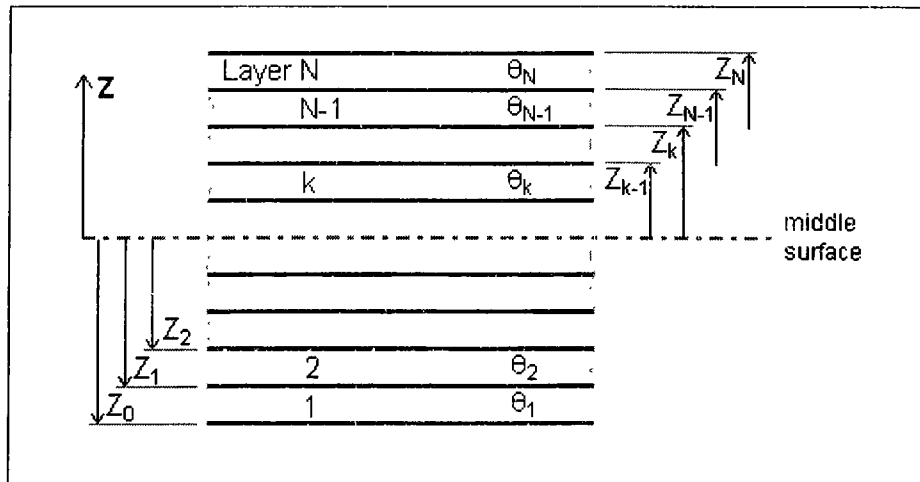


Figure 3.4. Example laminate with ten layers ($N=10$).

Classical plate theory relates forces and moments to in-plane midplane strain ϵ_0 and curvature κ :

$$\begin{Bmatrix} \{N\} \\ \{M\} \end{Bmatrix} = \begin{bmatrix} [A] & [B] \\ [B] & [D] \end{bmatrix} \begin{Bmatrix} \{\epsilon_0\} \\ \{\kappa\} \end{Bmatrix} \quad 3.8$$

where $\{N\}$ is a 3-unit vector corresponding to tensile and shear force per unit length (N_x , N_y and N_{xy}), and $\{M\}$ is a vector for moments per unit length (M_x , M_y and M_{xy}). The three symmetric 3 x 3 matrices $[A]$, $[B]$ and $[D]$ are the inplane stiffness matrix, the bending-extension coupling matrix, and the bending stiffness matrix, respectively [37]. Subscripts for these three matrices are the same, and equal to those used for Q' . The formulas for these three stiffness matrices are:

$$A_y = \sum_{k=1}^N (Q'_y)_k (z_k - z_{k-1}) \quad \text{or} \quad [A] = \sum_{k=1}^N ([Q']_k) (z_k - z_{k-1}) \quad 3.9$$

$$B_y = \frac{1}{2} \sum_{k=1}^N (Q'_y)_k (z_k^2 - z_{k-1}^2) \quad \text{or} \quad [B] = \frac{1}{2} \sum_{k=1}^N ([Q']_k) (z_k^2 - z_{k-1}^2) \quad 3.10$$

$$D_y = \frac{1}{3} \sum_{k=1}^N (Q'_y)_k (z_k^3 - z_{k-1}^3) \quad \text{or} \quad [D] = \frac{1}{3} \sum_{k=1}^N ([Q']_k) (z_k^3 - z_{k-1}^3) \quad 3.11$$

The bending-extension coupling matrix $[B]$ can be shown to be zero for the case of a symmetric laminate. A symmetric laminate is one where a ply below the mid-plane with coordinates $z_{k-1} = -a$ and $z_k = -b$ has a mate above the midplane (at the same distance) with $z_{k-1} = b$ and $z_k = a$ with the same fiber orientation, Figure 3.5 [32].

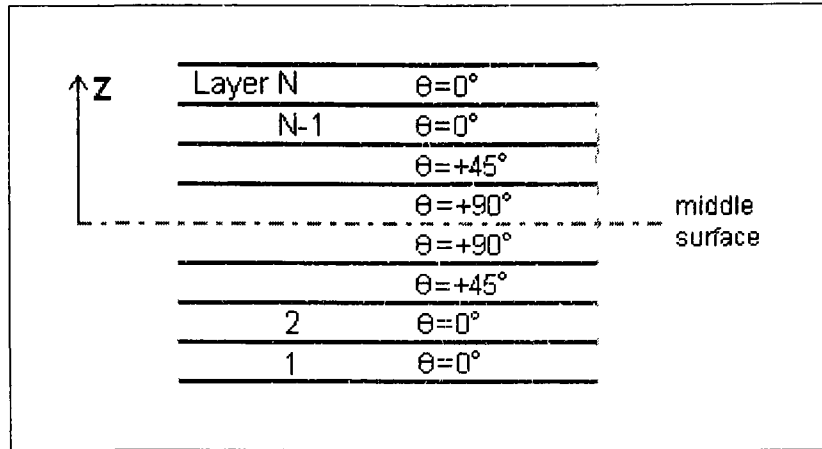


Figure 3.5. Example of a symmetrical laminate.

3.1.2. Woven Fiber Theory

Up to this point, discussion has been focused on unidirectional fibrous composites. However, the unique combination of light weight, flexibility, strength and toughness inherent to textile materials has long made them an attractive reinforcement for composites. Bidirectional weaves are available in a number weave patterns; plain, crow, twill, satin, etc. Triaxially woven fibers feature enhanced shear rigidity and isotropy [52]. However, weaving the yarns reduces the ability for the reinforcing fibers to maintain strength in compression since the fibers are not straight [32].

In orthogonal-woven (bidirectional) fabrics, the length direction is known as the warp, and the width direction is known as the fill (or sometimes weft). Parameters used to identify the geometry of the weave are n_{gf} and n_{gw} , which represent the number of yarns until repeat in the fill and warp directions, respectively [59]. Figure 3.6 shows some popular weaves with $n_{gf} = n_{gw}$. In this case, n_g is used to represent the number of yarns until the pattern is repeated in both the fill and warp directions.

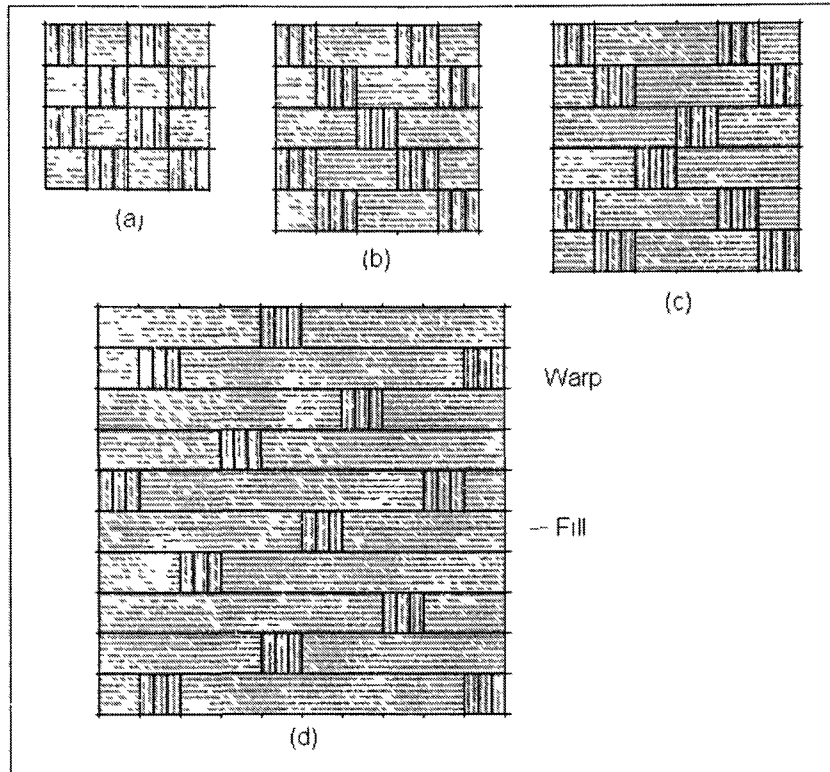


Figure 3.6. Examples of fabric weaves: (a) plain ($n_g = 2$); (b) twill weave ($n_g = 3$); (c) 4-harness satin ($n_g = 4$); and (d) 8-harness satin ($n_g = 8$).

Analytical models exist for determination of in-plane stiffness of woven fabric laminated plates. Each has certain limitations and applicability depending on the type of weave [60]. Simplifications are used to treat the fiber as an idealized assembly of infinitesimal pieces of laminate [59]. With the mosaic model, undulation (crimp) in actual fibers is omitted, providing convenient estimations of upper and lower bounds for elastic constants. Accounting for the weaving angle results in the fiber crimp model, which is best suited to models with low n_g values. For fabrics with no closely connected weaves and higher n_g , such as the satin weaves, the bridging model is well suited [59]. An element of a plain weave is shown below with its basic geometry, Figure 3.7.

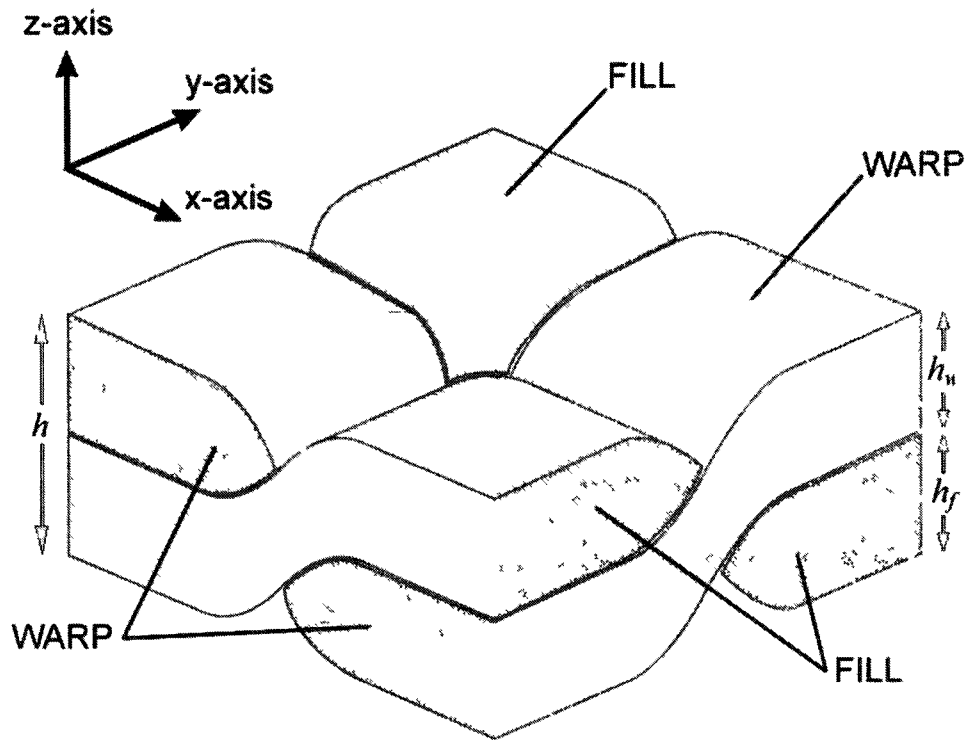


Figure 3.7. Fill and warp yarns in a plain-weave element.

Accurate analysis of in-plane stiffness properties using common woven fiber models necessitates careful measurement of the weave geometry [59]. Important parameters include the yarn width for fill and warp (a_f and a_w), yarn height for fill and warp (h_f and h_w), gap between fill and warp yarns (g_f and g_w), and undulation of the fill and warp yarns (u_f and u_w), Figure 3.8

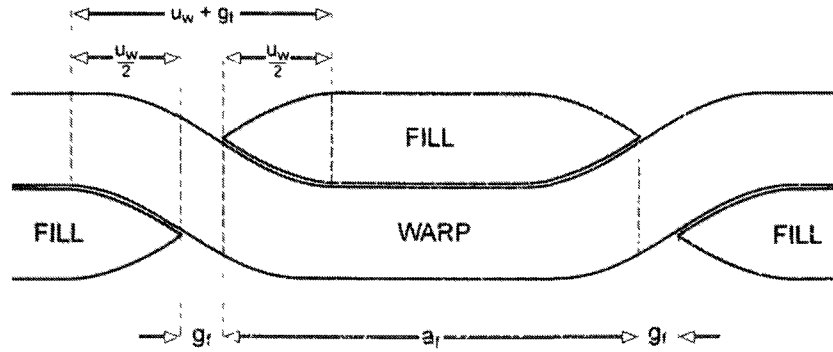


Figure 3.8. Section of woven fiber element.

When woven yarns are analyzed using the methods mentioned above, the results generally show a decrease in stiffness when compared to a unidirectional laminate of similar thickness and materials. For example, a cross-ply carbon-epoxy laminae constructed of unidirectional layers with a sequence of $[0/90/90/0]$ can be used to represent a woven fabric of similar construction. From the research of Naik [59], predicted in-plane stiffness for cross-ply unidirectional laminates and plain-weave fibers is shown, Table 3.1. These data were calculated based upon T300 carbon fibers and an epoxy matrix. Variations in the woven fiber geometry include the ratio of laminae thickness to yarn width (h/a) and ratio of undulation to yarn thickness (u/a).

Table 3.1. Unidirectional cross-ply and woven fabric comparison.

Overall Fiber Fraction, V_f	Undulation to Yarn Width Ratio, u/a	UD Lay-up E_x, E_y (GPa)	$h/a=0.1$ E_x, E_y (GPa)	$h/a=0.2$ E_x, E_y (GPa)	$h/a=0.4$ E_x, E_y (GPa)
0.25	0.1	33.2	29.8	29.3	29.0
0.35		45.2	40.4	39.6	39.3
0.50		63.5	56.6	52.3	51.9
0.25	0.6	33.2	29.8	25.5	21.6
0.35		45.2	40.3	34.3	29.0
0.50		63.5	57.5	49.2	41.6
0.25	1.0	33.2	30.8	25.9	18.4
0.35		45.2	42.2	35.5	25.1
0.50		63.5	61.6	53.9	40.3

A consistent trend in the above table indicates that fabrics with high undulation to yarn width (u/a) and a high yarn thickness to overall laminae thickness (h/a) exhibit significant degradation of in-plane stiffness. However, relatively flat fabrics (low h/a) increases the stiffness to values near those of the unidirectional plate. Thus, flatter, tighter weaves result in stiffer composites.

3.2. Plate Loading

Plate theory (or classical plate theory, CPT) for small deflections is well known for isotropic (e.g., metal) and anisotropic materials (e.g., fibrous composites). Here, out-of-plane deflection $w(x,y)$ is predicted based upon the plate stiffness D and the acting loads, Figure 3.9. Applied moments and in-plane shear loads are not shown in this diagram for clarity.

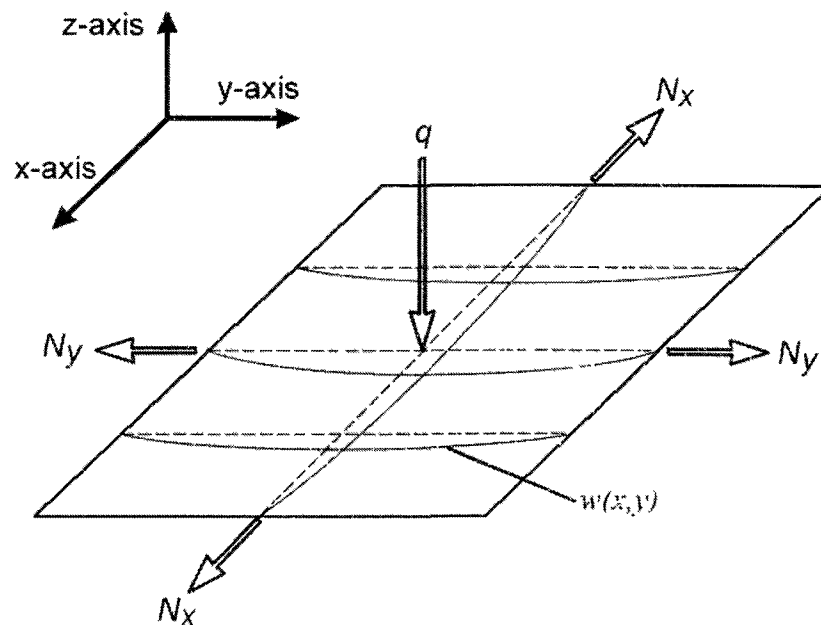


Figure 3.9. Definition of loads and resulting deflection for a rectangular plate.

The basic plate equation for buckling from isotropic theory is shown below, Equation 3.12 [61]. In the plate equation, plate stiffness D and the out of plane deflection $w(x,y)$ are related to the in-plane loads N_x , N_y , N_{xy} (which is a force per unit length), and out of plane pressure q using a differential equation.

$$D \left[\frac{\partial^4 w}{\partial x^4} + 2 \frac{\partial^4 w}{\partial x^2 \partial y^2} + \frac{\partial^4 w}{\partial y^4} \right] = q + N_x \frac{\partial^2 w}{\partial x^2} + N_y \frac{\partial^2 w}{\partial y^2} + 2N_{xy} \frac{\partial^2 w}{\partial x \partial y} \quad 3.12$$

The plate bending stiffness D for composite laminates is the matrix $[D]$ as calculated for the given ply orientations. For flat plates and small deflections, the stiffness matrix is symmetric with dimension 3 x 3. The buckling equation for a thin, laminated anisotropic plate equation with no lateral loading is shown below. The values D_1 , D_2 and D_3 represent elements of the bending stiffness matrix, where D_{xx} , D_{yy} and D_{xy} are direct strains and D_{ss} is the shear stiffness [62].

$$D_1 \frac{\partial^4 w}{\partial x^4} + 2D_3 \frac{\partial^4 w}{\partial x^2 \partial y^2} + D_2 \frac{\partial^4 w}{\partial y^4} = N_x \frac{\partial^2 w}{\partial x^2} + N_y \frac{\partial^2 w}{\partial y^2} + 2N_{xy} \frac{\partial^2 w}{\partial x \partial y} \quad 3.13$$

where:

$$\begin{aligned} D_1 &= D_{xx} \\ D_2 &= D_{yy} \\ D_3 &= D_{xy} + 2D_{ss} \end{aligned} \quad 3.14$$

The solution of the displacement $w(x,y)$ can be achieved by a number of methods, including equilibrium (static), energy, and kinetic or dynamic methods [58]. Elastic stability (or instability) is concerned with the lateral deflection w of a plate induced by in plane loads N_x , N_y , or N_{xy} , and will be discussed in more detail later.

3.3. Plate Geometry

Crushing of plates within a prismatic corrugated material can be approximated by a short wide plate in compression. Such a plate of width a and height b is shown schematically in Figure 3.10. F is the force per length acting over the width. There is significant point loading in the proposed structure at the crossover points where the layers contact one another. This point loading causes stress concentrations, which can lead to premature failures of the material [37]. The situation depicted in Figure 3.10 does not consider these stress concentrations.

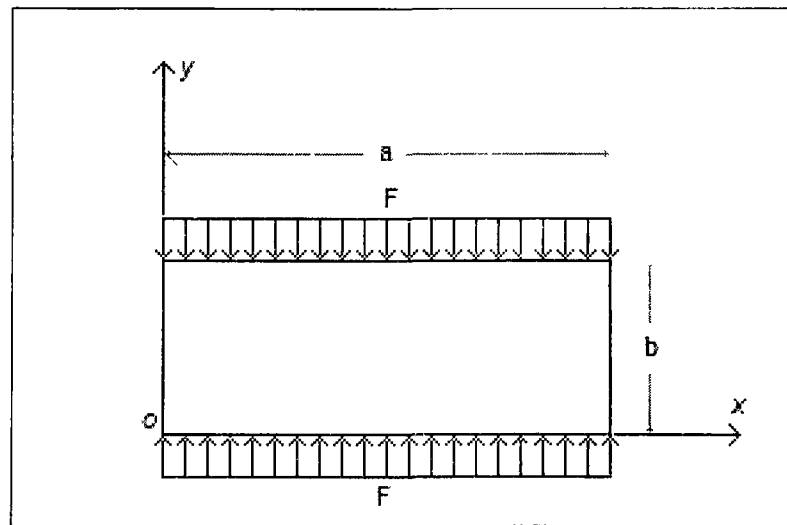


Figure 3.10. Ideal loading of a wide plate in uniform axial compression.

The boundary conditions will be considered as pinned or simply supported along the x -direction at $y=0$ and $y=b$. This type of boundary condition will allow no displacement but some rotation for the kinematic (geometric) variables. This is another simplification, as the structure is only supported at certain points. The force (static)

variables at $y = 0$ and $y = b$ are set to allow finite force, but no moment [61]. This is represented by satisfying the following four equations:

$$w(x,0) = 0 \quad 3.15$$

$$w(x,b) = 0 \quad 3.16$$

$$\left. \frac{\partial^2 w}{\partial y^2} \right|_{y=0} = 0 \quad 3.17$$

$$\left. \frac{\partial^2 w}{\partial y^2} \right|_{y=b} = 0 \quad 3.18$$

The edges along the y -direction at $x = 0$ and $x = a$ are free, such that the kinematic variables allows free displacement and rotation. A free boundary condition also requires that the static variables for moment and shear force are zero. This boundary condition is satisfied with the following four equations:

$$\left(\frac{\partial^2 w}{\partial x^2} + \nu \cdot \frac{\partial^2 w}{\partial y^2} \right) \Big|_{x=0} = 0 \quad 3.19$$

$$\left(\frac{\partial^2 w}{\partial x^2} + \nu \cdot \frac{\partial^2 w}{\partial y^2} \right) \Big|_{x=a} = 0 \quad 3.20$$

$$\left(\frac{\partial^3 w}{\partial x^3} + (2-\nu) \cdot \frac{\partial^3 w}{\partial x \partial y^2} \right) \Big|_{x=0} = 0 \quad 3.21$$

$$\left(\frac{\partial^3 w}{\partial x^3} + (2-\nu) \cdot \frac{\partial^3 w}{\partial x \partial y^2} \right) \Big|_{x=a} = 0 \quad 3.22$$

3.4. *Plate Instability*

When structures fail, they normally do so due to material failure, structural instability, or some combination of the two. Material failure is calculated, for the most part, from

known strength values. Structural instability (and stability analysis), on the other hand, presents a more formidable challenge since the buckling response of a complicated structure is often nonlinear and difficult to predict [63].

Consider a flat plate subjected to a small axial compressive load that is in a state of equilibrium. As this compressive load is increased, it is known that an out-of-plane deflection will occur after the load has reached a critical load N_{CR} [58]. At this point, buckling has occurred. This more often occurs on a large scale (as the laminae bends) but can also manifest itself in the higher energy scenario through micro-buckling of fibers within the composite [32].

Kicher and Mandell [62] studied compressive buckling of laminated plates. For two simply supported edges and two free edges (see Figure 3.10), the critical loading, N_{CR} (force per unit length) is given below, Equation 3.23. With unloaded edges unsupported, this estimation has a form very similar to that for compressed, slender members. This equation suggests that tall, compliant plates have a low buckling strength, as one would intuitively believe.

$$N_{CR} = \frac{\pi^2 D_{yy}}{b^2} \quad 3.23$$

Post critical behavior and calculation of collapse loads for collapsing plates are generally quite complicated, even for isotropic materials (simple, closed form solutions are not available) [58]. Inelastic behavior complicates the problem further, since the tools used to compute elastic behavior no longer apply [63].

3.5. *Triangular Corrugation*

Triangular corrugation has been studied in some degree; as a blast protector under out of plane loading [16], for in-plane compressive loads [64] and under shear loading as a sandwich panel core [62]. However, these studies did not focus on the cellular aspects of the corrugated material. Therefore, determination of properties important to the study of cellular materials (e.g., relative density and densification strain) is in order.

3.5.1. Geometry

Three base variables describe the two dimensional geometry of the triangular corrugation used for samples under consideration, Figure 3.11. They are wavelength L , angle θ , and flute thickness t [64]. These govern the overall layer thickness and therefore the relative density of the finished product. The third dimension is the width, w . With laminated composites, the orientation of material within layers is also important, as it influences stiffness, strength, and buckling behavior.

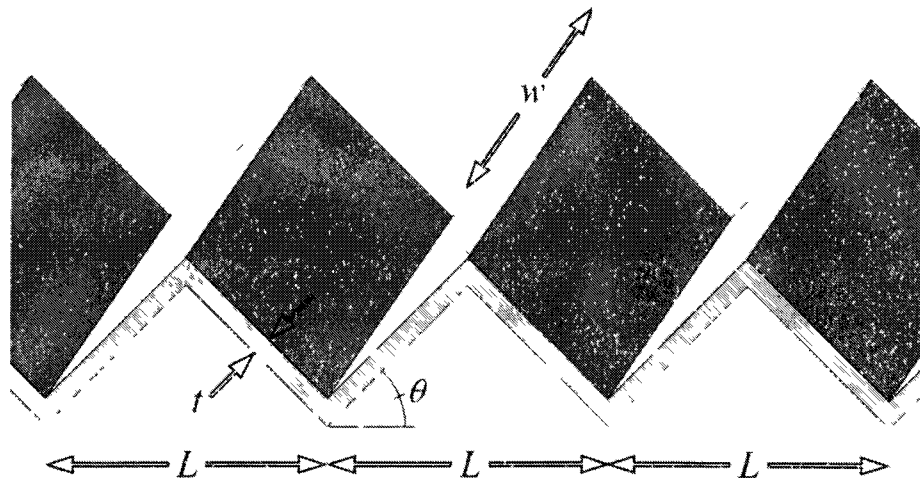


Figure 3.11. Triangular geometry.

When many individual layers are stacked, additional variables (e.g., layer orientation, layer offset) become important. The orientation of each layer with respect to one another is probably the most important of these in terms of its effect on overall behavior. We now consider properties.

3.5.2. Properties

Relative density is one of the most important properties governing the behavior of a cellular solid [1]. Relative density is defined as the ratio of solid material volume to total volume. Since the proposed corrugated material has a constant cross section within any ply, relative density ($\bar{\rho}$ or ρ/ρ_s) is simply the ratio of cross-sectional area of solid material to the total area. For a flute of corrugation, the area of solid material (A_s) is the product of its thickness, t , and length, l . Total area (A_T) is the product of the flute wavelength L and height h . The approximation is shown in the equation below.

$$\bar{\rho} = \frac{\rho}{\rho_s} = \frac{A_s}{A_T} = \frac{t \cdot l}{h \cdot L} \approx \frac{(t) \cdot (L/\cos \theta)}{(L \tan \theta) \cdot (L)} = \frac{t}{L \cos \theta \tan \theta} \quad 3.24$$

This estimation of relative density does not take into account the possibility for a bonding agent between layers. Use of adhesives will cause the measured density of a sample to be higher than above. Values for ρ_s can be found by the rule of mixture equations presented in chapter one. For a composite with fiber volume $V_f = 0.5$, fiber density of Kevlar 49 $\rho_f = 1.44 \text{ g/cm}^3$ and epoxy density of $\rho_m = 1.18 \text{ g/cm}^3$, resulting composite density is $\rho_s = 1.31 \text{ g/cm}^3$.

Another important property of cellular materials is the densification strain ε_D , as discussed in section 1.6. Densification strain in a cellular material occurs at a point on the stress-strain curve when the amount of stress required for continued densification rises rapidly, Figure 1.25. Although one may expect the densification strain to be equal to the porosity, $(1 - \rho/\rho_s)$, where all the free space of the material has been squeezed out, experience has shown that densification occurs sooner than this. Experience with testing of corrugated metal fabrics [6] and closed-cell foams [1] show that a slow increase in stress occurs when cell walls begin crushing together. For closed-cell foams, Gibson and Ashby [1] account for this and provide the following estimate for densification strain:

$$\varepsilon_D = 1 - 1.4 \left(\frac{\rho}{\rho_s} \right) \quad 3.25$$

From laminated plate theory and geometry of the corrugated triangular layers, an approximate maximum compressive stress for an entire corrugated sample can be estimated. First assume that there are a large number of cells within the sample, such that the sample width, w , is several times greater than the corrugation wavelength, L . Now consider a unit of corrugation of width w , and area A , Figure 3.12.

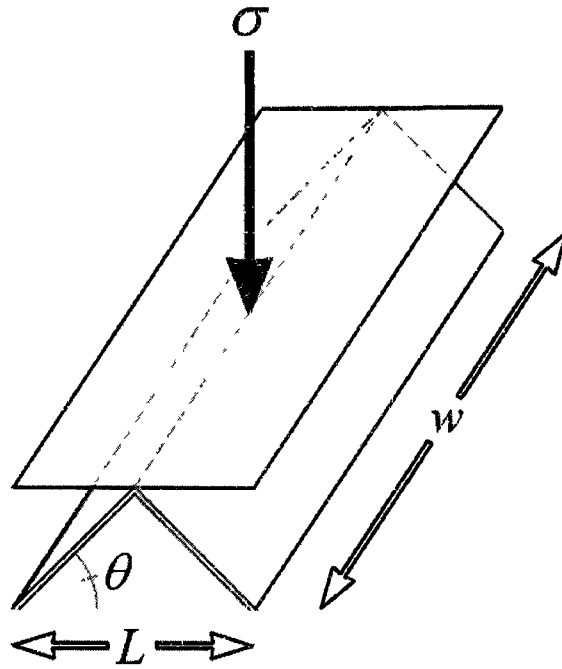


Figure 3.12. Unit of triangular corrugation under compression.

At buckling (maximum force), an area of width w , and length L , will be able to support a maximum stress σ_m . The maximum force F_m is simply:

$$F_m = \sigma_m \cdot A = \sigma_m \cdot L \cdot w \quad 3.26$$

The load is assumed to be shared equally between both plates, as shown in Figure 3.13.

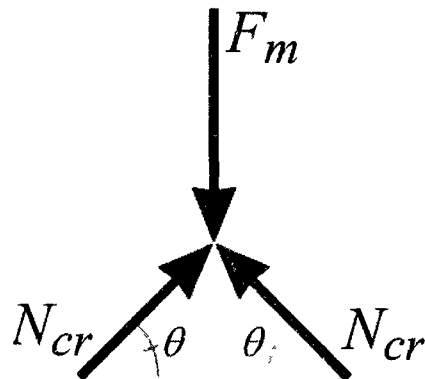


Figure 3.13. Free body diagram of loaded element.

The in-plane buckling of the plates load per unit length, N_{cr} (as found in section 3.4), can be related to the applied load as:

$$F_m = 2 \cdot N_{cr} \cdot w \cdot \sin \theta = \sigma_m \cdot L \cdot w \quad 3.27$$

Thus, the compressive buckling stress is simply:

$$\sigma_m = \frac{2}{L} \cdot N_{cr} \cdot \sin \theta \quad 3.28$$

Recall from Equation 3.23 that $N_{cr} = \frac{\pi^2 \cdot D_{yy}}{b^2}$ and $b = \frac{L}{2 \cdot \cos \theta}$ to find:

$$\begin{aligned} \sigma_m &= \frac{2}{L} \cdot \left(\frac{\pi^2 \cdot D_{yy}}{b^2} \right) \cdot \sin \theta = \frac{2}{L} \cdot \left(\frac{\pi^2 \cdot D_{yy}}{\left[\frac{L}{2 \cdot \cos \theta} \right]^2} \right) \cdot \sin \theta \\ \sigma_m &= \frac{8 \cdot \pi^2}{L^3} (D_{yy} \cdot \cos^2 \theta \cdot \sin \theta) \quad 3.29 \end{aligned}$$

This estimation should be used as an upper bound for compressive strength. As previously discussed, it does not take into account the non uniform (point) loading or stress concentrations. Additionally, its accuracy is directly related to the accuracy of the plate stiffness calculation D_{yy} .

4. 1. SAMPLE DESIGN AND FABRICATION

Thus far, the proposed structure has been reviewed and important properties have been estimated. Experimenting with fabrication methods, raw materials, and assembly procedures must be conducted and followed by testing to verify that the proposed structure will perform as expected. Once a viable and cost-effective method for sample fabrication is established, compressive testing will highlight potential areas for improvement. It is expected that through this learning process, there will be an increase of the mechanical performance (most importantly, specific strength).

Samples of the triangular corrugated type were built from two different types of commercially available woven Kevlar fabric. Overall relative density could be controlled through the choice of different base materials (type of Kevlar fabric or epoxy used) and assembly technique (number of plies in each laminae, bonding agents used). Mechanical properties, including compressive strength and densification strain, will depend on these choices as well.

4.1. *Sample Construction*

All samples were built to have approximately the same exterior dimensions, from twelve individual layers, Figure 4.1. Samples were nearly cubic. Their average height was 54 mm while their length and width were 60 mm.

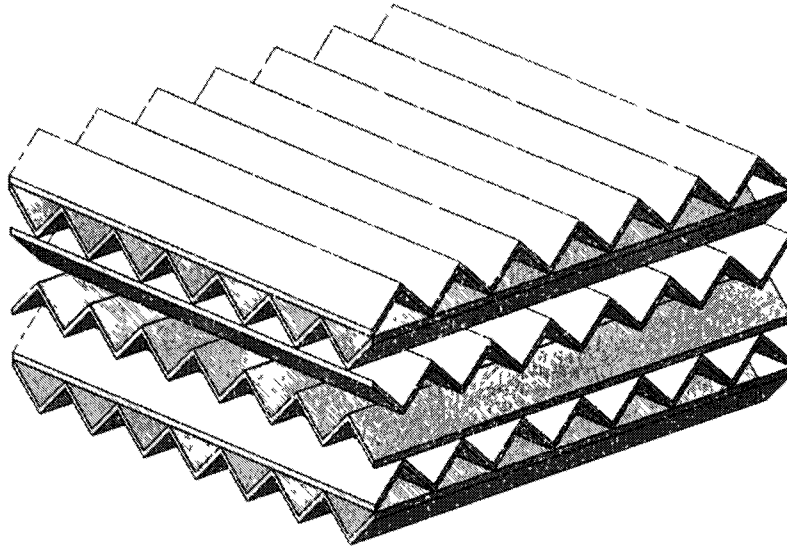


Figure 4.1. Assembly of the proposed sample.

Each sample was constructed using techniques similar to those used for conventional composites (wet hand lay-up). An aluminum mold was used to achieve the desired finished shape of each Kevlar-epoxy layer. This technique, described in further detail below, is commonly used for marine, automotive, and aerospace applications due to its low cost and reasonable equipment requirements. Although a number of additional tools and techniques (such as vacuum bags and autoclaves) might be used, the chosen method is suitable for this research, as equipment investment is minimum, and an excellent finish can be achieved. Disadvantages to the wet lay-up process include low production rates, difficulty in maintaining part uniformity, long cure times at room temperature, and high volatile emissions [37].

4.1.1. Mold Fabrication

For wet-layup composite fabrication, a mold that matches the final shape of the product is used. As the matrix cures (hardens), the finished composite takes on the shape of the

mold. The molds used for the composite lay-ups were made from an aluminum alloy since metal molds tend to perform well after repeated use [37]. The choice of aluminum alloy is due to its low-cost and machinability. Solid block aluminum was milled into the final shape by ERAU (Embry-Riddle Aeronautical University) machine shop staff. An engineering drawing of one half of the mold is shown in Figure 4.2. A matching half is used to squeeze the layup into the desired shape.

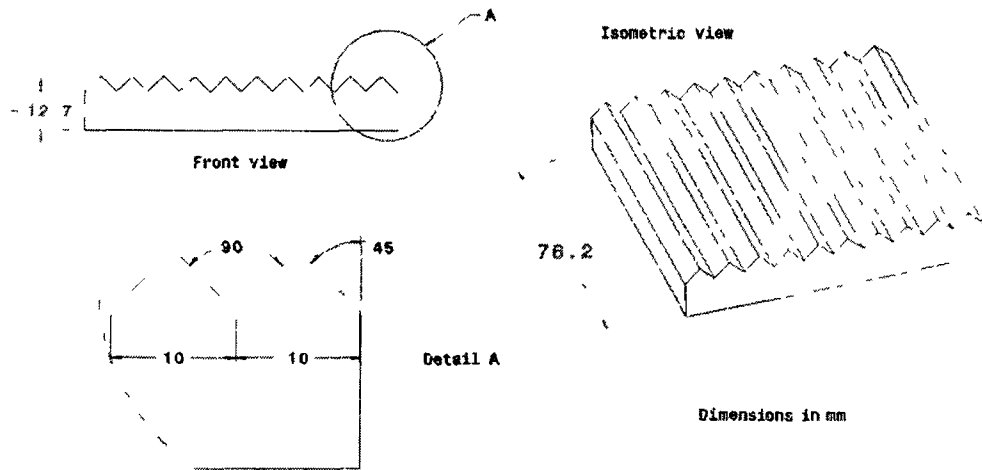


Figure 4.2. Engineering drawing of one half of mold.

The finished mold, Figure 4.3, was used for a large number of layups, each having the potential to damage the surface. Keeping the surface of the mold in good condition after each lay-up is important, as separating the cured aramid-epoxy layers can be difficult and possibly damage the composite [37]. Sandblasting and fine sanding with a fine paper (400-600 grit) after approximately twelve layups was found helpful in maintaining a smooth surface of the mold.

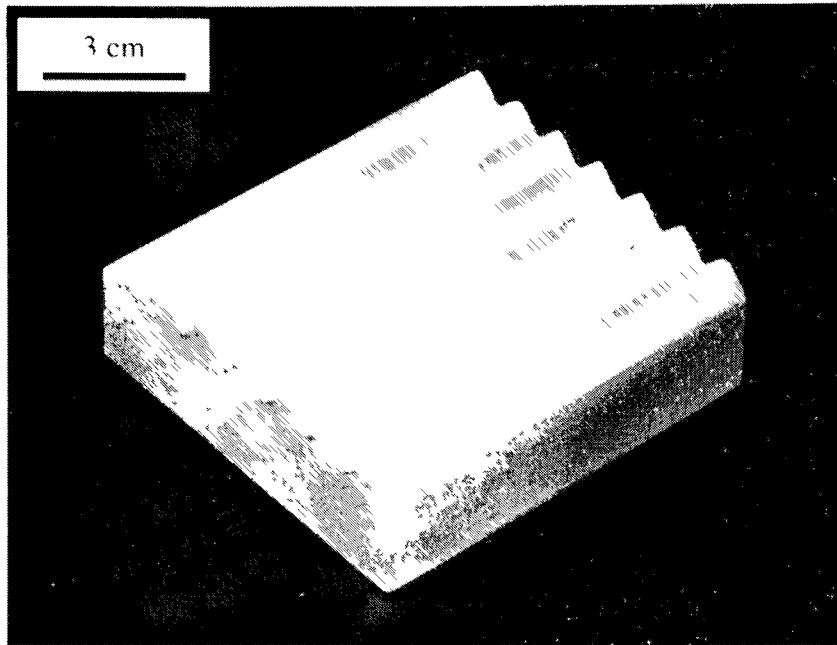


Figure 4.3. One half of the finished mold used for lay up.

Furthermore, a mold release wax (Finish Kare Products, South El Monte, CA) was applied to the mold before each layup to encourage release of the layup (a very common technique for molded composites). Other mold releases, such as dry aerosol film, liquid polyvinyl alcohol (PVA), woven release fabric, and bagging film were attempted, but did not yield satisfactory results in terms of separation or final laminae surface quality.

4.1.2. Ply Lay-Up

Individual layers were made using the technique described below each having one or more plies of Kevlar fabric. The weave orientation (how the fabric is oriented) is important as it affects the stiffness and buckling strength (as discussed in the previous section). Several orientations were examined.

To construct individual layers using a wet hand lay-up technique, the mold must first be cleaned and prepared with the mold release wax. Then, a piece of fabric (such as fiberglass, carbon, or aramid) is impregnated with a mixed resin such as polyester, vinyl ester, or epoxy [37]. The aramid fabric used for these experiments was either style 120 or 281. Both are plain weaves, but style 281 is a heavier, thicker, and stronger fabric.

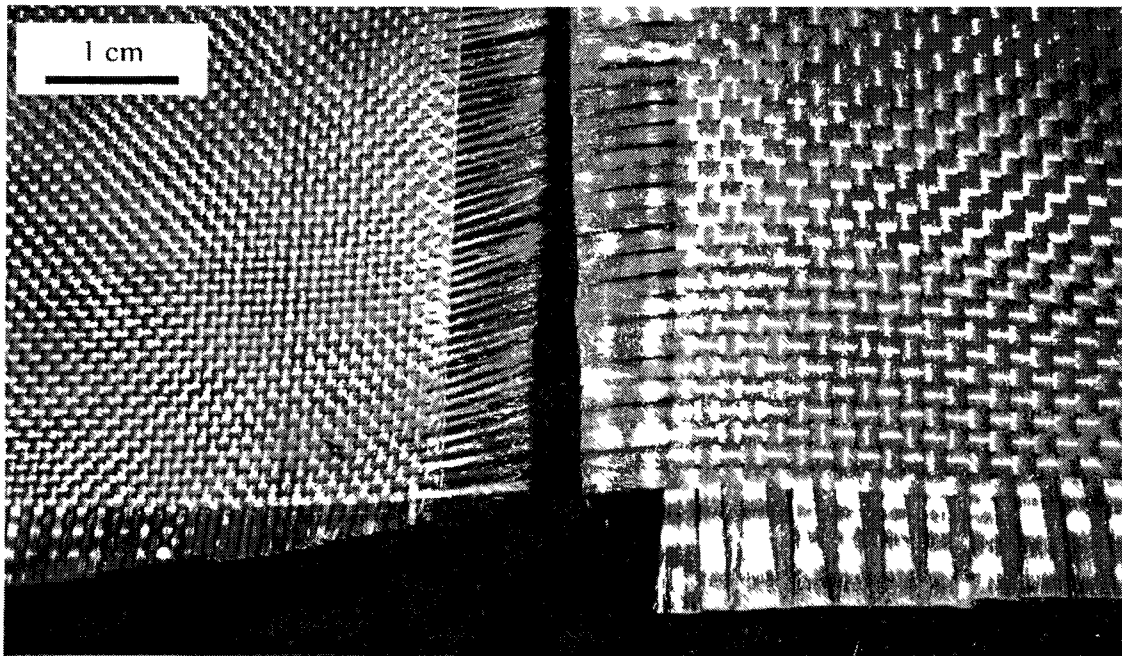


Figure 4.4. Plain weave Kevlar fabric comparison; left is style 120, right is style 281.

The Kevlar fabric used for this research was purchased from Aircraft Spruce and Specialty Co., Peachtree City, GA. Details of the two aramid fabrics are shown below along with those from a number of other woven Kevlar fabrics.

Table 4.1. Woven Kevlar fabric comparison [44].

Style	Weight (g/m ²)	Weave Style	Yarns/cm Warp x Fill	Thickness (mm)	Denier (g/9000 m)
Light weight					
166	30.6	Plain	37 x 37	0.04	55
120	61.1	Plain	13 x 13	0.11	195
220	74.7	Plain	9 x 9	0.11	380
Medium weight					
181	169.8	8h satin	20 x 20	0.23	380
281	169.8	Plain	7 x 7	0.25	1140
285	169.8	Crow	7 x 7	0.25	1140
328	230.9	Plain	7 x 7	0.33	1420
Unidirectional					
143	190.2	Crow	39 x 8	0.25	380 x 195
243	227.5	Crow	15 x 7	0.33	1140 x 380
Woven Roving					
1050	356.6	4x4 basket	11 x 11	0.46	1420
1033	509.4	8x8 basket	16 x 16	0.66	1420

To fabricate a single laminae, the appropriate fabric is cut to a slightly oversized dimensions, then wetted with mixed West System epoxy (Gougeon Brothers, Inc., Bay City, MI). For this epoxy system, a hand pump dispenses the correct amount of resin and hardener for a single “stroke” of each (recall that this ratio is important for complete cure). The epoxy was purchased from West Marine (Daytona Beach, FL), and is commonly used in marine and aerospace applications. The fast cure 205 hardener was used for all layouts, as it provides good mechanical properties and a reasonable cure time (roughly 12 hours). Appendix A contains detailed technical information on the different West Systems epoxies.

Once the fabric was wetted, it was placed between two halves of the mold. Pressure is applied to sandwich (44.5 N of lead shot) the aramid-epoxy between the mold halves, and the setup was left to cure for a minimum of 8-12 hours at room temperature (25 °C). After curing, excess material was removed and the mold separated, Figure 4.5. A finished layer is shown, Figure 4.6. The mold was then prepared for another layer by applying the release wax and the process was repeated. Every twelve samples, the mold halves were cleaned and sanded.

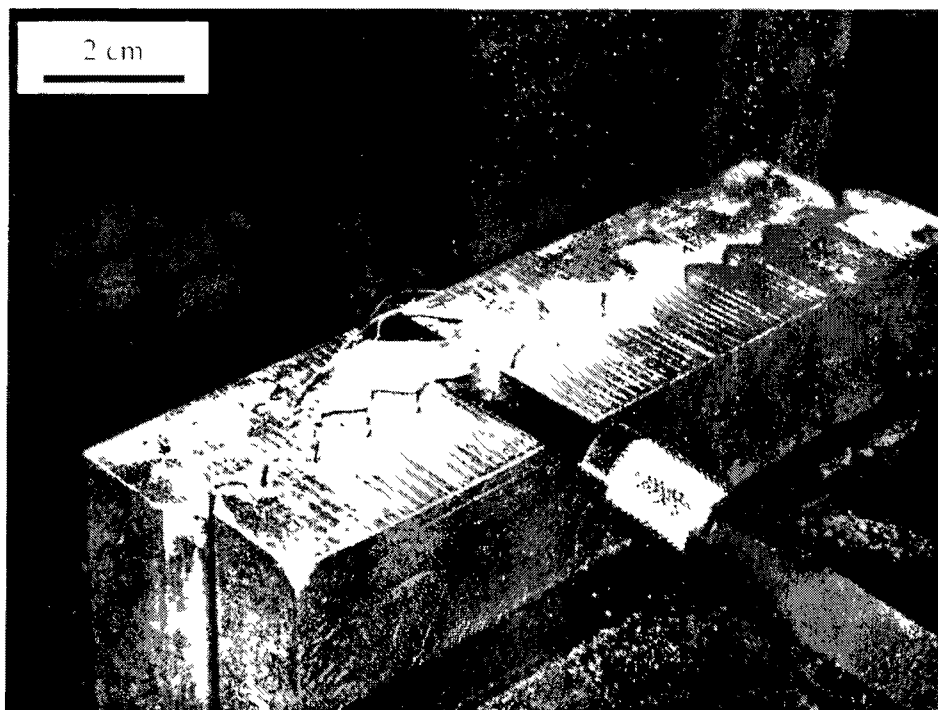


Figure 4.5. Removing excess material from layer.

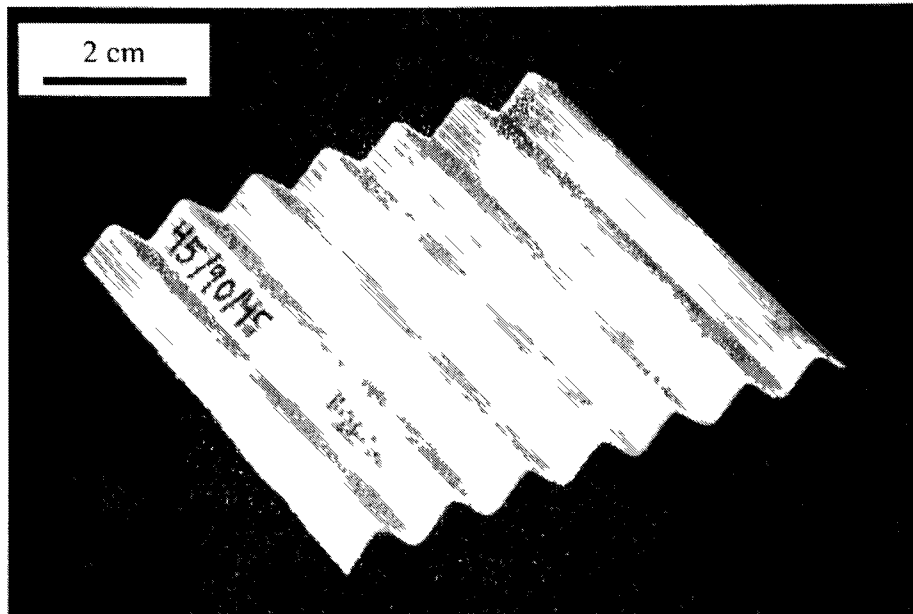


Figure 4.6. Completed single layer of an amid-epoxy.

4.1.3. Layer Assembly

When individual layers are stacked to construct a 3-D sample, multiple orientations can be chosen which affect the load paths through the corrugated structure. Two possible orientations include “in-phase” and “out-of-phase”, Figure 4.7. For the “in-phase” configuration, the contact points between layers cause some amount of shear loading, while the out-of-phase arrangement causes bands of compression between the contact points, Figure 4.8.

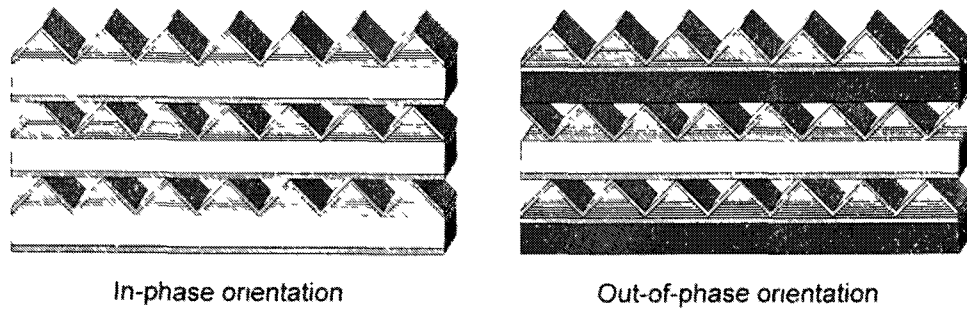


Figure 4.7. Comparison of different orientations.

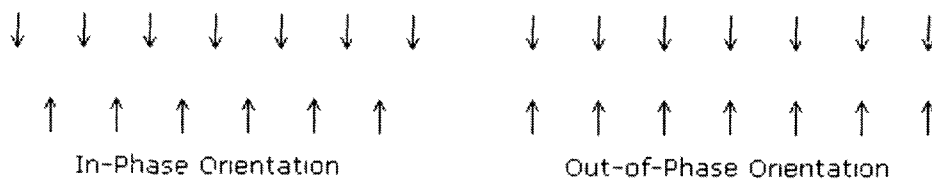


Figure 4.8. Plate loading due to different orientations.

The choice of adhesive between layers is important. As the triangular corrugation is compressed, the reaction force can induce lateral loading (especially near the sample boundaries), leading to shear stress within the adhesive. If the adhesive fails, force cannot be effectively transmitted to adjacent layers. However, more adhesive will add excess weight to the structure. A strong, tough adhesive that is properly suited to the laminae is critical.

Adhesive is added to each individual layer as they are stacked in the assembly. A “strip” of the mixed epoxy applied along the apex of each layer was an effective method. When the adjacent layer is stacked, a number of discrete points bond together as the epoxy cures. These are the points where load is transferred through the structure, so ensuring that the epoxy is applied is important.

5. SAMPLE DETAILS AND TEST RESULTS

5.1. Sample Overview

A table outlining each sample assemblies is shown below. Samples were built in the numerical order given. After construction, each sample was tested (as indicated in the table). Knowledge gained during the test was used in the design of the next sample in the sequence to improve the performance.

Table 5.1. Sample overview.

	Fabric	Plies	Fabric Orientation	Laminae Matrix Epoxy	Inter-Laminae Epoxy	Phase	Testing
1	#281	1	0/90	105/205	5-min	In-phase	Quasi-static
2	#281	1	±45	105/205	105/205	In-phase	Quasi-static
3	#281	1	±45	105/205	105/205	Out-of-phase	Quasi-static
4	#120	1	0/90	105/205	105/205	In-phase	Quasi-static
5	#281	1	±45	105/205	MetlWeld	Out-of-phase	Quasi-static
6	#120	3	0/90, ±45, 0/90	105/205	MetlWeld	Out-of-phase	Quasi-static
7	#120	3	±45, 0/90, ±45	105/205	MetlWeld	Out-of-phase	Quasi-static
8	#120	3	0/90, ±45, 0/90	105/205	MetlWeld	Out-of-phase	Dynamic
9	#120	3	0/90, ±45, 0/90	105/205	MetlWeld	Out-of-phase	Dynamic

The trend in sample design above illustrates a few important concepts about the design for increasing strength. First, increasing the number of plies to 3 and using the style 120 fabric was found to be beneficial. Additionally, MetlWeld adhesive was used for samples 5 and on.

Table 5.2. Comparison of sample measurements.

	Mass (g)	Length (mm)	Width (mm)	Height (mm)	Area (mm²)	Volume (cm³)	Density. (g/cm³)
1	31.1	65.1	64.2	54.7	4179.4	228.61	0.136
2	32.1	66.4	65.9	56.1	4369.1	245.02	0.131
3	32.1	66.4	65.3	56.6	4338.2	254.54	0.131
4	18.1	66.3	65.7	55.0	4355.9	239.58	0.076
5	42.1	66.3	65.6	55.0	4350.0	240.00	0.175
6	55.7	65.8	65.8	55.4	4329.6	239.86	0.232
7	56.8	65.0	65.4	55.5	4244.5	235.57	0.241
8	55.6	66.5	66.1	56.0	4395.7	246.16	0.225
9	51.9	67.6	67.0	56.8	4529.2	257.26	0.202

Mass readings were taken using a scale with 0.1 g accuracy. Length measurements are an average of four readings for height, and two readings each for width and length. A digital caliper with 0.01 mm accuracy was used for these measurements. Area, volume, and density were calculated using average values. The increase in sample mass (along with density) due to the MetlWeld adhesive for sample 5-9 is apparent.

5.2. Testing Setup

Measurement of force-displacement was conducted quasi-statically for the majority of tests. Under relatively slow compression, failure of individual layers within the sample could be observed and photographed without the need for high-speed equipment. A 7.1 megapixel Olympus Camedia C-7000 digital camera was used to photograph the test specimens. Aperture stop was fixed at $f/8.0$ to maintain a maximum depth of field and clear focus, and CCD sensitivity was set to an ISO 400 equivalent. Shutter speed was allowed to adjust automatically for proper exposure, and was generally in the 1/13 – 1/4 sec range. A fiber optic light source was used to illuminate the samples.

A strain rate of 0.001 s^{-1} was used for the quasi-static tests, Samples 1-7. This corresponds to a rate of about 3.3 mm/s, which is within the quasi-static regime. Digital photographs of the testing event were recorded approximately every 0.5 mm of crosshead displacement (about 1% strain).

5.2.1. Quasi-static Testing Apparatus

A 150 kN capacity Tinius-Olsen (Tinius-Olsen Corp, Horsham, PA) screw driven electromechanical testing machine was used for quasi-static compression testing, Figure 5.1. The machine uses a pen plotter to record measured force and displacement values. Force range can be set to 3 kN, 15 kN, 60 kN, or 150 kN. If the upper limit of a range is reached during a test, range is automatically increased. The range for displacement can be set to 12.5 mm, 50 mm, 250 mm, 500 mm, or 1250 mm. Crosshead speed can be set between 0.2 in/min (5.1 mm/min) and 20 in/min (50.8 mm/min).

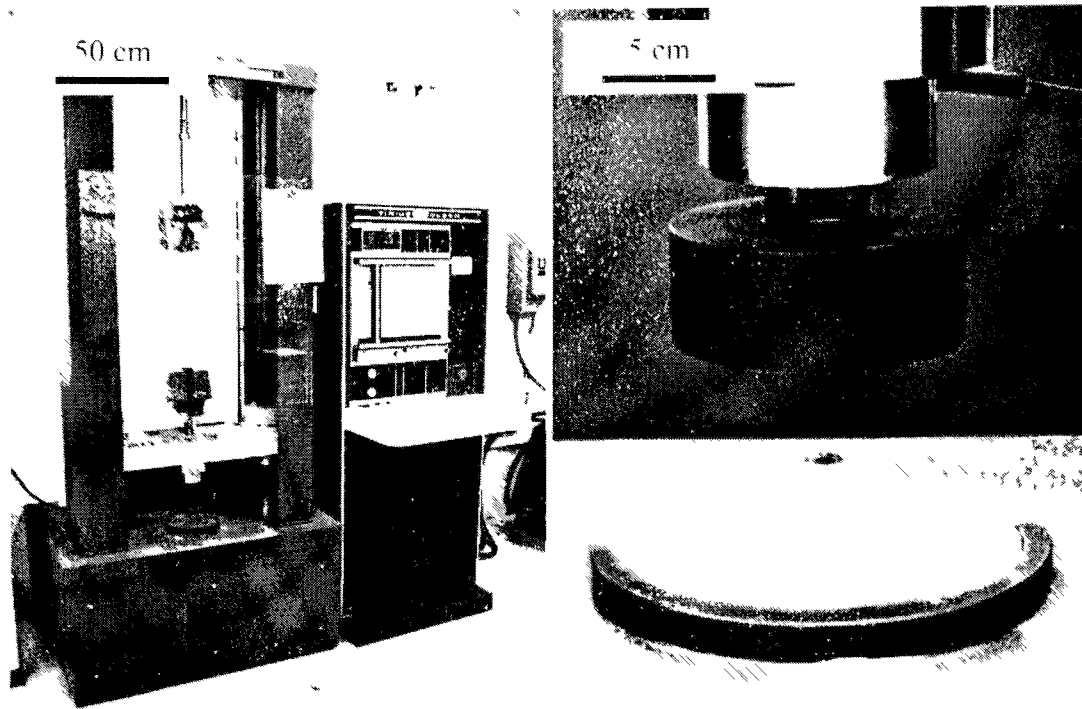


Figure 5.1. Compressive testing machine and striker.

For this work, the 3 kN and 50 mm were the range settings. This provided reasonable limits for the sample size and strength tested. Several samples went beyond the 3 kN limit; the Tinius-Olsen machine then automatically changed the range to 15 kN.

5.2.2. Dynamic Testing Apparatus

For the dynamic (impact) tests, an Instron Dynatup 9250HV (Instron Corporation, Norwood, MA) drop tower impact machine was used, Figure 5.2. The Dynatup is compatible with a number of impact test standards, such as ASTM D-3763, ASTM D-5420, NASA ST-1, and more. This machine uses gravitational potential energy for lower velocity impacts, and spring assist for higher velocities. Impact masses can be changed using removable weights from 8.3 kg to 28.3 kg (as configured). The maximum velocity is 20 m/s, but in all cases the maximum energy is limited to 1,600 J.

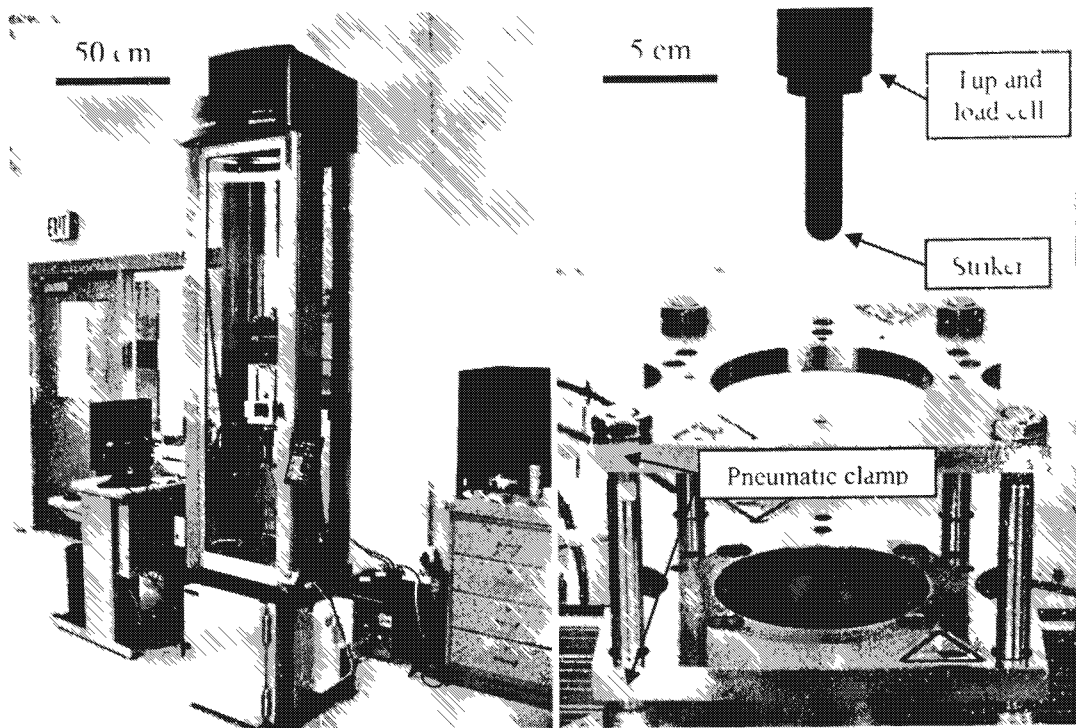


Figure 5.2. Dynamic testing machine and platen.

A hemispherical, 12.7 mm diameter striker was used for testing, Figure 5.2. Indenter stress σ_{ind} is reported, and is calculated from the measured force F_{ind} and the cross sectional area $A = \pi (12.5 \text{ mm}/2)^2 = 122 \text{ mm}^2$

$$\sigma_{ind} = \frac{F_{ind}}{A} \quad 5.1$$

This striker is compatible with test standard ASTM D-3763-06, used to test the penetration of plastics. The impact event is recorded onto PC after signals are passed through the A/D converters and conditioners. Instron Dynatup Impulse Data Acquisition v2.0.3 records and saves the data and allows graphing of displacement, load, and more.

There is no established limit on sample thickness in the ASTM standard, but the penetrating insert had a depth of approximately 45 mm, Figure 5.2. If this penetration

depth is exceeded, this could result in erroneous data, as there will be a large spike in the force transmitted to the tup and load cell.

The ASTM standard test method requires the specimen to be clamped securely, which is accomplished with the pneumatic apparatus, Figure 5.2. The test method recommends a 76.2 mm diameter hole in the clamping. This was determined to be too large for the corrugated composite samples which had widths of roughly 66 mm. Aluminum shims were machined at the ERAU machine shop to increase the clamping area. These shims measured an outside diameter of 102 mm, an inside diameter of 25.4 mm, and a thickness of 3.5 mm. They were inserted above and below the sample in the pneumatic clamp, and proved effective at preventing slippage of the samples under impact.

ASTM D-3763 recommends an impact speed between 0.041 m/s and 4.16 m/s for the test. This does not compare to the range of velocities seen with bullets or fragments that are explosive in nature, but should show the behavior of the corrugated samples under a concentrated, dynamic load. Impact mass for these runs was kept constant at 8.4 kg.

5.3. *Experimental Results*

Experimental results for each sample are now reviewed. Stress-strain diagrams are included. Photographs of quasi-static compression tests were taken approximately every 1% strain. A sequence of these photographs at 0%, 25%, 50% and 75% is documented. During the discussion, layers with corrugation running parallel to the sight of the camera will be referred to as “longitudinal” while layers with corrugation running perpendicular to the camera will be referred to as “transverse” layers.

5.4. *Sample 1*

Results from sample 1 are shown in the stress-strain diagram below, Figure 5.4. During compression, epoxy joining the different layers failed early on at a majority of the contact points. The result is that very little energy is absorbed when trying to buckle and bend the plates. Instead, much a smaller amount of energy is used to break each individual layer at its apexes and flatten each layer. Cracking was heard throughout the test as the adhesive failed at these points; generally these audible acoustic emissions were accompanied by a small drop in the compressive stress. After compression, the sample had been flattened, but the buckling and bending of the plates (desirable for high energy absorption) did not occur.

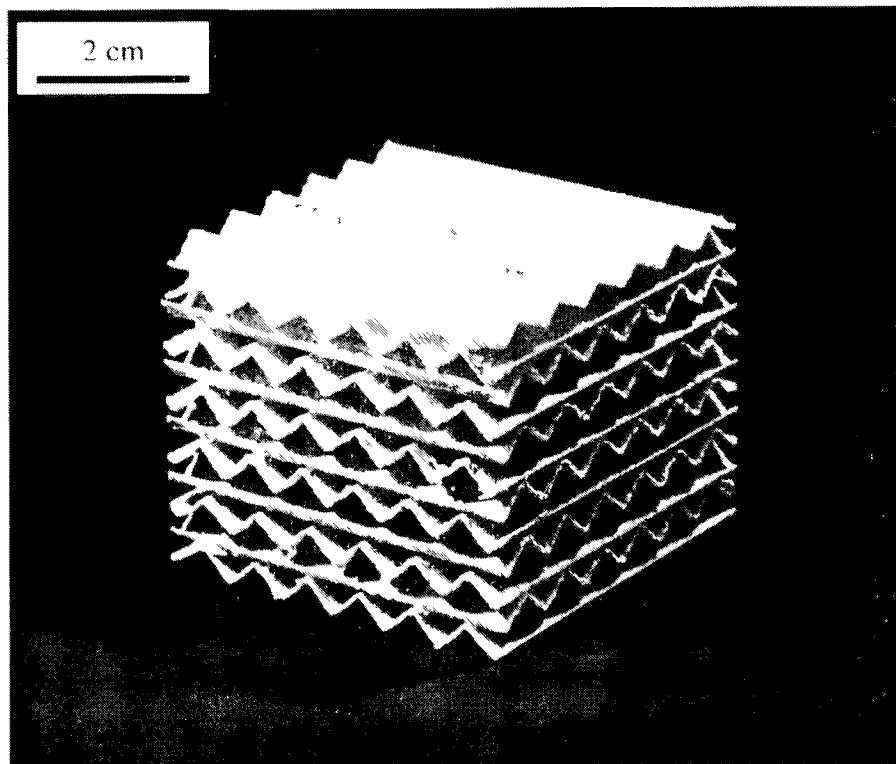
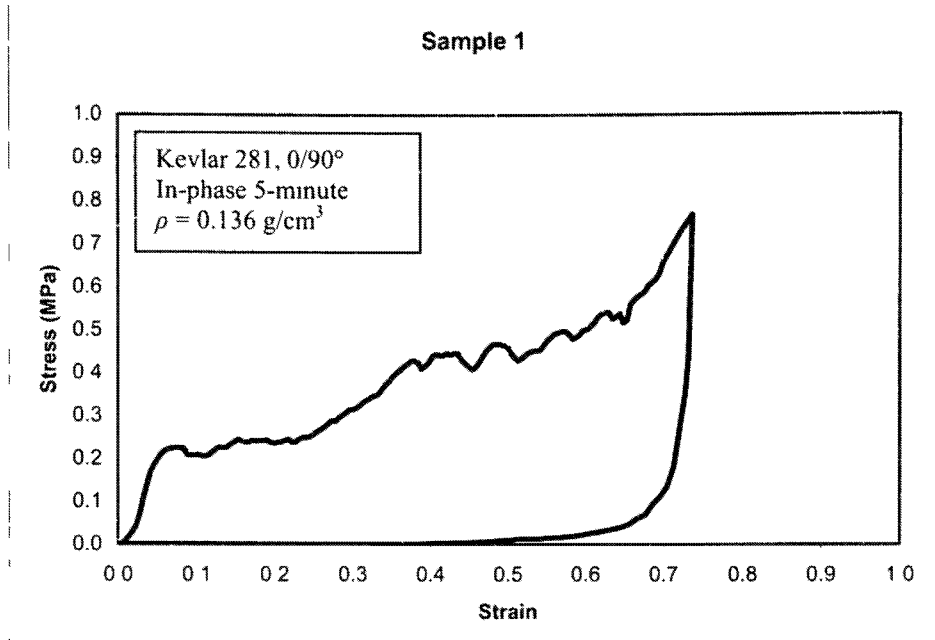


Figure 5.3. Finished sample 1.



The flattening of individual layers can be seen in the sequence below. This is due to failure of the bonds, and was initiated at the layers near the middle of the sample. As these longitudinal layers are flattened and “squeezed out” of the sample, they begin to cover the view of other transverse layers; this behavior is clearly visible in Figure 5.5, starting at the 25% strain frame.

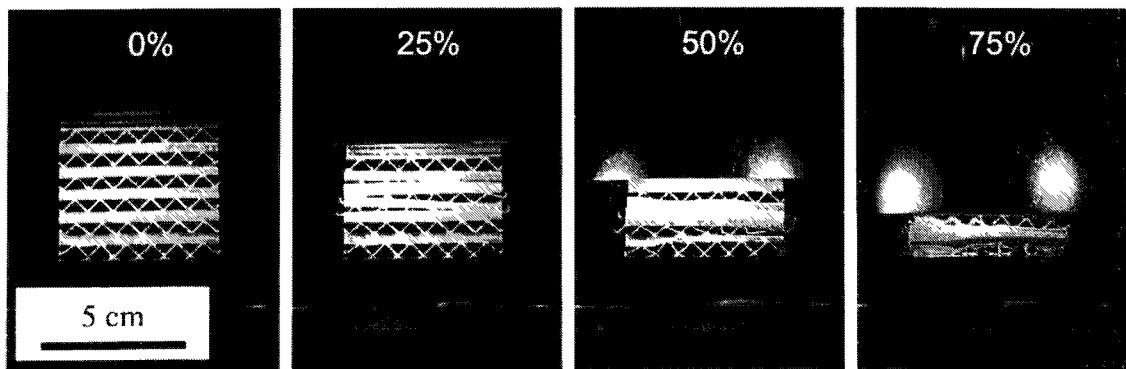


Figure 5.5. Crushing sequence of sample 1.

5.5. *Sample 2*

Sample 2 was assembled in the same way as the previous sample, but assembled with the stronger West Systems 105/205 epoxy. This change was made to alleviate the flattening of the corrugations which resulted in a low compressive stress of sample 1. This sample is seen below, Figure 5.6. Another change was made to the fiber orientation, as this sample used the 45-degree orientation.

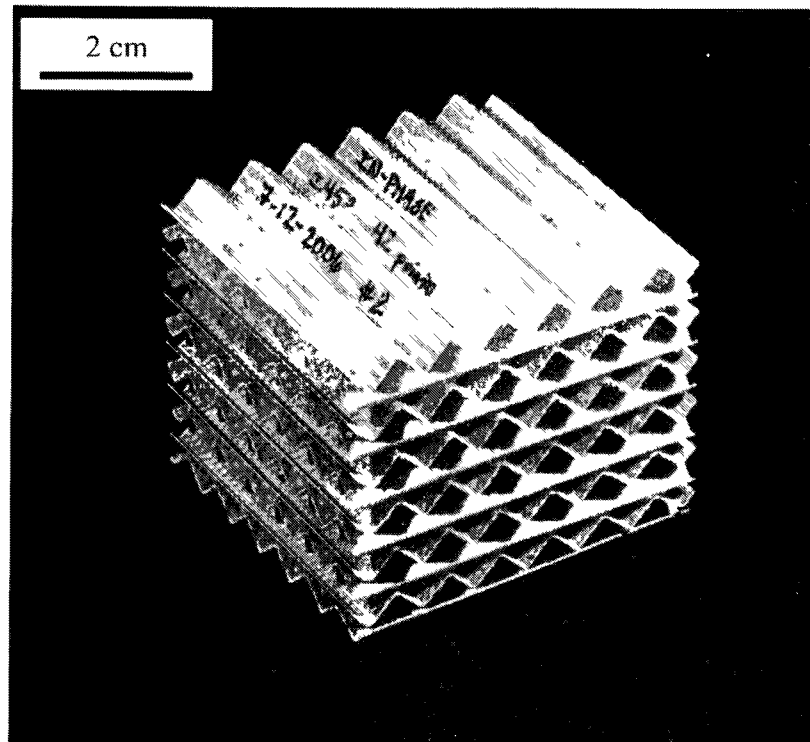


Figure 5.6. Finished sample 2.

A higher quality bond between layers resulted in increased strength of Sample 2, Figure 5.7. There was also a decrease in the number of layers which were flattened and “squeezed” out, as can be seen in the sequence of photographs, Figure 5.8. For this sample, the force range approached 15 kN as the sample reached densification.

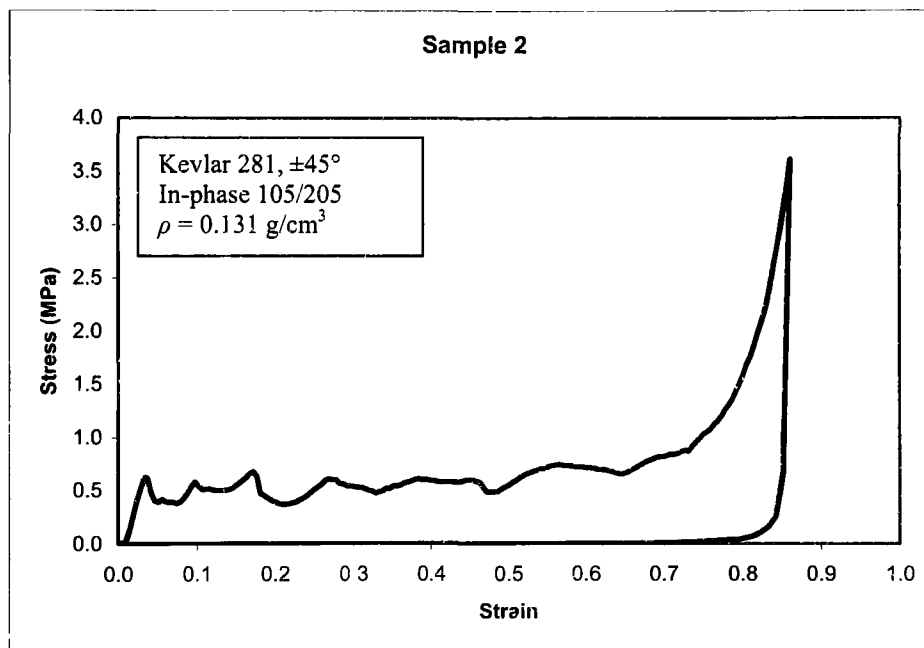


Figure 5.7. Stress-strain diagram, sample 2

Interestingly, some of the layers in the second sample held their corrugated shape much longer than other layers within the sample. This shows a small amount of inconsistency in the manufacture of the layers, and more importantly that the onset of failure within a layer decreases its strength, causing the whole layer to collapse.

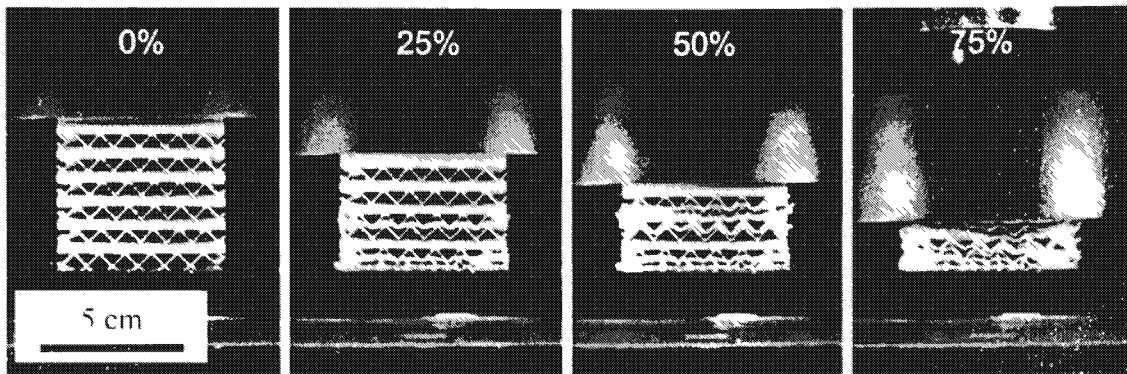


Figure 5.8. Crushing sequence of sample 2.

Another observation is that the bottom layer was one of the first to fail, as seen in Figure 5.8 at 25% strain. Also, an important feature of the in-phase orientation can be observed at 50%, where longitudinal layers (parallel to camera sight) are aligned as they stack upon one another.

5.6. *Sample 3*

The third sample tested the effect of changing the phase (orientation) of separate layers. With “out-of phase” orientation, the loading on individual layers produces point loads directly opposing the reaction loads, reducing shear load in the plate. Sample 3 is shown below, Figure 5.9. Style 281 fabric was used, in a ± 45 degree orientation, with a single ply per layer.

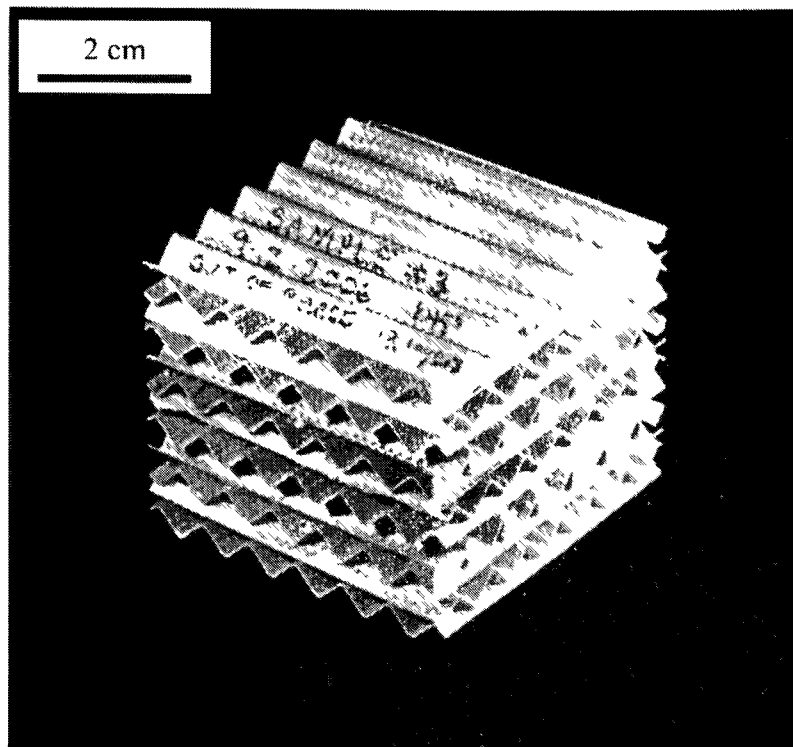
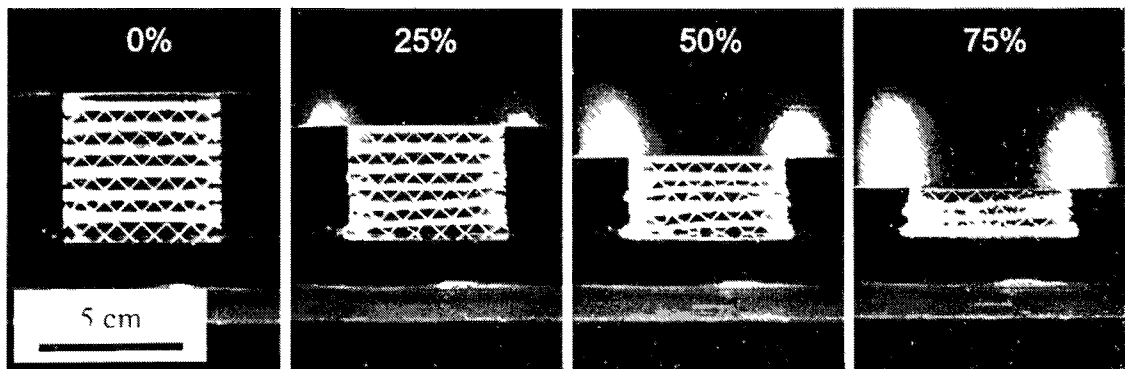
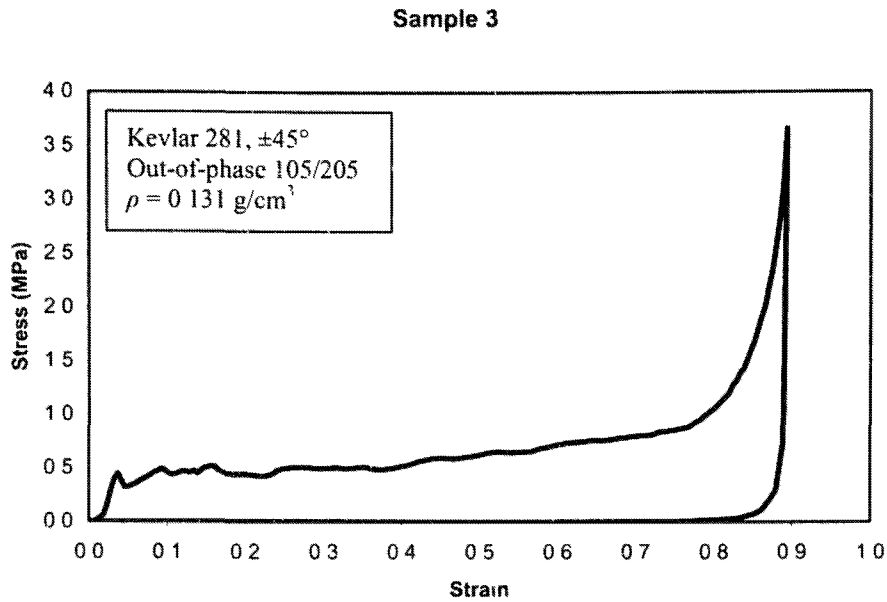


Figure 5.9. Finished sample 3.

The third sample results show a fairly smooth plateau stress, but a slightly lower strength than the previous sample, Figure 5.10. While the strength was not enhanced by the change in phase, sample 3 exhibited a flatter stress-strain curve, a desirable trait for energy absorbers. Intra-layer adhesion was still reasonable, however the bottom layer failed early on in a fashion similar to the second sample, seen at 25% strain. Bending and buckling of the plates is also now more apparent, as seen in the sequence for this sample.



5.7. *Sample 4*

To test the performance of lower density samples, a single ply of the lighter style 120 fabric at 0/90 degree orientation was used. Additionally, facesheets made of single-ply 0/90 degree Kevlar #120 and West Systems 105/205 were attached to the top and bottom layers to prevent their flattening under load – a common premature failure mechanism seen in the earlier samples. The finished sample is shown below, Figure 5.12.

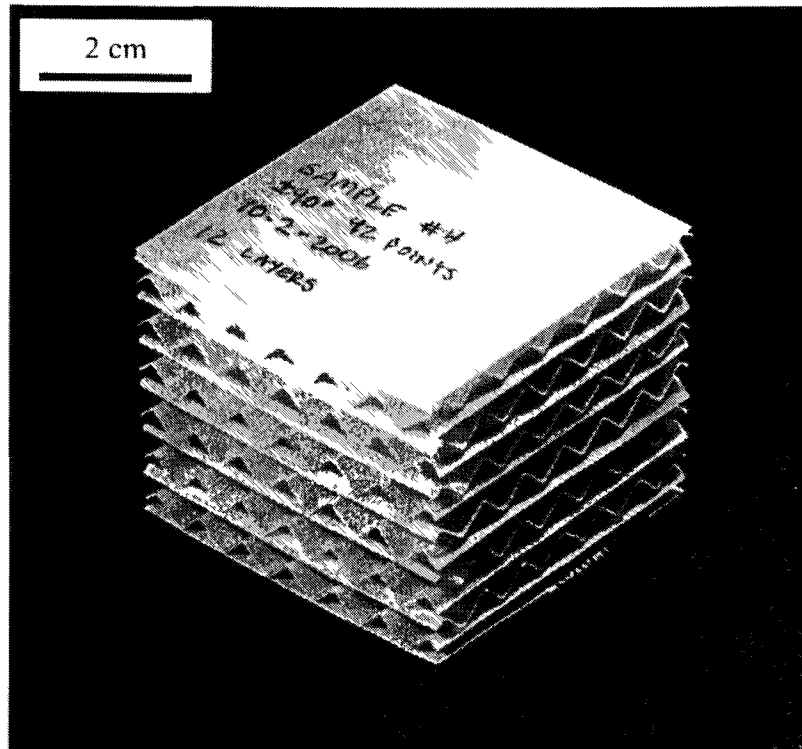


Figure 5.12. Finished sample 4.

The lighter Kevlar was used for the fourth sample in order to study how energy absorption related to sample density. However, the low stiffness of the layers was not well suited with the chosen corrugation geometry, as the plates buckle under little load. With a relatively low buckling strength, the plates collapse but the bonds between the layers hold, which preventing individual layers from flattening (a desired trait).

Another interesting behavior observed with Sample 4 was the relatively early increase in compressive stress as the sample densified, Figure 5.13. At the 80% strain level, the stress had risen to nearly 5 times the plateau stress (which was roughly 0.1 MPa) The more dense Sample 3 had a stress rise of two times the plateau stress at 80% strain. This is not consistent with the normal behavior of cellular materials, where less dense samples usually densify at higher strain levels.

Sample 4

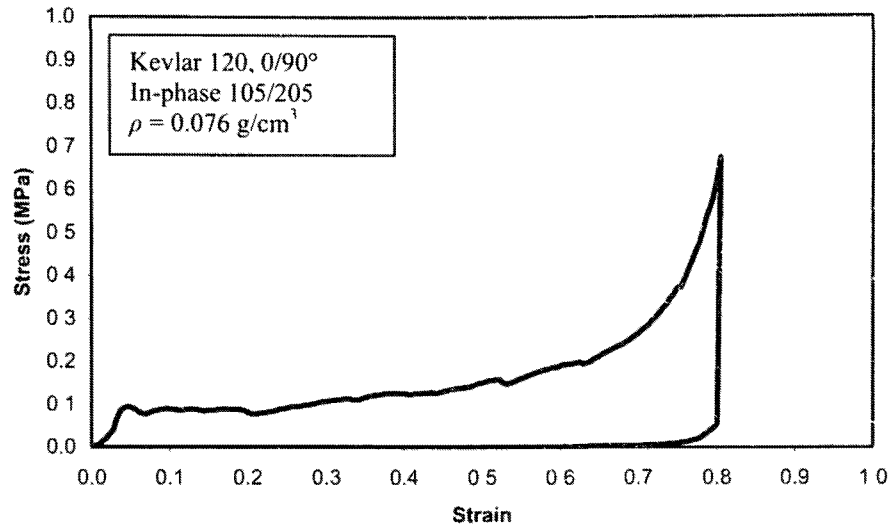


Figure 5.13. Stress-strain diagram, sample 4

A behavior which was noticed in the post test review, Figure 5.14, was that failures of individual layers did not happen at once, but portions of a given layer were crushed early on. This is apparent at 50% strain, where some layers do not remain flat through the test, supporting the idea that initial defects and their location play a large role in failure of the composite plates.

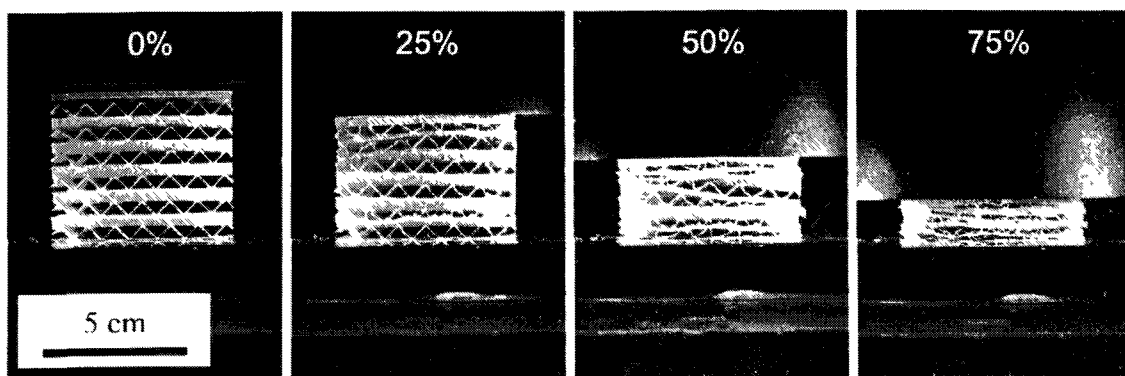


Figure 5.14. Crushing sequence of sample 4.

Incorporation of facesheets helped to prevent the top and bottom layers from flattening since the points of contact and bonds are supported on both side. By observation of the test, Figure 5.14, and the post-test sample, facesheets helped prevent premature flattening of the top and bottom.

5.8. *Sample 5*

With knowledge that a single ply of lighter #120 fabric was not suited for the chosen corrugation geometry, the heavier #281 fabric was used again, but this time in a single ± 45 degree orientation. For sample 5, a different bonding epoxy was used to test whether failures between layers could be delayed to higher loadings. The chosen adhesive was MetlWeld brand epoxy (System Three Resins, Auburn, WA) and this was used to assemble the layers in the “out-of-phase” orientation. MetlWeld is a toughened epoxy with good adhesion to a number of materials. In comparison to the West Systems 105/205 system (used to assemble samples 2-4), it should support higher stress at a higher strain before failure. The lightweight style 120 fabric was again used for the facesheets, maintaining a 0/90 degree orientation. Sample 5 is shown below, Figure 5.15.

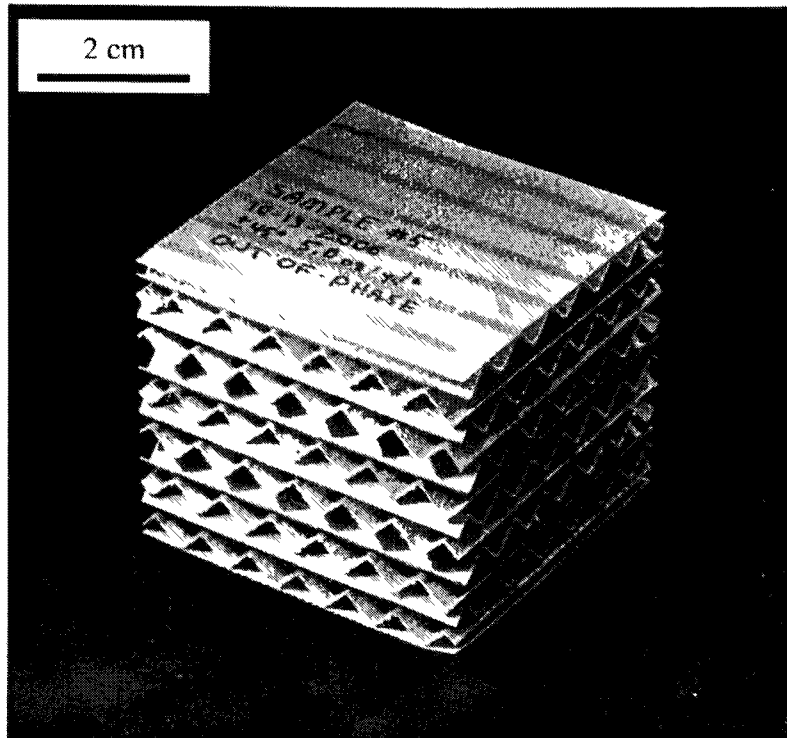


Figure 5.15. Finished sample 5.

A much stronger bond between layers was achieved with the MetlWeld epoxy adhesive than was seen in the previous samples. Post-testing examination of the sample verified this, as the sample maintained a higher stress level than samples with similar laminac, as seen in the stress-strain diagram, Figure 5.16. The added weight of the MetlWeld (and resulting increase in relative density) resulted in slightly lower performance with respect to the energy absorbed per unit mass.

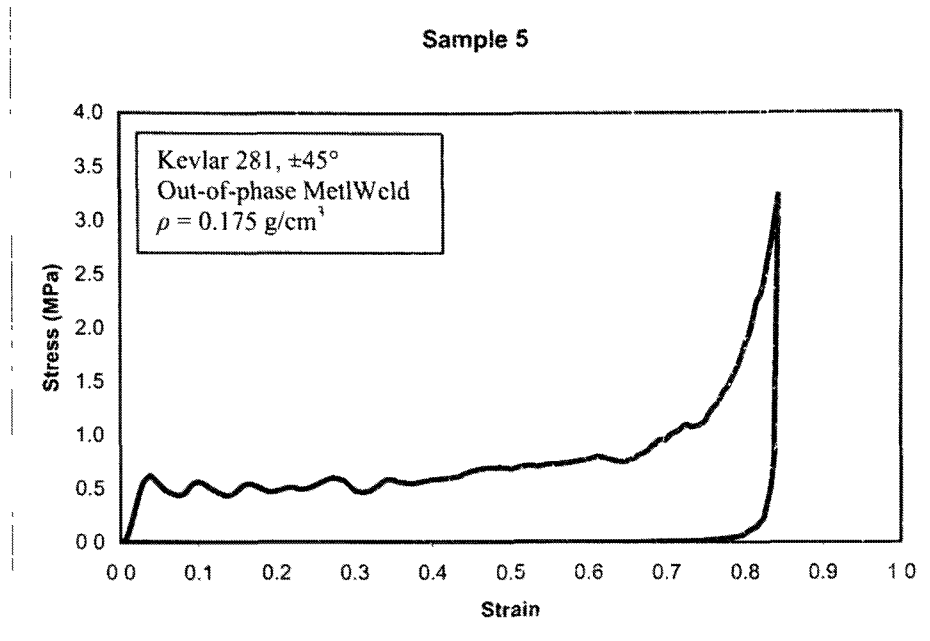


Figure 5.16. Stress-strain diagram, sample 5.

The sequence below shows the different layers failing, and again confirms the theory that facesheets on the top and bottom layers would help prevent premature failure of those layers, as can be seen with the crushing sequence, Figure 5.17. Adding the facesheets does not appear to contribute significantly to the strength, but did facilitate a more uniform crushing through the test.

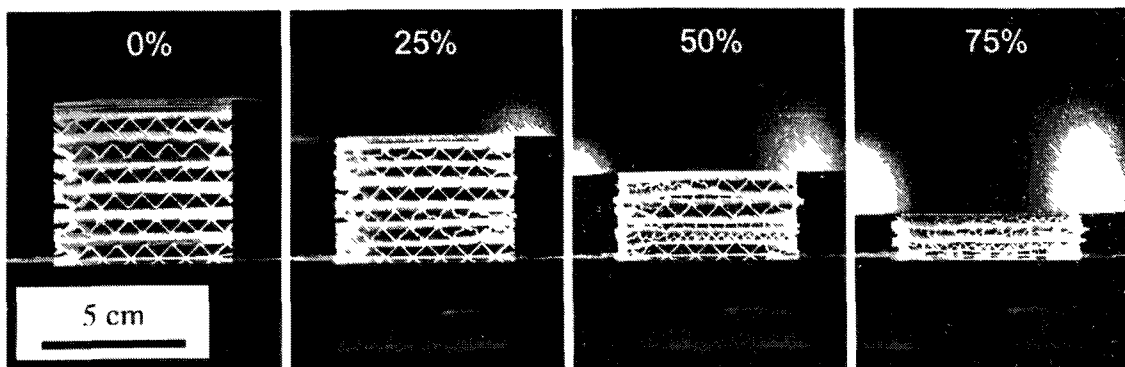


Figure 5.17. Crushing sequence of sample 5.

As mentioned, another major difference with sample 5 was the use of MetlWeld adhesive between layers. This prevented most separation between layers during compression, and revealed that stiffness of the laminated aramid-epoxy plates had become the limiting feature. This sample revealed that overall compression performance is sensitive to a balance between individual plate between stiffness and shear strength of the adhesive bonds between layers.

5.9. *Sample 6*

Sample 5 revealed that plate buckling was a limiting factor in the overall compressive strength of a sample. Tailoring of layer stiffness was attempted in Sample 6 by using three layers of the lighter style 120 fabric to increase stiffness without a dramatic increase in mass, Figure 5.18. The outer two layers were oriented at 0/90, and the center layer was maintained near the ± 45 degree orientation. From laminate theory, this geometry should yield a high stiffness for the bending (from the 0/90 plies), as well as good shear resistance (from the ± 45 ply).

With three plies in the laminate, sample density is higher. Cellular material theory predicts that this higher density should result in densification at a lower strain than the single ply samples.

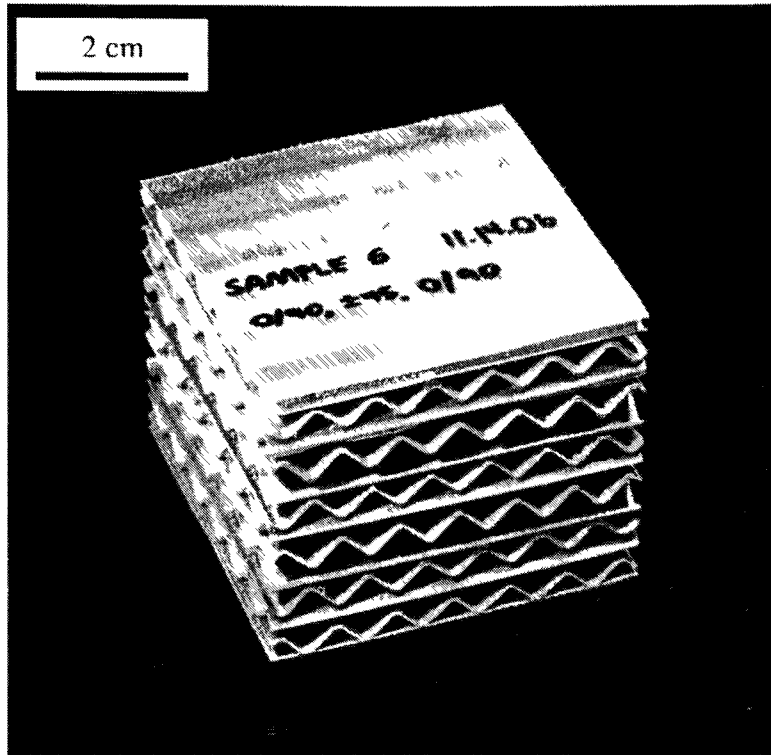


Figure 5.18. Finished sample 6.

MetlWeld epoxy adhesive was again used to bond the layers in the “out-of-phase” orientation as well as the style 120 facesheets to the top and bottom, (this had shown to be an effective way to increase the sample strength).

With stiffer composite layers within Sample 6, the load at failure was higher than any of the previous samples by a factor of nearly two, Figure 5.19. A linear increase in stress up to yield at 5% strain, resulted in a Young’s Modulus of about 500 MPa. However, this stiffness does not take into account the compliance of the testing device. The densification strain occurred earlier than previous samples, as would be expected with a more dense sample.

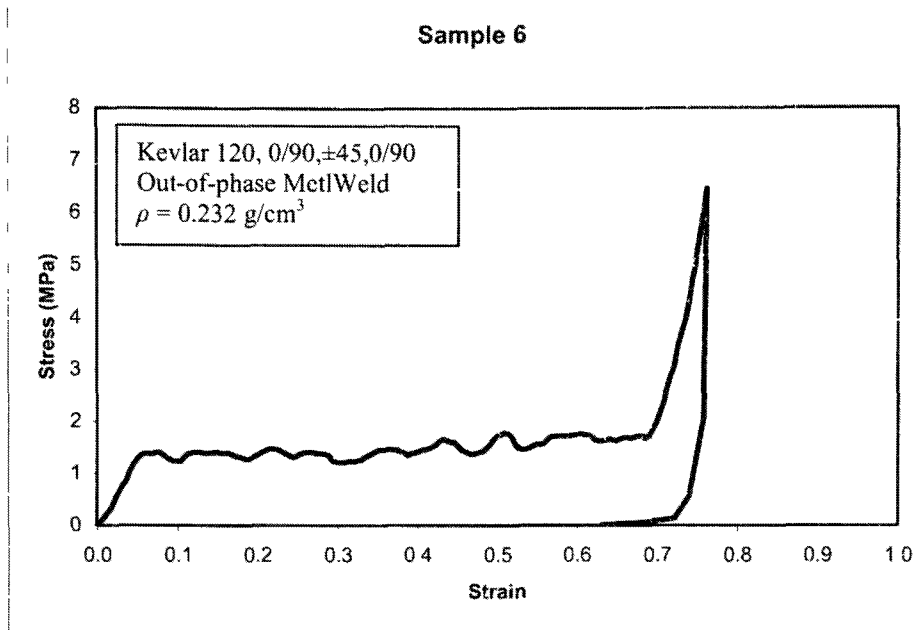


Figure 5.19. Stress-strain diagram, sample 6.

Sample six had the best overall balance of layer stiffness (obtained through the use of multiple layers of Kevlar), and adhesive shear strength between layers. A fairly consistent failure of sample layers is seen in the sequence of photographs, Figure 5.20. This is also apparent in the stress-strain diagram where the plateau stress remains fairly constant until densification at a strain of about 69%.

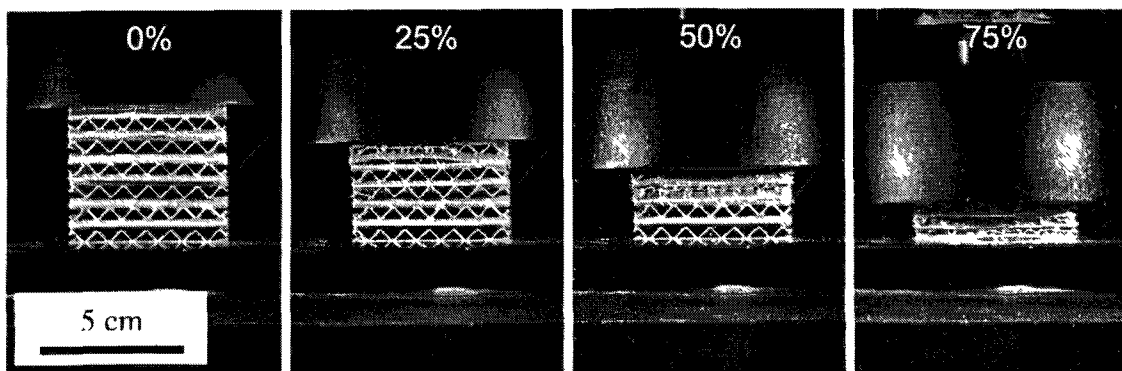


Figure 5.20. Crushing sequence of sample 6.

5.10. Sample 7

As with Sample 6, a multiple-ply approach was used for each layer. Three plies of the lightweight style 120 Kevlar were used, in a $\pm 45, 0/90, \pm 45$ orientation. By plate theory, the overall bending stiffness (and therefore buckling strength) of this orientation is lower than that of sample 6. This is due to less fibers running parallel to the load. It does have the advantage of maintaining a higher shear stiffness (due to the higher number of 45-degree fibers), which could be useful to assemblies with in-phase orientation. This sample was assembled with the out-of-phase orientation, Figure 5.21.

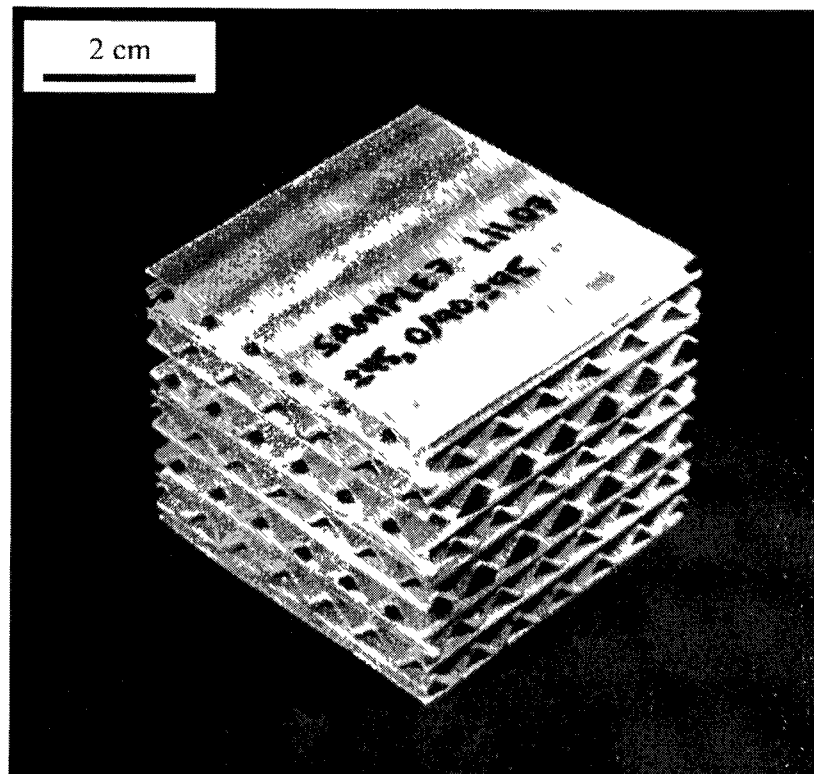


Figure 5.21. Finished sample 7.

As with sample 6, results of Sample 7 confirmed that increasing the stiffness of plates within the corrugated layers produces a higher plateau stress, Figure 5.22. The overall energy absorbed was slightly less than that of Sample 6. An important distinction

between this sample and the previous was a decrease in smoothness of the plateau, which could be flaw dependant. Another feature seen on the stress-strain diagram was an initial hardening, similar to a densification, around a strain of about 66%.

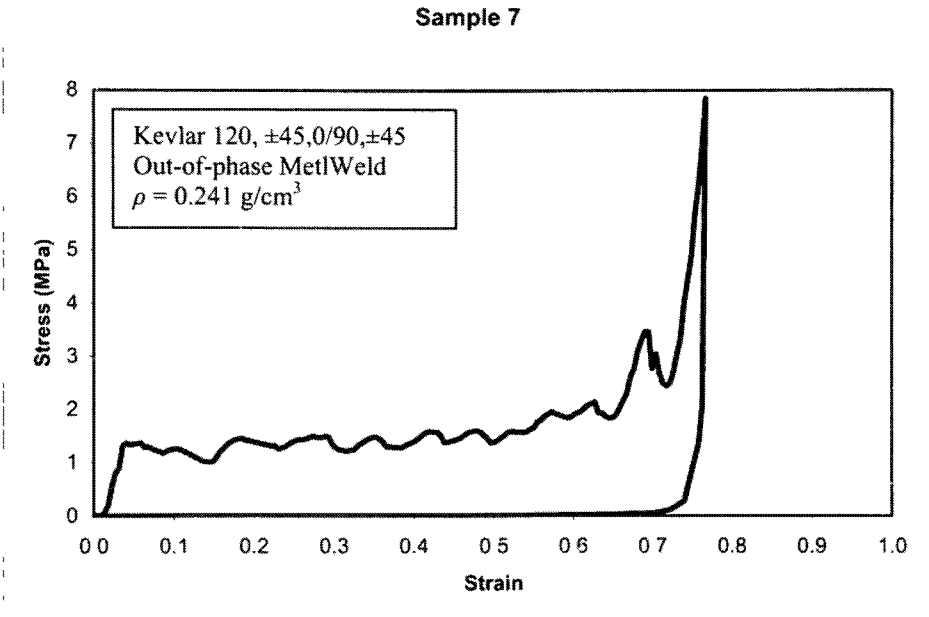


Figure 5.22. Stress-strain diagram, sample 7.

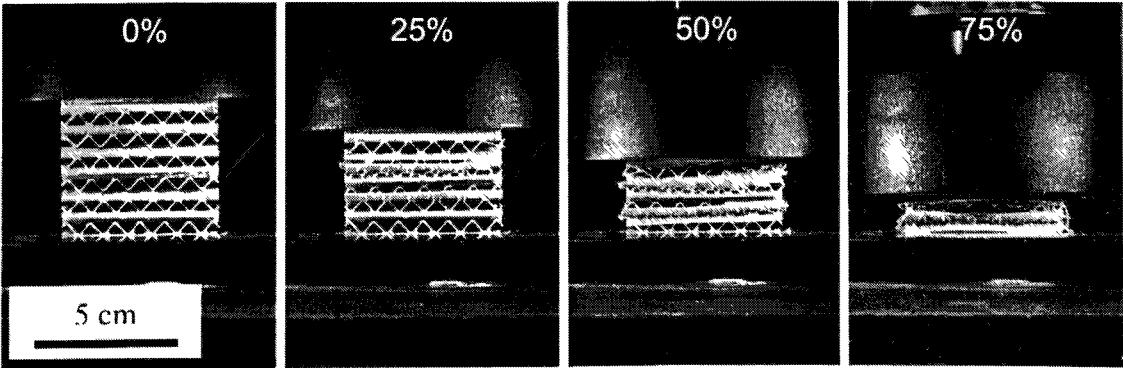


Figure 5.23. Crushing sequence of sample 7.

5.11. Sample 8

Sample 8 was built in the same fashion and orientation as sample 6, Figure 5.24. It was tested under dynamic loading conditions to study the penetration resistance of the corrugated aramid. Crosshead speed at impact for this test was 1.67 m/s, with crosshead mass $m = 8.4$ kg, and impact energy $E = 11.7$ J.

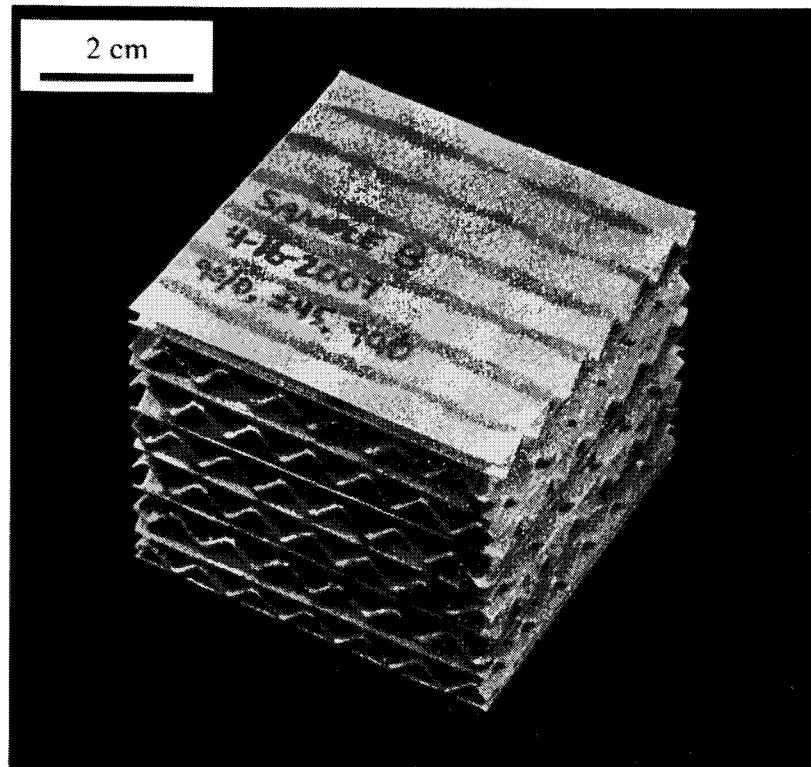


Figure 5.24. Finished sample 8.

The stress-displacement diagram recorded from the Instron software is seen below, Figure 5.25. With an initial impact energy of 11.7 J, the penetration depth was 14 mm. The slow rise in stress up to nearly 5 mm is mostly due to the increase in contact area as the hemispherical insert penetrates the facesheets and top corrugated layer. A stress of nearly 10 MPa was recorded during this initial penetration. Another increase in the stress at 9 mm displacement is likely due to penetration of the second corrugated layer.

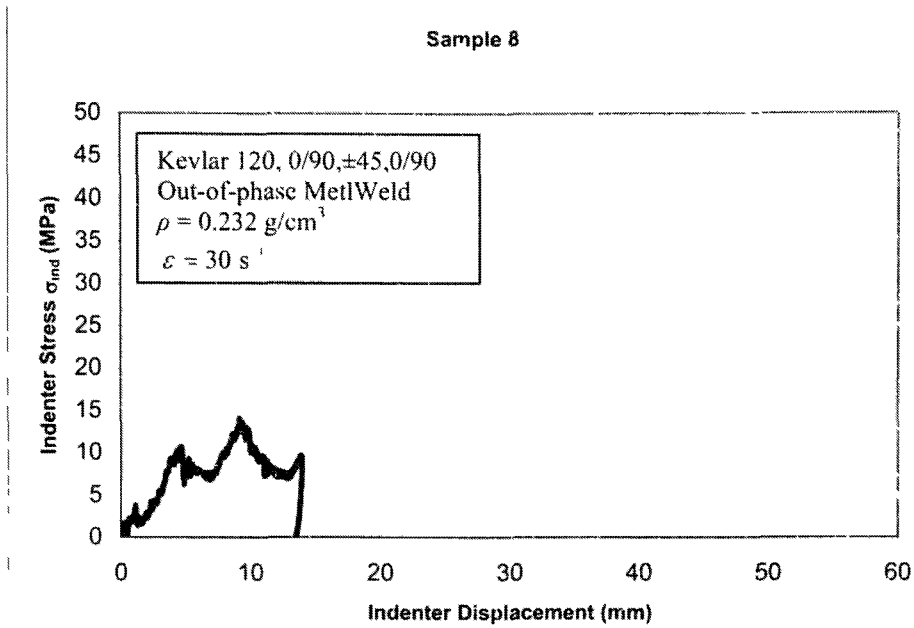


Figure 5.25. Stress-displacement of sample 8.

Post-test investigation revealed that portions of the corrugated sample away from the point of impact were not damaged, Figure 5.26. The overall structure remained intact since the damage was localized, a potentially desirable characteristic.

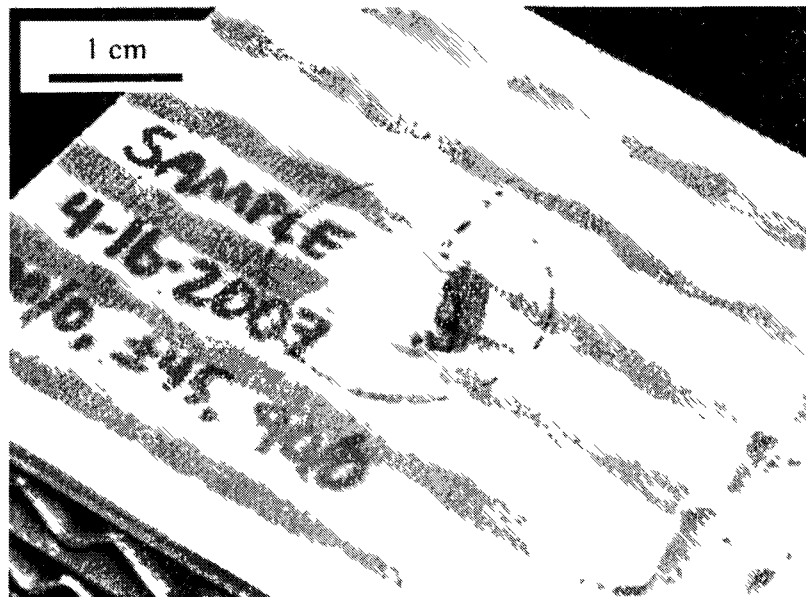


Figure 5.26. View of sample 8 after penetration test.

5.12. *Sample 9*

Sample 9 was constructed and tested in the same fashion as the previous sample. Figure 5.27. It was built to the same specifications in order to verify the behavior of the dynamic results. A higher initial velocity was used, $v = 4.16$ m/s and impact energy $E = 72.7$ J (impacting mass was not changed).

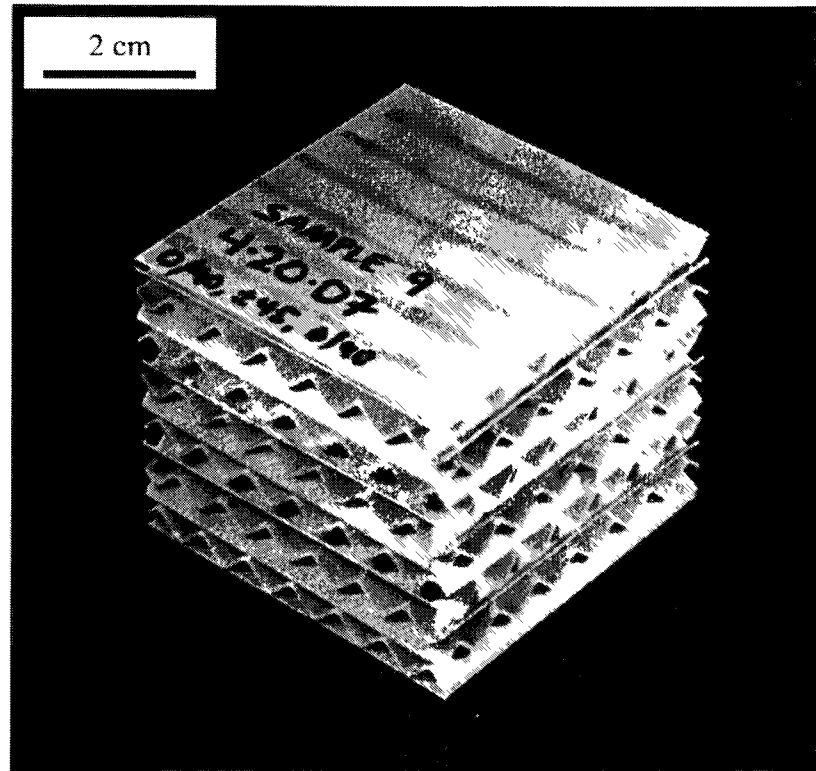


Figure 5.27. Finished sample 9.

The stress-displacement diagram, Figure 5.28, reveals behavior through the initial 45 mm of impact consistent with the previous test. An increase in the stress after contact of the striker is seen, as well as a spike near 9 mm displacement (also seen in sample 8).

However, the energy of the striker had not been dissipated fully when the tup and load cell came into contact with the sample. This caused a large increase in force between 40 mm and 50 mm displacement. Note that this is not densification as seen with the earlier samples in quasi-static testing. Interestingly, this high load did not damage or permanently deform the structure beyond the penetration due to the striker. The localization of the damage witnessed in the previous test was similar to that seen with sample 8, but deeper.

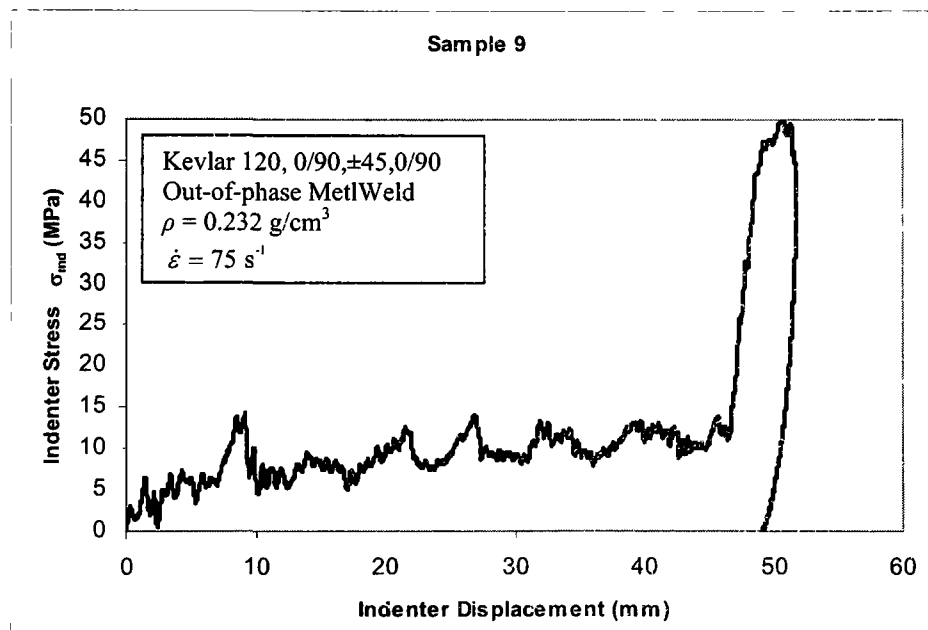


Figure 5.28. Stress-displacement behavior of sample 9.

5.13. Comparison of Quasistatic Results

Overall, plateau strength increased as knowledge was gained during the design and fabrication of samples. The summarized results,

Table 5.3, show the important properties of the cellular solids and the test results for that sample.

Table 5.3. Comparison of mechanical properties from quasi-static testing.

	Density (g/cm ³)	Relative Density	Approximate Densification Strain	Plateau Stress σ_{pl} (MPa)	Absorbed Energy/Mass (J/g)	Absorbed Energy/Vol (J/cm ³)
1	0.136	0.103	~	0.42	~	~
2	0.131	0.100	0.72	0.55	3.007	0.394
3	0.131	0.100	0.76	0.61	3.213	0.420
4	0.076	0.058	0.70	0.15	1.209	0.091
5	0.175	0.133	0.75	0.72	2.798	0.491
6	0.232	0.177	0.69	1.66	4.234	0.983
7	0.251	0.192	0.66	1.41	3.968	0.957

Relative density was calculated from the sample density, ρ , and base material density $\rho_s = 1.31 \text{ g/cm}^3$. Plateau stress σ_{pl} , reported in the table above, was calculated at 50% strain for all samples. The densification strain as reported in the above table was used for calculation of the energy absorbed per unit volume and energy absorbed per unit mass. Due to the adhesive failure between layers for sample 1, densification strain is not reported and energy absorption is calculated for the overall compression test, to 70% strain.

By comparing compressive strength and relative density, it can be seen that a two-fold increases in strength does not require doubling the relative density. Sample 6 has the best performance in terms of specific compressive strength (σ_{pl}/ρ), and Sample 4 has the lowest specific strength.

6. RESULTS AND ANALYSIS

Through persistence with development of corrugated composite samples, improved mechanical performance was generally observed (in terms of stress and stiffness). An important aspect of these materials is their mechanical behavior and performance in comparison to other energy absorbers. One sample of aluminum alloy foam and one sample of aluminum honeycomb were tested for this purpose, and their quasi-static compressive stress-strain behavior is reported. Additionally, two samples of aluminum alloy honeycomb (with facesheets adhered) were tested for penetration resistance, and the force-displacement data reported. Lastly, suggested improvements for the corrugated aramid-epoxy are covered.

6.1. *Validation of Predicted Results*

It was speculated that measured relative density would be higher than that calculated due to the inter-layer adhesive used for final sample assembly. The anticipated behavior for relative density was consistent with calculated values, Table 6.1. Measured relative density is found from measured density, ρ , divided by the base material for Kevlar-epoxy, $\rho_s = 1.31 \text{ g/cm}^3$. This higher measured density is especially apparent in samples 5-9, where the denser MetlWeld adhesive was used for assembly of the layers. In addition to a higher density, MetlWeld is more viscous, which causes additional epoxy to stick to each layer when assembled. Facesheets were also incorporated from sample 4 on, which contributed to additional composite and adhesive not accounted for in the original density

estimation, Equation 3.24. This is seen as an increase in the difference between predicted and measured density.

Table 6.1. Comparison of relative density.

	L (mm)	θ (deg)	t (mm)	Relative Density, measured	Relative Density, eqn. 3.24	% Diff
Sample 1	7.07	45	0.4	0.093	0.080	14%
Sample 2	7.07	45	0.4	0.089	0.080	10%
Sample 3	7.07	45	0.4	0.089	0.080	10%
Sample 4	7.07	45	0.2	0.052	0.040	23%
Sample 5	7.07	45	0.4	0.119	0.080	33%
Sample 6	7.07	45	0.6	0.159	0.120	25%
Sample 7	7.07	45	0.6	0.172	0.120	30%
Sample 8	7.07	45	0.6	0.171	0.120	30%
Sample 9	7.07	45	0.6	0.154	0.120	25%

Densification strain as shown in the Gibson-Ashby method [1] was compared with experimental results of the quasi-static compression testing. This method generally predicted densification at a higher strain than measured, and the discrepancy is likely caused by the inefficiency of packing the folded plates into a small volume as they buckle. Results from the quasistatic compression tests and the standard Gibson-Ashby method are given below, Figure 6.1.

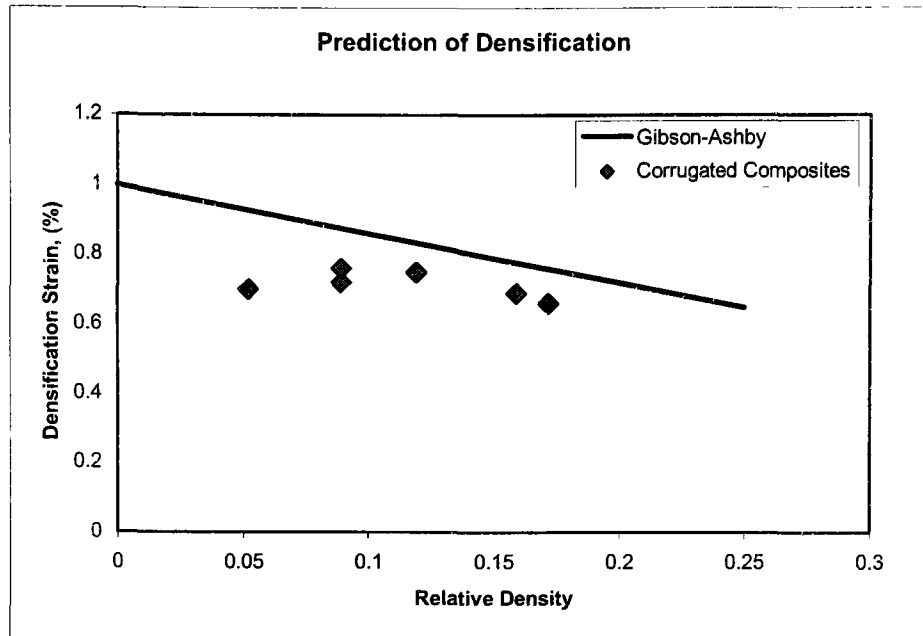


Figure 6.1. Predicted densification strain.

Strength estimations were conducted using estimates for critical plate buckling loads as suggested by Kicher [62] and covered in Chapter 3. The method for these estimations is covered in section 3.5.2, and the plate stiffness calculations (shown below,

Table 6.2) for this section were completed using the MATLAB script as outlined in Appendix B.

The predicted strength is higher than the measured plateau strength for nearly all of the samples. One possible reason for this is the point loading where peaks of adjacent layers contact one another. This leads to a higher stress at points of contact, thus instigating failure. Another potential cause is in manufacturing defects of the laminae. Regardless, the predictions do show that increasing strength due to stiffer laminated plates corresponds to stronger samples.

Table 6.2. Plate stiffness and predicted maximum stress.

	Ply Orientation	D_{yy} (N-m)	σ_m by eqn. 3.29 (MPa)	σ_m as measured
Sample 1	0/90	0.0440	1.23	0.42
Sample 2	± 45	0.0260	0.72	0.55
Sample 3	± 45	0.0260	0.72	0.61
Sample 4	0/90	0.0037	0.10	0.15
Sample 5	± 45	0.0260	0.72	0.75
Sample 6	0/90, ± 45 , 0/90	0.0620	1.73	1.66
Sample 7	± 45 , 0/90, ± 45	0.0612	1.71	1.41

6.2. Comparison to Other Materials

The corrugated composites described in this paper are similar in strength to commercially produced metallic foams. Alporas® (Shinko Wire Co., Japan), is a stochastic aluminum alloy produced by adding a blowing agent to heated liquid alloy, Figure 6.2. A sample of Alporas was tested quasi-statically in a similar method to those tested in Chapter 5 for comparison with the corrugated composites from this research.

Dimensionally, the Alporas sample was slightly smaller than the corrugated aramid-epoxy samples. The length was 45.2 mm, depth was 44.8 mm, and height 45.4 mm. Mass was measured at 20.9 g, with calculated density of 0.227 g/cm³ and a relative density of 0.081. Strain rate for the test was $\dot{\epsilon} = 0.001 \text{ s}^{-1}$.

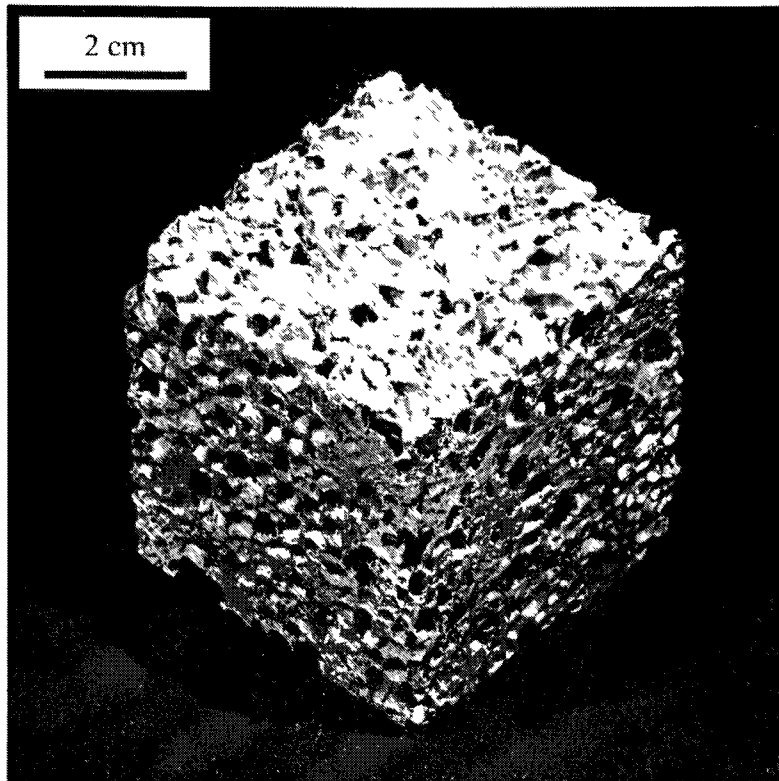


Figure 6.2. Alporas aluminum foam sample (Shinko Wire Co., Japan).

The stress-strain diagram for the Alporas foam shows a peak strength of nearly 1.6 MPa, followed by a slightly lower plateau stress of around 1.5 MPa, Figure 6.3. The increase in stress seen at densification (near 70% strain) happens slowly as the cells walls within the foam crush together, which is not always desirable for energy absorbers. When compared to the best performing corrugated composite samples, the performance is quite close, although the Alporas reaches densification sooner, which can limiting its total energy absorption.

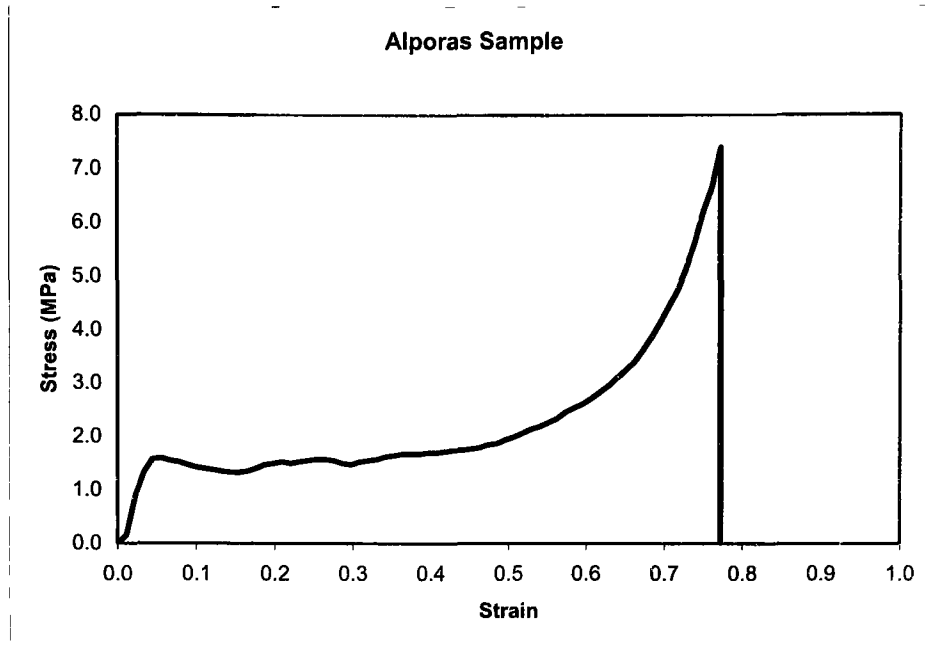


Figure 6.3. Results for quasi-static testing of Alporas.

A 5056 series aluminum-alloy honeycomb, HexWeb CR III (Hexcel Corporation, Dublin, CA) was also tested as a comparison material, Figure 6.4. Cell size was 0.25 in and gage thickness was 0.002 in. Honeycomb, as discussed in Section 1.1.2, has excellent performance of energy absorbed per unit mass. Its disadvantages include an initial high peak stress upon loading followed by a lower plateau stress for the majority of the crushing in compression.

The sample tested was chosen to be nearly the same area as the corrugated composite samples. Its width was 65.9 mm, its length was 66.5 mm, and its height was 76.2 mm. The mass of the sample tested was 23.8 g, with a calculated density of 0.071 g/cm³ and a relative density of 0.025. Quasi-static testing at a strain rate of $\dot{\epsilon} = 0.01 \text{ s}^{-1}$ was performed in a similar manner to that for the corrugated samples as discussed in Section

5.2. A peak strength of approximately 4.45 MPa is followed by a relatively flat plateau of 1.8 MPa, until densification at 80% strain, Figure 6.5.

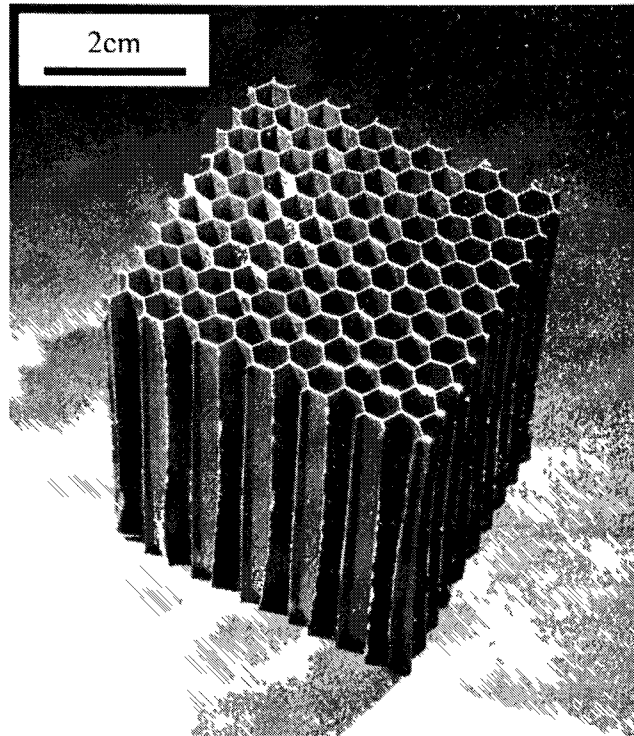


Figure 6.4. Honeycomb used for compression testing (Hexcel Composites, Dublin, CA).

Compared to the best performing corrugated aramid-epoxy laminates discussed in this research, honeycomb outperforms their energy absorption on a per weight basis by a factor of nearly 4. On a per unit volume comparison, however, the honeycomb has energy absorption about 25% better than the best performing composite corrugated sample tested here. The major drawbacks are the high out-of-plane peak strength (~2.5 times the plateau strength), lack of strength along in-plane directions, and lack of penetration resistance in the out-of-plane direction

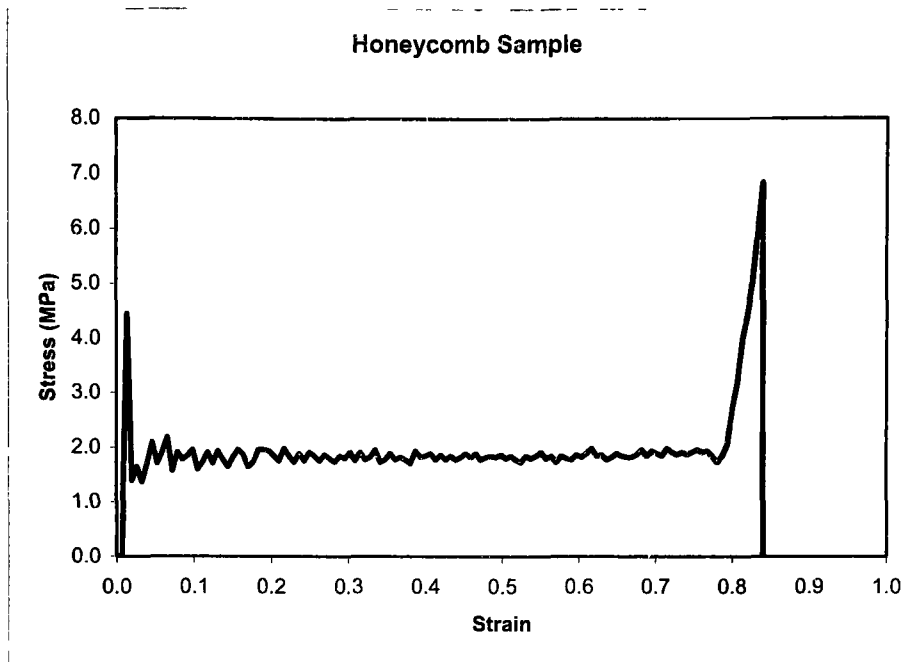


Figure 6.5. Results for quasi-static testing of honeycomb.

Overall, the behavior of corrugated composite cellular materials described in this research perform reasonably well in comparison to commercially available materials. Their strength is similar to that of metallic foams of similar density, but less than that of honeycombs.

These results are shown graphically for compressive plateau strength versus density below, Figure 6.6. This shows that the Alporas aluminum alloy foam is similar in strength and density to samples 6 and 7, while the honeycomb is a much lower density. Energy absorbed per unit volume versus density is also shown, Figure 6.7. Here, energy absorption characteristics of the corrugated composites with the Alporas can be seen, as well as the good performance of the honeycomb.

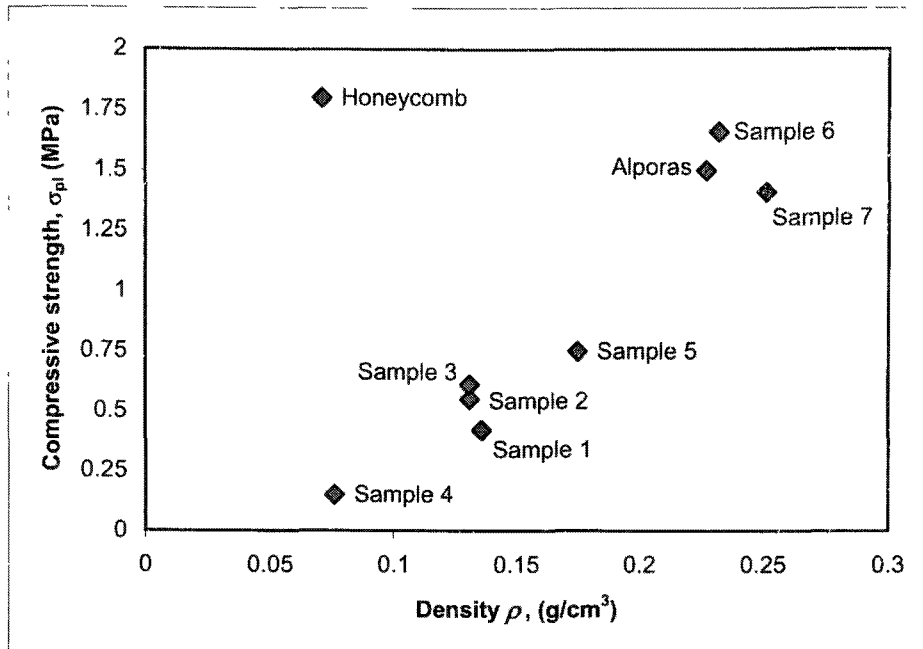


Figure 6.6. Comparison of compressive plateau stress.

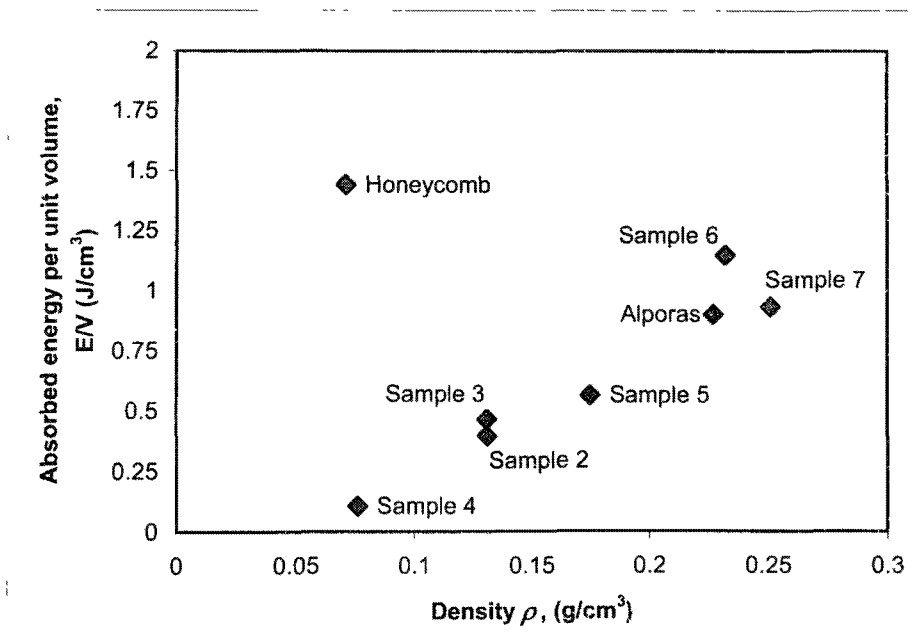


Figure 6.7. Comparison of energy absorbed per unit volume.

The dynamic tests for this research were compared to two samples of the HexWeb honeycomb, Figure 6.8. These samples had aramid-epoxy facesheets bonded to the impact face using MetlWeld adhesive epoxy. The facesheets were single ply, style 120 aramid fabric, the same material as used in the corrugated composite samples.

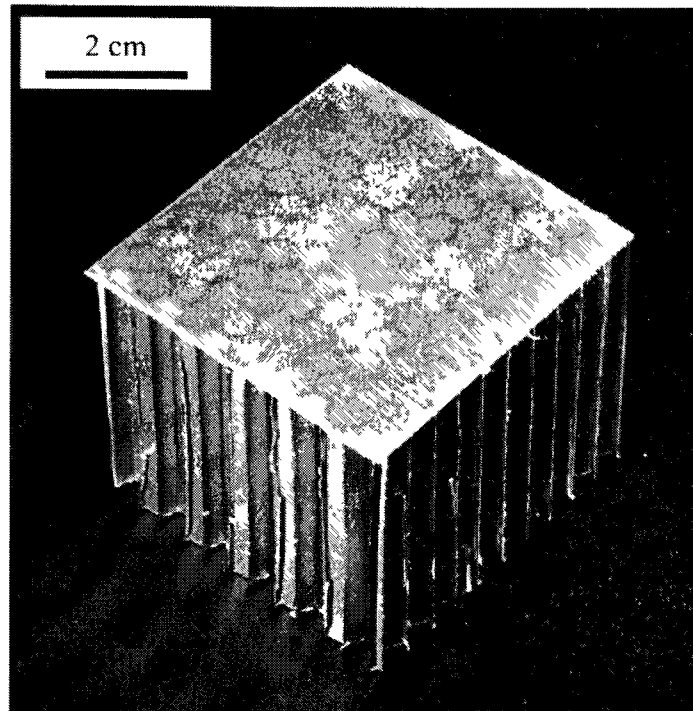


Figure 6.8. HexWeb honeycomb with attached aramid facesheet.

The two samples of honeycomb with the facesheets were built to be the same dimensions of the corrugated aramid samples. The dimensions for the first honeycomb sample were 54 mm in height, 66 mm for length, and 68 mm for width. Mass for this sample was 19.1 g, and density was calculated to be 0.078 g/cm^3 . The second honeycomb sample was measured at 56 mm in height, 69 mm for length, and 66 mm for width. Its mass was 19.1 g, and density was 0.075 g/cm^3 . Facesheets and adhesive are responsible for the increase in density (~5%) compared to honeycomb alone.

Indenter stress-displacement diagrams are plotted below for both honeycomb penetration tests Figure 6.9. The low speed test was conducted at 1.67 m/s (same as corrugated sample 8) and the high speed at 4.16 m/s (same as corrugated sample 9). Mass was unchanged, and therefore energy for the first and second tests corresponded with corrugated samples 8 and 9, respectively.

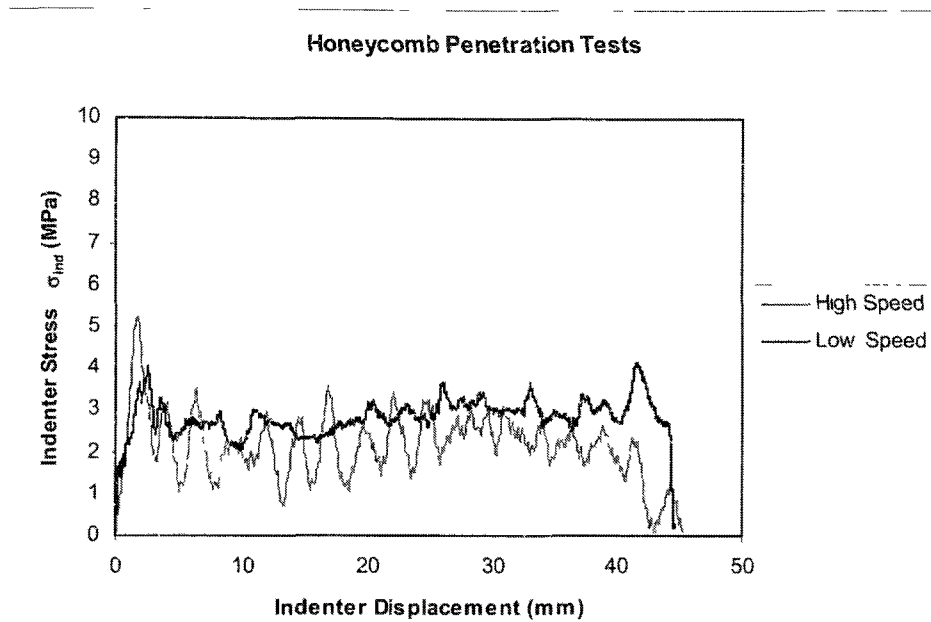


Figure 6.9. Stress-displacement for honeycomb samples.

The penetration tests show a larger amount of fluctuation in the reading for the high speed test. Also, an initial peak in the stress reading is seen, which may be attributed to the aramid-epoxy facesheet. Mean stress values are similar for both tests (averaging 2.5 MPa), but much lower than the stress measured during the corrugated aramid samples (averaging around 8 MPa). This type of behavior is likely due to the unfavorable orientation of material within the honeycomb.

6.3. *Further Research*

Through this original research, it has become clear that obtaining accurate properties for the behavior of any energy absorbing material is important. Since experimental data for composite behavior is an important aspect of understanding its failure modes, devising a test for laminated plate members under in-plane compressive loads would prove useful. Finite Element Analysis (FEA) could prove to be a useful tool for strength predictions of the corrugated composites. Such methods should give quantitative value for the critical buckling load N_{CR} for a variety of different corrugation designs; altering geometry, fabric orientation and types, and orientation of applied load (in-phase or out-of-phase point loading). It has been suggested that satin weaves provide higher stiffness than plain weaves [60], but this should be examined for the geometry in question if the number of rovings in the compressed plate is low.

Additional improvements to the performance could be obtained through automation of the layup process. Vacuum bagging or heated autoclave using prepregs (fibers preimpregnated with resin) can reduce void count and improve the overall quality of the layup [37]. Single, large sheets of corrugation (rather than a few inches per side) would vastly increase the production rate of samples while maintaining a reasonable price for manufacture.

The use of different corrugation geometry should be studied as well. This should also include multi-layer samples with different corrugation geometry of each layer, which could be used to control the failure and rise in stress level through compression. Hybrid materials (i.e., woven carbon/aramid blends) or changes in fabric orientation are other proposed ways to achieve this goal.

Penetration or ballistic behavior should be quantified for the corrugated composites. Aramid fibers are well known for their penetration resistance, however some testing should conform that in a structural corrugated configuration this benefit is still realized. Ballistic penetration tests can be performed under the guidance of ASTM or MIL standards for comparison to other materials and structures with similar properties.

Lastly, additional mechanical properties should be investigated. Stiffness and strength values in multiple axes are needed for nearly all forms of structural designs. The layered approach of this material should provide a good amount of strength in multiple axes, and this behavior could be tailored by the orientation of the corrugation on each layer, much like the fabric orientation in laminated plates.

6.4. Conclusions

This work shows that corrugated composites can make viable energy absorbers. The fabrication methods which were developed produced samples with mechanical properties similar to those of commercially produced metal foams. After a few iterations, compressive strengths over 1.5 MPa were reached with a relatively smooth plateau stress and no sharp peak stress. Through refinement of this process and an understanding of the mechanical modeling, it is believed that the performance of these materials could be improved further.

7. REFERENCES

1. Gibson, L.J. and Ashby, M.F. *Cellular Solids, Structure and Properties, Second Edition*. Cambridge University Press, Cambridge, United Kingdom. 1997.
2. Sypeck, D.J. *Constructed Cellular Metals. Processing and Properties of Lightweight Cellular Metals and Structures* TMS, Warrendale, PA pp. 35-45. 2002.
3. Du Pont Company. *Kevlar: The Fiber that Lets you Re-Think Strength and Weight*. Document E 38532. Date unknown.
4. Hooke, R. *Micrographia*. The Royal Society, London, England. 1664.
5. Sypeck, D.J. and Wadley, H.N.G. *Multifunctional Microtruss Laminates: Textile Synthesis and Properties* Journal of Material Research Vol. 16 No. 3. pp 890 -- 897. 2001
6. Choi, Jeong Ho. *Fabrication and Compressive Yield Strength of Open Cell Corrugated Cellular Solids*. MSAE Thesis, Embry-Riddle Aeronautical University. 2005.
7. Britannica Concise Encyclopedia. *Bee*. Available at: <http://concise.britannica.com/ebc/article-9356880/bee>. Accessed April 11, 2007.
8. Wikipedia. *Sponge*. Available at: <http://en.wikipedia.org/wiki/Sponge>. Accessed February 27, 2007.
9. Bonfield, W. *Artificial Bone*. Concise Encyclopedia of Composite Materials. Pergamon Press, Oxford, England. 1989.
10. Raymer, D.P. *Aircraft Design: A Conceptual Approach. Third Edition*. American Institute of Aeronautics and Astronautics. Reston, Virginia. 1999.
11. Meyer, J.A. *Wood-Polymer Composites*. Concise Encyclopedia of Composite Materials. Pergamon Press, Oxford, England. 1989.
12. Reid, S.R and Peng, C.. *Dynamic Uniaxial Crushing of Wood*. International Journal of Impact Engineering. Vol. 19 No. 5. pp. 531-570. 1997.
13. Lekhnitskii, S.G. *Anisotropic Plates*, Translation of *Anizotropnye plastinki*. Gordon and Breach Science Publishers, New York. 1984.
14. U.S. Census Bureau. *Statistics for Industry Groups and Industries: 2005*.

15. Ashby, M.F., et al. *Metal Foams: A Design Guide*. Butterworth-Heinemann, Woburn, Massachusetts. 2000.
16. Liang, et al. *Optimum Design of Metallic Corrugated Core Sandwich Panels Subjected to Blast Loads*. Ocean Engineering. Vol. 28, pp. 825-861. 2001.
17. Knox, E.M., et al. *Adhesively Bonded Steel Corrugated Core Sandwich Construction for Marine Applications*. Marine Structures. Vol. 11, pp. 184-204. 1998.
18. Wiernicki, C.J. *Structural Analysis Methods for Lightweight Metallic Corrugated Core Sandwich Panels Subjected to Blast Loads*. Navel Engineers Journal. Vol. 103, pp. 192-203. 1991.
19. John, L.K. *Designing with Fibre-Reinforced Composites to Meet New Bird Strike Requirements*. Fifth Technical Symposium, Design and Use of KEVLAR Aramid Fiber in Composite Structures. Reno, Nevada. 1984.
20. Côté, F., et al. *The Out-of-Plane Compressive Behavior of Metallic Honeycombs*. Materials Science and Engineering. Vol. 380, pp. 272-280. 2004.
21. Wu, E. and Jiang, W. *Axial Crush of Metallic Honeycombs*. International Journal of Impact Engineering. Vol. 19, No. 5-6. pp. 439-456. 2006.
22. Sypeck, D.J. and Wadley, H.N.G. *Cellular Metal Truss Core Sandwich Structures*. Advanced Engineering Materials Vol. 4, No. 10. pp 759 – 764. 2002
23. Deshpande, V.S., Fleck, N.A. *Energy Absorption of an Egg-Box Material*. Journal of the Mechanics and Physics of Solids. Vol 51, pp. 187-208. 2003.
24. Basily, B.B., Elsayed, E.A. *Dynamic Axial Crushing of Multilayer Core Structures of Folded Chevron Patterns*. International Journal of Materials and Product Technology. Vol. 21, Iss. 1-3, pp. 169-185. 2004.
25. Deshpande, V.S., Fleck, N.A. *High Strain Rate Compressive Behavior of Aluminum Alloy Foams*. International Journal of Impact Engineering. Vol. 24, pp 277-298. 2000.
26. Balch, D.K., et al. *Plasticity and Damage in Aluminum Syntactic Foams Deformed Under Dynamic and Quasi-Static Conditions*. Materials Science and Engineering. Vol. A 391, pp 408-417. 2005.
27. Min, J.B., et al. *Analysis of Stainless Steel Sandwich Panels with a Metal Foam Core for Lightweight Fan Blade Design*. 45th AIAA/ASME/ASCE/AHS/ASC Structures, Structural Dynamics, and Materials Conference. Palm Springs, CA. 2004

28. Kumar, R.S. and McDowell, D.L. *Design of Multifunctional Materials*. 9th AIAA/ISSMO Symposium on Multidisciplinary Analysis and Optimization. Atlanta, GA. 2002.
29. Wirtz, R.A., et al. *Thermal/Fluid Characteristics of 3-D Woven Mesh Structures as Heat Exchanger Surfaces*. IEEE Transactions on Components and Packaging Technologies, Vol. 26, No. 1. 2003.
30. Granta Design Limited. *Cambridge Engineering Selector Constructor*. Version 4.7.0, Build: 2006, 12, 6, 1. Cambridge, United Kingdom. 2006.
31. Britannica Concise Encyclopedia. *Composite Material*. Available online at <http://concise.britannica.com/ebc/article-9361292/composite-material>. Visited March 15, 2007.
32. Baker, A.F., et al. *Composite Materials for Aircraft Structures: Second Edition*. American Institute of Aeronautics and Astronautics. Reston, Virginia. 2004.
33. Beardmore, P. *Automotive Components: Fabrication* Concise Encyclopedia of Composite Materials. Pergamon Press, Oxford, England. 1989.
34. Cooke, T.F. *Fibers and Textiles: An Overview*. Concise Encyclopedia of Composite Materials. Pergamon Press, Oxford, England. 1989.
35. Schwartz, M. *Composite Materials Handbook, Second Edition*. Mc-Graw Hill, Inc. New York. 1992.
36. Callister, W.D. *Fundamentals of Materials Science and Engineering*. John Wiley & Sons, New York. 2001.
37. Barbero, E.J. *Introduction to Composite Material Design*. Taylor and Francis. Philadelphia, PA. 1999.
38. Bowen, D.H. *Applications of Composites: An Overview*. Concise Encyclopedia of Composite Materials. Pergamon Press, Oxford, England. 1989.
39. International Union of Pure and Applied Chemistry. *Compendium of Chemical Terminology*. Available at: <http://goldbook.iupac.org/> Visited April 4, 2007.
40. Wikipedia. *Aromaticity*. At: <http://en.wikipedia.org/wiki/Aromatic>. Accessed March 27, 2007.
41. Loken, H.Y. *Du Pont Aramid for Advanced Composites*. Industrial Composites Seminar, Society for the Advancement of Materials and Process Engineering. Midwest Chapter. 1982.
42. Department of Defense. *Composite Material Handbook, Vol. 3: Polymer Matrix Composites Materials Usage, Design, and Analysis*. MIL-HDBK-17F, 2002.

43. Wardle, M.W. *Designing Composite Structures for Toughness*. Fifth Technical Symposium, Design and Use of KEVLAR Aramid Fiber in Composite Structures. Reno, Nevada. 1984.
44. Chang, K.K. *Aramid Fibers*. ASM Handbook, Volume 21: Composites. ASM International. Materials Park, Ohio. 2001.
45. Du Pont Company. *Honeycomb of "Nomex" Aramid Structural Sheet*. 1985
46. Gudgeon Brothers, Inc. *West Systems Typical Physical Properties*, available at <http://www.westsystem.com/frames/tier2/productinfo/typicalphysicalproperties.htm>. Accessed Mar 5, 2007.
47. Sypeck, D.J. *Damage Evolution in Titanium Matrix Composites*. Ph. D. Dissertation. University of Virginia, 1996.
48. Nolan, Peter J. *Fundamentals of College Physics, Second Edition*. W.M. Brown Communications, Dubuque, Iowa. 1995.
49. Avalle, M., et al. *Characterization of Polymeric Structural Foams Under Compressive Impact Loading by Means of Energy-Absorption Diagram*. International Journal of Impact Engineering. Vol. 25, pp 255-472. 2001.
50. Lankford, J. and Gray, W. *Composite Armor*. Concise Encyclopedia of Composite Materials. Pergamon Press, Oxford, England. 1989.
51. Winchester Ammunition. *2007 Product Guide – Final.pdf*. Available online at <http://www.winchester.com/pdf/2007%20Product%20Guide%20-%20Final.pdf> accessed April 10, 2007.
52. Chou, T.W. *Woven-Fabric Composites· Properties*. Concise Encyclopedia of Composite Materials. Pergamon Press, Oxford, England. 1989.
53. Chang, M.J. *Hybrid Protective Composite*. U.S. Patent 6162746, December 1998.
54. Cronkhite, J.D. *Design of Helicopter Composite Structures for Crashworthiness*. Fifth Technical Symposium, Design and Use of KEVLAR Aramid Fiber in Composite Structures. Reno, Nevada. 1984.
55. Langston, P.R. *Design and Use of Kevlar in Aircraft Structures*. Fifth Technical Symposium, Design and Use of KEVLAR Aramid Fiber in Composite Structures. Reno, Nevada. 1984.
56. Peterson, J.P. and Card, M.F. *Investigation of the Buckling Strength of Corrugated Webs in Shear*. NASA Technical Note D-424. 1960.
57. Tsai, S.W. and Hahn, H.T. *Introduction to Composite Materials*. Technomic Publishing Company, Lancaster, Pennsylvania. 1980

58. Calcote, Lee R. *The Analysis of Laminated Composite Structures*. Van Nostrand Reinhold Company, New York. 1969
59. Naik, N.K. *Woven Fabric Composites*. Technomic Publishing Company, Inc. Lancaster, PA. 1994.
60. Ishikawa, T. and Chou, T.W. *Stiffness and Strength Behaviour of Woven Fabric Composites*. Journal of Materials Science. Vol. 17, No. 11. pp. 3211-3220. 1982.
61. Ugural, Ansel C. *Stresses in Plates and Shells, Second Edition*. McGraw-Hill Company, Singapore. 1999.
62. Kicher, T.P. and Mandell, J.F. *A Study of the Buckling of Laminated Composite Plates*. AIAA Journal. Vol 9, No. 4. pp. 605-613. 1971.
63. Bažant, Z.P. and Cedolin, L. *Stability of Structures: Elastic, Inelastic, Fracture and Damage Theories*. Oxford University Press., New York. 1991.
64. Tian, Y.S. and Lu, T.J. *Optimal Design of Compression Corrugated Panels*. Thin-Walled Structures Vol 43, pp. 477-498. 2005.
65. ASTM International. *Standard Test Method for High Speed Puncture Properties of Plastics Using Load and Displacement Sensors*. Designation D-3763-06. American Society for Testing and Materials International, West Conshohocken, PA. 2006.
66. System Three Resins, Inc. *MetlWeld Structural Adhesive Technical Datasheet*, at http://www.systemthree.com/members/tds/Metlweld_TDS.pdf. Accessed Mar 6, 2007.

8. Appendix A – Material Details

West System Epoxy 105/205 is a fast setting, high strength structural epoxy for marine and aerospace applications. The resin used (West System 105) is mixed in with 1/5 part hardener by weight (West System 205), which gives about 12 minutes working time. Mechanical properties of the family of West System epoxies are shown below [46].

Table A.1. West System epoxy properties.

Property	105/205	105/206	105/207	105/209
Mix Ratio by weight*	5.07:1	5.0:1	3.4:1	3.56:1
Mix Viscosity @ 72°F (cPs)	975	725	775	725
Pot Life of 100 g @ 72°F (min.)	12	21.5	26.4	51
Specific Gravity of Cured Resin	1.180	1.180	1.163	1.163
Hardness @ 1 day (Shore D)	80	80	78	70
Hardness @ 2 weeks (Shore D)	83	83	82	82
Compression Yield @ 1 day (MPa)	69.7	55.1	41.5	8.45
Compression Yield @ 2 weeks (MPa)	78.7	79.3	74.7	69.13
Tensile Strength (MPa)	54.1	50.5	51.8	50.59
Tensile Elongation (%)	3.4	4.5	3.4	3.5
Tensile Modulus (GPa)	2.81	3.17	2.82	2.96
Flexural Strength (PSI)	97.3	81.4	89.7	86.9
Flexural Modulus (PSI)	3.18	3.10	3.54	2.95
Heat Deflection Temperature (°F)	47.8	50.6	47.8	46.7
Onset of Tg by DSC (°F)	53.9	52.2	50.6	49.4
Ultimate Tg by DSC (°F)	61.1	59.4	58.3	56.7
Izod Impact, notched (J/m)	49.6	28.8	67.8	58.7

MetlWeld adhesive epoxy is a high strength, toughened structural adhesive with excellent mechanical properties that also excels in bonding of dissimilar metals. Like most adhesives, the surface to be bonded must be freshly sanded and clean of grease, wax, oil, and other contaminants. MetlWeld is designed to cure at room temperature [66].

Table A.2. System Three MetlWeld adhesive properties.

Mix Ratio by weight resin/hardener	100/91
Mix ratio by volume resin/hardener	100/100
Working time @ 25 °C	30 minutes
Tack-free time @ 25 °C	4 hours
Specific Gravity, Mixed	1.36
Lap Shear Strength, Al-Al, (MPa)	14.82
Lap Shear Strength, Cold-Rolled Steel (MPa)	15.44
Lap Shear Strength, Galvanized Steel (MPa)	12.55
T-Peel Strength, PLI	28

9. Appendix B – Plate Stiffness Calculator

The plate stiffness calculator was written in MATLAB v7.0.1. It utilizes standard methods for unidirectional laminates outlined in a number of references [32, 37, 58]. Units may be either English or SI, as long as consistency is maintained.

For the stiffness calculations, the plate height a and width b were held constant, along with the fiber and matrix stiffness, E_f , E_m . Volume fractions V_f and V_m were 0.5 and 0.5, respectively. Layer thickness t is taken as one-half of cloth thickness [44]. Unidirectional composite properties E_l and E_t were calculated as discussed in chapter 1. The major Poisson ratio used and ν and flexural stiffness G_{lt} were based on Kevlar 49 and an unspecified epoxy matrix [32]. However, they have a small effect on the overall stiffness D_{yy} .

Table B.1. Values used for calculations of plate stiffness.

	n	t , (mm)	Layer Orientations (degrees)	Stiffness D_{yy}
1	2	0.125	[0, 90]	0.0440
2	2	0.125	[-45, +45]	0.0260
3	2	0.125	[-45, +45]	0.0260
4	2	0.055	[0, 90]	0.0037
5	2	0.125	[-45, +45]	0.0260
6	6	0.055	[0, 90, -45, +45, 90, 0]	0.0620
7	6	0.055	[-45, +45, 90, 0, +45, -45]	0.0612
8	6	0.055	[0, 90, -45, +45, 90, 0]	0.0620
9	6	0.055	[0, 90, -45, +45, 90, 0]	0.0620

```

% Multi-laminate plate stiffness, October 2006

%%% Assumes same material on each layer
%%% Only orientation may change

clear
n=6; %layers (2 per woven ply)
t=0.055e-3; %thickness PER layer, (m)
a=0.00707; %plate height, (m)
b=0.055; %plate width, (m)
theta=[+45 -45 0 90 -45 +45]; %fiber orientation

Vf=0.5; %Fiber Volume Fraction
Vm=0.5; %Matrix Volume Fraction
Ef=120e9; %Fiber Stiffness
Em=2.8e9; %Matrix Stiffness

El=Ef*Vf + Em*Vm; %Stiffness along fiber direction
Et=1 / (Vf/Ef + Vm/Em); %Stiffness in transverse direction
nu=0.34; %ESTIMATED Poisson, L to T, nu[lt]
Glt=2.1e9; %ESTIMATED shearing modulus

%%% LAYER THICKNESS %%%
for i=1:n+1 %Calculate upper and lower
    h(i)=t*(-0.5*n+i-1); % heights of each layer.
end

%%% MATERIAL COMPOSITE STIFFNESS MATRIX and COMPLIANCE MATRIX %%%
% Compliance matrix elements, natural axes:
S11=1/El;
S12=-nu/El; %ALSO = -nu[tl]/Et
S22=1/Et;
S44=1/Glt;
% Composite stiffness matrix elements:
C11=S22/(S11*S22-S12^2);
C12=-S12/(S11*S22-S12^2);
C22=S11/(S11*S22-S12^2);
C44=1/S44;
% Composite stiffness matrix:
C(1,:)=[C11 C12 0];
C(2,:)=[C12 C22 0];
C(3,:)=[0 0 C44];

%%% TRANSFORMATION MATRICIES %%%
% Transformation of axes from x,y to 1 and 2 for layers:
T=zeros(3,3,n); %initialize variable.
%Repeat for every layer.
for i=1:n
    ang=theta(i)*pi/180;
    c2=cos(ang).^2;
    s2=sin(ang).^2;
    sc=sin(ang)*cos(ang);
    T(1,:,i)=[(c2) (s2) (sc)];
    T(2,:,i)=[(s2) (c2) (-sc)];
    T(3,:,i)=[(-2*sc) (2*sc) (c2 - s2)];
end

```

```

%%% PLATE STIFFNESS MATRIX %%%
for i=1:n
    Cbar(1:3,1:3,i)=T(:, :, i)'*C*T(:, :, i);
end

%%% Sum layers for the total. %%%
D=zeros(3,3);
for i=1:n
    D(:, :)=D(:, :)+1/3*(Cbar(:, :, i).*(h(i+1)^3)-(h(i)^3));
end

D1=D(1,1);
D2=D(2,2);
D3=D(1,2)+2*D(3,3);

%%% CRITICAL PLATE LOAD, from KICHER %%%
%%% Ncr will be in Force/Length and in the y-direction %%%
for m=1:1
    Ncr=pi^2*D2/a^2
end

```